



School of Chemistry

**Microwave plasma assisted growth of CVD diamond
incorporating BN atom clusters**

Bea Nutbrown

**This thesis is submitted in partial fulfilment of the requirements for the
Honours Degree of MSci at the University of Bristol**

April 2024

Supervisor: Professor Neil Fox
Second Assessor: Professor Paul May
Section: Physical Chemistry

Statement of factors which limited progress

- First term was spent doing boron line calibrations/training so was unable to start any personal practical work until January
- Throughout February there were faults with striking and maintaining plasma, leading to growth runs taking a much longer time (e.g., one 3 hour runs took 6 hours due to stopping and starting of the plasma) and this therefore meant not being able to fit in my scheduled 2 per day
- The reactor stopped working completely on the 15th of February due to issues with the power supply, so remaining growths that were already unfortunately delayed due to plasma faults, then couldn't be completed.

Abstract

The fabrication of an n-type diamond that operates at room temperature would revolutionise the field of diamond electronics, harnessing diamond's superior properties into novel applications. Doped diamond exhibits great potential in electronics as a semiconductor, with the creation of p-type diamond already well documented, however n-type diamond creation remains a challenge. Its discovery would enable the manufacture of diamond-based pn junction devices, with applications in energy storage and electric transport.

As efficient BN cluster incorporation into the diamond lattice is expected to give an n-type diamond, this project explored the individual effects of B and N atoms within boron and nitrogen co-doped diamond (BNDD). Microwave plasma chemical vapour deposition (MP CVD) was employed to deposit BNDD onto p-type Si substrates at $\sim 900^\circ\text{C}$, 1.1 kW and 100 torr. The growth process maintained specific methane and hydrogen gas flows, 25 sccm and 500 sccm, respectively, whilst varying the ratios of boron and nitrogen to carbon. N_2 gas was varied between 0-7.5% N_2/C ratio with diborane fixed at 0.5 sccm, and subsequently the B_2/C ratio was varied between 1-2.5%, fixing N_2 to 1.1 sccm. These specific parameters allowed the distinct effects of each dopant to be monitored and understood.

Samples were analysed using Raman spectroscopy, scanning electron microscopy (SEM), four-point probe apparatus, Hall measurement system, x-ray photoelectron spectroscopy (XPS), ultraviolet photoelectron spectroscopy (UPS) and photoemission electron microscopy (PEEM). These techniques provided valuable insights into the conductivity, surface morphology and band structures of the samples, enabling the evaluation of dopant incorporation and potential n-type characteristics.

Although n-type samples were not confirmed to have been made, results indicated that the 1.5% and 2% B_2/C diamond films had potential n-type characteristics. Both B and N doping caused decreased sheet resistance in samples, with N-doping increasing growth rate and B-doping enlarging individual grain sizes. A reduction in the work function (WF) of samples could be correlated to increased N-doping, despite the presence of nitrogen not being visible in XPS spectra. Additionally, unusual surface effects from UV exposure were reported on a highly N-doped film, due to high levels of oxygen binding attributed to the exposure of the film to atmospheric oxygen.

Acknowledgements

I would like to thank Professor Neil Fox, my supervisor, for the advice and support throughout the duration of this project.

For their help with analytical techniques: Dr Jude Laverock for NanoESCA work, Dr Jean-Charles Eloi for SEM, and Arpit Nandi for Hall measurements.

I would also like to thank my tutor Dr Sebastien Rochat for his support across all four years of my time at Bristol.

To my friends and family who have been there throughout my whole degree, thank you.

Contents

Abstract	2
Acknowledgements	3
Abbreviations:	6
1 Introduction	7
1.1 Diamond structure & properties.....	7
1.1.1 Synthetic diamond applications.....	7
1.1.2 Bonding in diamond	8
1.1.3 Diamond classification	9
1.2 Diamond synthesis.....	10
1.2.1 High pressure high temperature (HPHT)	10
1.2.2 Chemical vapour deposition (CVD)	12
1.2.3 Substrate choice & preparation	15
1.2.4 Crystal orientation	16
1.3 Band gap theory.....	17
1.3.1 Semiconductors	17
1.3.2 Fermi level.....	18
1.4 Doping in diamond.....	20
1.4.1 n-type vs p-type dopants	20
1.4.2 Nitrogen doped diamond.....	21
1.4.3 Boron doped diamond	21
1.4.4 Theory of co-doping.....	22
1.4.5 Methods of dopant incorporation	22
1.4.6 Boron nitrogen co-doped diamond (BNDD)	23
1.5 Previous synthesis of B N co-doped diamond	24
1.5.1 Applications of BN co-doped diamond	27
1.6 Characterisation techniques	28
1.6.1 SEM – Scanning Electron Microscopy	28
1.6.2 Raman Spectroscopy.....	29
1.6.3 XPS – X-ray Photoelectron Spectroscopy.....	31
1.6.4 UPS – Ultra-violet Photoelectron Spectroscopy	32
1.6.5 PEEM – Photoemission Electron Microscopy	33
1.6.6 SIMS – Secondary Ion Mass Spectrometry	34
1.6.7 Sheet resistance measurements.....	34
1.6.8 Hall measurements	34
1.7 An alternative dopant gas: N ₂ O	35

2	Project aims.....	37
3	Experimental	38
3.1	Preparation of substrate	38
3.2	Microwave Reactor	38
3.2.1	Nitrogen variation runs	38
3.2.2	Boron variation runs	39
3.3	Analysis	39
3.3.1	Raman	39
3.3.2	Resistivity	39
3.3.3	Hall measurements	41
3.3.4	SEM	41
3.3.5	XPS.....	42
3.3.6	UPS and PEEM.....	42
4	Results & discussion	43
4.1	Raman spectroscopy.....	43
4.1.1	Nitrogen variation runs.....	43
4.1.2	Boron variation runs	44
4.2	SEM	45
4.2.1	Surface morphology.....	45
4.2.2	Film thickness.....	49
4.2.3	Substrate growth	52
4.3	Four-point probe.....	53
4.4	Hall measurements	55
4.4.1	Nitrogen variation runs.....	55
4.4.2	Boron variation runs	57
4.5	XPS.....	59
4.5.1	Survey spectra.....	59
4.5.2	C 1s spectra	60
4.5.3	N 1s and B1s spectra	61
4.6	UPS.....	62
4.6.1	Valence band maxima	62
4.6.2	Work functions.....	63
4.7	PEEM.....	65
4.8	UV surface effects:	67
5	Conclusions and future work.....	68
5.1	Conclusions	68

5.2	Future work.....	69
6	References	71
7	Appendix.....	75

Abbreviations:

- **BDD** – Boron-doped diamond
- **BNDD** – Boron and nitrogen co-doped diamond
- **CBM** – Conduction band minimum
- **CVD** – Chemical vapour deposition
- E_F – Fermi level
- E_G – Band gap
- E_{VAC} – Vacuum level
- **HOMO** – Highest occupied molecular orbital
- **HPHT** – High pressure high temperature
- **I/V** – Current / voltage
- **LUMO** – Lowest unoccupied molecular orbital
- **MP** – Microwave plasma
- **NV** – Nitrogen vacancy
- **PEEM** – Photoemission electron microscopy
- **RTP** - Room temperature and pressure (298 K and 1 atm)
- **sccm** - Cubic centimetre per minute at STP
- **SEM** – scanning electron microscope
- **SIMS** – Secondary ion mass spectrometry
- **STP** – Standard temperature and pressure (273 K and 1 atm)
- **UPS** – Ultraviolet photoelectron spectroscopy
- **VBM** – Valence band maximum
- **WF** – Work function
- **XPS** – X-ray photoelectron spectroscopy

1 Introduction

1.1 Diamond structure & properties

Diamond is the hardest known material and its exceptional properties, including chemical inertness, have ensured its extensive use in engineering and electronics, whilst its natural rarity and sparkle has made it extremely sought after as a gemstone.

Diamonds can be mined, or since the last century, produced synthetically in the lab. The discovery of lab-grown diamond techniques has allowed for more widespread use in research due to lower acquisition cost compared to mined diamond, and the ability to alter its chemical composition. In both synthetic and natural diamonds, nitrogen and boron are the main impurities and thus have a bearing on the diamond's properties.¹ Synthetic diamonds with an N impurity can surpass other diamond types in hardness and wear resistance, when the N concentration is 0.3ppm, allowing for greater applications.²

Diamond is seen as being a superior material and D. Araujo et al (2021) state that “among wide band gap semiconductors, diamond is considered to be the ultimate semiconductor for high-power electronics”.³ This is due to its excellent physical properties and how they compare to other materials, shown in table 1.

Table 1- The extreme properties of pure diamond (adapted from J. E. Field 1992⁴, P.W. May 2000⁵ and D. Araujo et al 2021³)

Property	Value & units	Comparable to other materials
Mechanical hardness	90 GPa	Extreme
Bulk modulus	$1.2 \times 10^{12} \text{ Nm}^{-2}$	Highest known
Compressibility	$8.3 \times 10^{-13} \text{ m}^2 \text{ N}^{-1}$	Lowest known
Thermal conductivity	$2 \times 10^3 \text{ W cm}^{-1} \text{ K}^{-1}$	Highest known
Thermal expansion coefficient	$1 \times 10^{-6} \text{ K}$	Very low
Resistivity	$10^{13} \Omega \text{ cm}$	Very good insulator
Band gap	5.4 eV	Semiconductor
Dielectric constant	5.7 ϵ	Low

1.1.1 Synthetic diamond applications

In engineering, diamond's extreme mechanical hardness ensures its use in materials such as diamond drill bits. Diamond also has applications in the optical field, due to its transparency through a large spectral range, from UV to IR, along with its outstanding physical and thermal properties.⁶ This explains its use in extreme situations, such as diamond windows used in corrosive environments, missile radomes, and diamond endoscopes for surgery.^{6,7} Electronically, diamond's applications are expansive, including electric transport, energy distribution, diodes and transistors.³ Diamond can also be used in detectors due to its wide band gap providing a low background current.^{3,8} Diamond detectors can be used for a range of detection capabilities, including for radiation detection, detection of toxic gas or for

the detection of viruses such as SARS-CoV-2.^{6,9,10} There have also been reports of diamond electrodes, for uses such as the reduction of CO₂.¹¹

The applications of diamond span many areas of research, a testament to its extreme properties, and this provides an insight into the desire to continue to research its capabilities, such as in this project.

1.1.2 Bonding in diamond

Carbon exists in group 4 of the periodic table, giving it the electronic structure s^2p^2 . These s and p states hybridise to form tetrahedral sp^3 bonds, which create the diamond lattice.¹² Other group 4 elements, such as silicon and germanium also form a crystal lattice in the same way, and they are also known for being excellent semiconductors along with diamond.¹² Silicon and germanium's semiconductor properties are due to their 4 valence electrons which mean that they can lose and gain electrons simultaneously, a property which diamond shares.¹³ Diamond has bulk modulus (listed in table 1) four times that of silicon, making it the superior material.¹²

Carbon exists in lattice form in both of its most common allotropes: diamond and graphite. A variation in bonding causes these two lattice types to exhibit differing properties. Diamond has sp^3 hybridisation whereas graphite has sp^2 . Diamond consists of a carbon lattice with each carbon equally spaced and in a tetrahedral shape, surrounded by 4 other carbon atoms.¹⁴ The carbon atoms in diamond "lie on two interpenetrating face-centred cubic lattices" giving a unit cell with the shape of a parallelepiped.¹⁴ Graphite is made up of layers of sp^2 bonded carbon atoms, with each layer stacked upon another by Van der Waals forces. The structures of carbon and graphite are shown in figure 1.

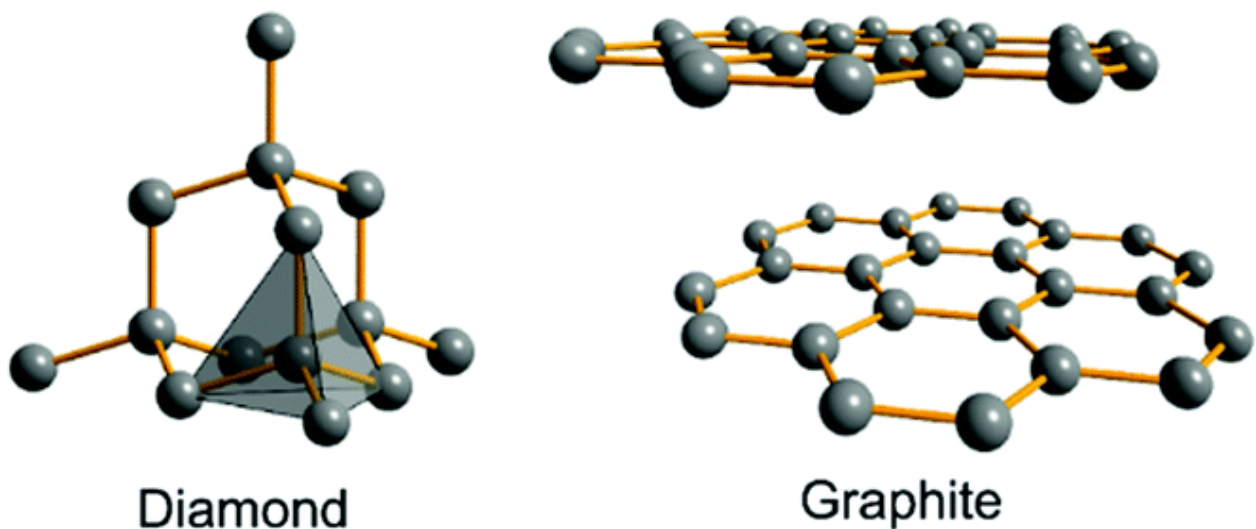


Figure 1- Comparison of the bonding in diamond vs in graphite (from I.V. Popov et al 2019)¹⁵

Carbon crystallised in the diamond crystal structure is in a metastable phase, as once it is formed it cannot spontaneously convert to graphite.^{5,16} The binding energy peaks for

graphite and diamond are very similar, separated by only 0.1 eV, (diamond 284.5 eV and graphite 284.4 eV).¹⁷ At RTP, graphite is scarcely more thermodynamically stable than diamond (within 2 kJ mol⁻¹), and diamond and graphite are seen as having a “quasi-degeneracy” (degenerate within 1 kcal mol⁻¹).¹⁵ Despite this, and with such a small difference between enthalpies of formation, graphite being 2.9 kJ mol⁻¹ lower than diamond, an extremely large activation barrier prevents easy conversion of graphite to diamond.¹⁸

1.1.3 Diamond classification

The presence or absence of boron and nitrogen, the two main impurities in diamond, and their configuration within the lattice, dictates how a diamond gets classified.¹⁹ These differences in the diamond lattice and their configurations are demonstrated in figure 2.

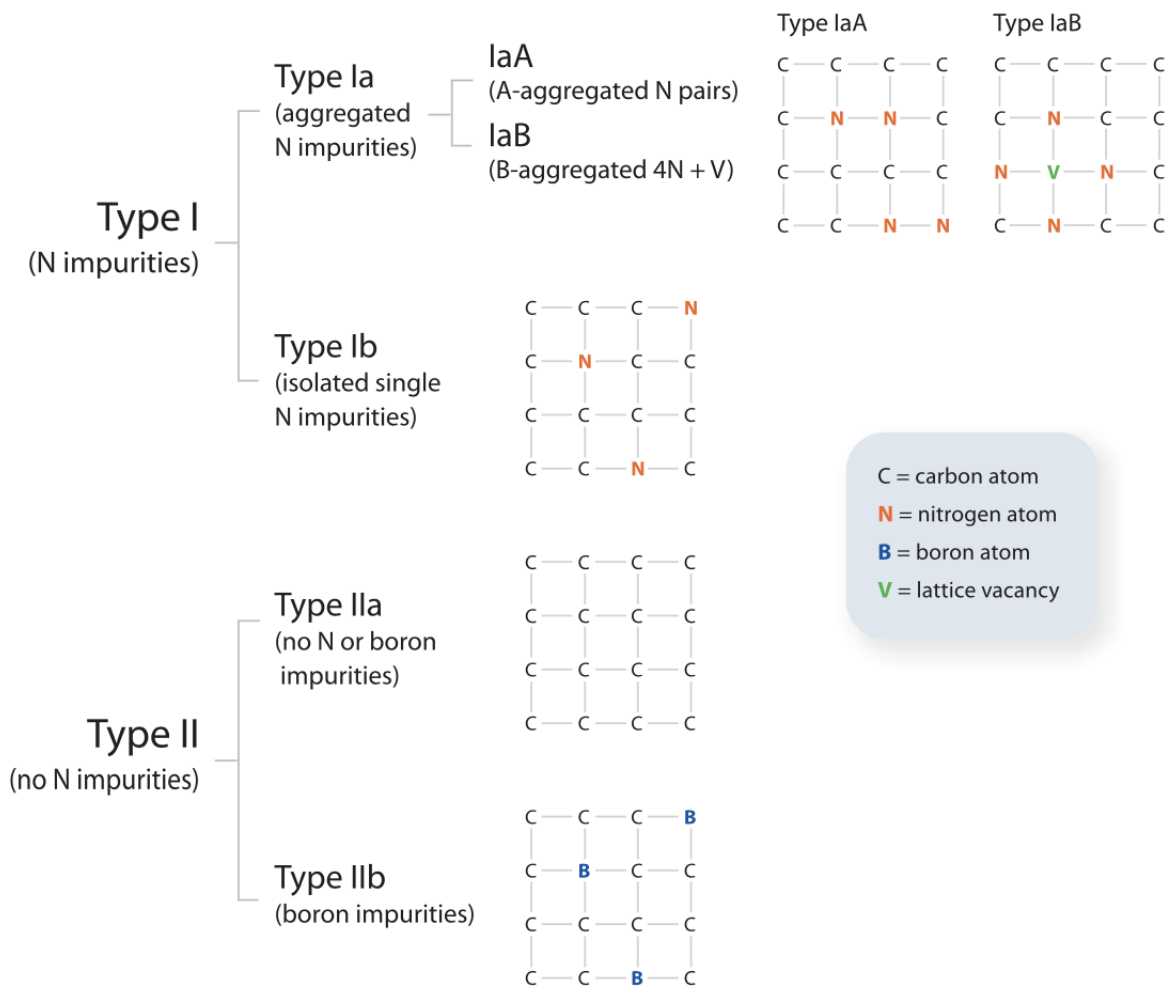


Figure 2- the classification of B or N doped diamonds (from C. M. Breeding and J. E. Shigley 2009)¹⁹

Type I diamonds contain nitrogen impurities and this is defined as being “sufficient N to be measurable by IR absorption spectroscopy”.¹⁹ Conversely, type II do not have a detectable amount of N.¹⁹ Within Type I diamonds there are two subgroups: Type Ia- where N atoms replace C atoms in the lattice, known as aggregated N impurities, or Type Ib – “isolated single N impurities”.^{3, 19} Type Ia diamonds make up the bulk of naturally occurring diamonds found, whereas diamonds grown synthetically are majority type Ib diamonds.^{19, 20} This classification difference could provide a way to differentiate between lab-grown and natural diamond.¹⁹

The reduction in nitrogen concentration in type II usually comes about from an increase in boron impurities.^{3, 19} Type IIa occurs when both B and N impurity content is low, and it is virtually free from impurity (purest diamond). When boron concentration exceeds nitrogen concentration, it is Type IIb.³ A Type IIb diamond is a p-type semiconductive crystal, due to the presence of boron, the rarest naturally occurring diamond, which is generally blue in colour.^{3, 20} Because of their rarity, type IIb diamonds made up just 800g out of 40 tonnes of naturally occurring diamond in 1990.²⁰

1.2 Diamond synthesis

1.2.1 High pressure high temperature (HPHT)

The first synthetic diamonds were made by the HPHT method. Initially in 1953 in Sweden using Fe₃C and graphite with HPHT conditions of 7.5 GPa and 1500°C, and then in the following year in the US using FeS and graphite at 7 GPa and 1600°C.²¹ The HPHT method replicates the way that diamond is naturally made within the Earth’s mantle.

Graphite has anisotropic bonding as the interatomic distance in the graphite layer is 1.42Å, with the distance between planes being 3.37 Å.²¹ It can therefore be proposed that applying pressure to graphite to shorten the bonds between layers and buckle the carbon rings, will convert it to diamond.²¹ This is the basis of the HPHT method of producing diamond, demonstrated in figure 3. In the HPHT synthesis, diamond is thermodynamically more stable than graphite, as can be seen in figure 4 where HPHT sits in carbon’s diamond phase.⁸ This differs from the other common method of making diamond, CVD, which sits in carbon’s metastable phase.

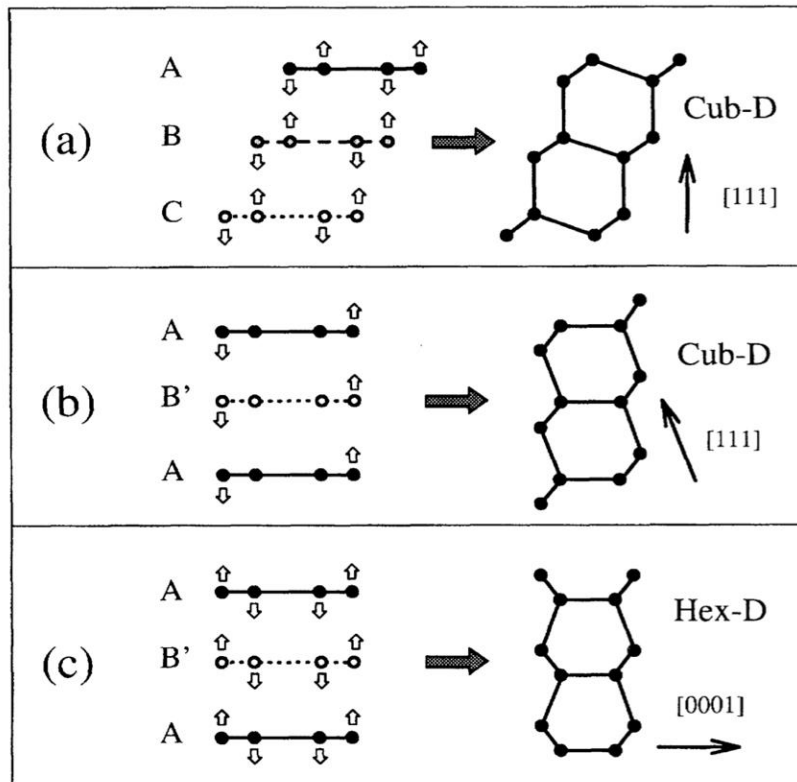


Figure 3 - Geometric paths for graphite to diamond formation: “a) rhombohedral graphite to cubic diamond, b) orthorhombic graphite to cubic diamond, c) orthorhombic graphite to hexagonal diamond” (from S. Scandolo et al, 1995)²²

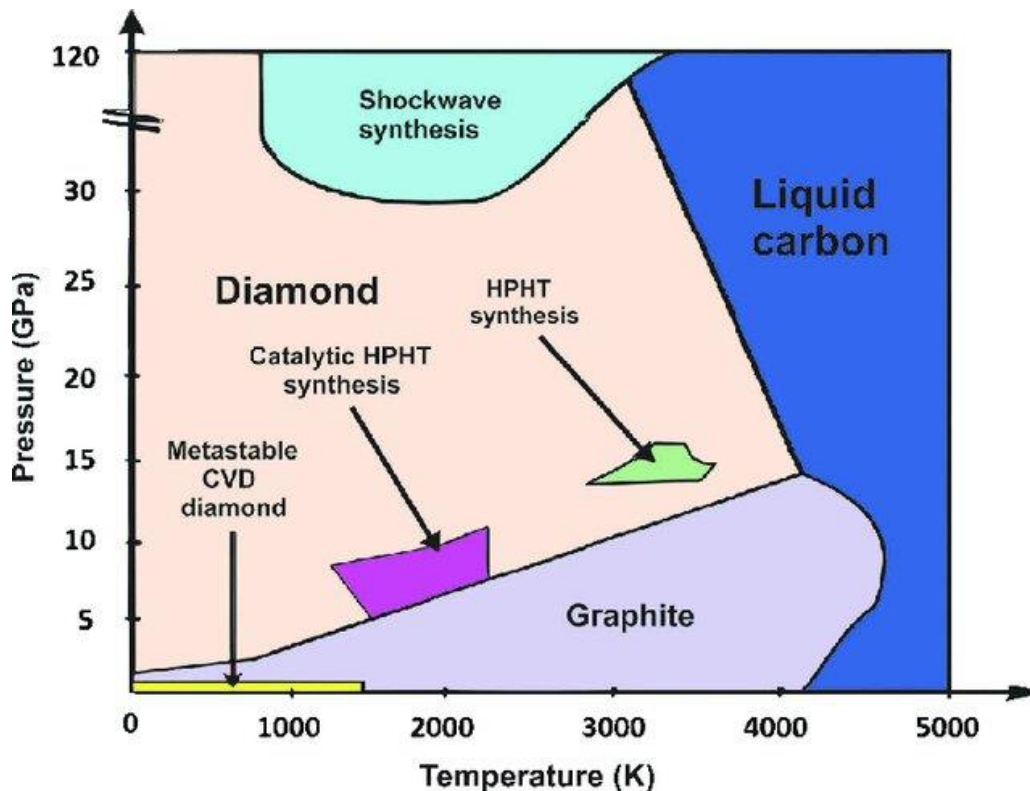


Figure 4 – Different carbon phases and allotropes and their required pressure and temperature (from S. Veljkovic et al, 2020)²³

1.2.2 Chemical vapour deposition (CVD)

Chemical vapour deposition is the process by which a chemical reaction of vapour-phase reactants forms a “thin solid film on a substrate”.²⁴ For diamond CVD, the process works by gas activation of methane and hydrogen: either by a hot filament (HF) or a microwave plasma (MP) reactor. Generally, HF is cheaper to run and can grow over larger areas, whilst MP has higher growth rates.²⁵ MPCVD is shown to grow high-quality diamond with superior optical and electric properties, and this was the technique used for growth in this project.³

The process of diamond deposition onto a substrate, by hot filament activation, is shown in figure 5. Gas activation by hot filament creates free radicals from the inputted gases and these deposit onto the substrate layer. MP CVD deposition follows the same process of gas activation and deposition, except that the gas activation occurs from plasma instead.

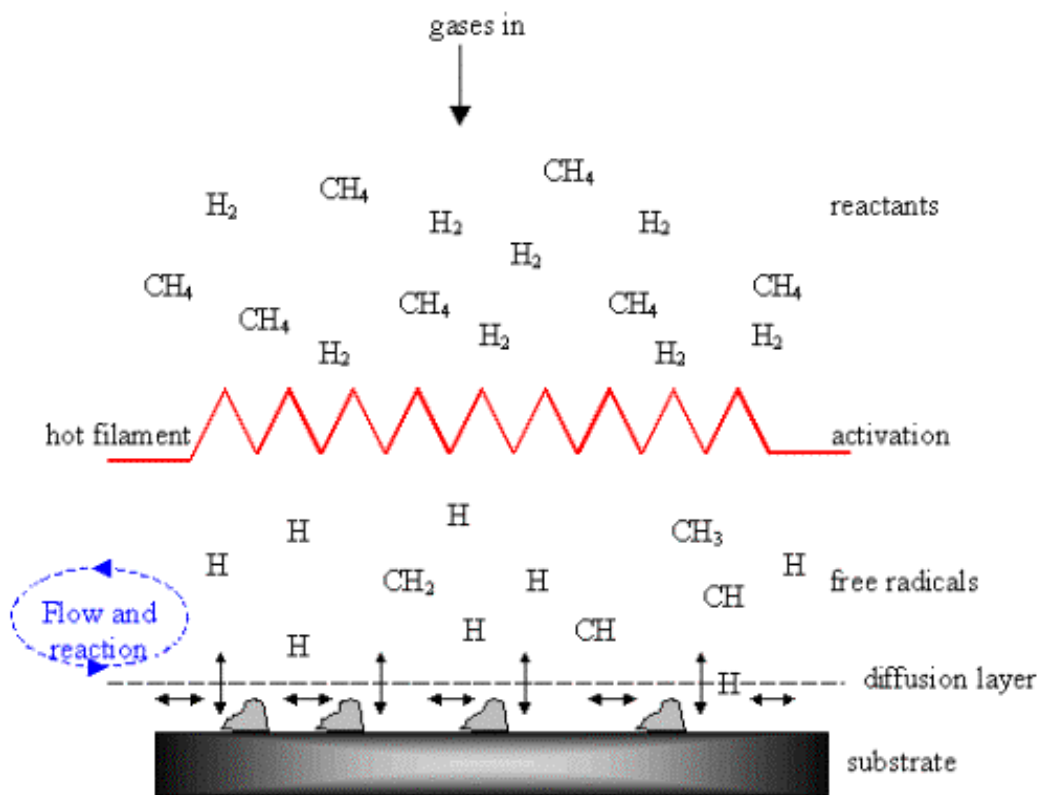


Figure 5- a schematic of the process of Hot filament CVD (from G. Pastor-Moreno, 2002)²⁶

CVD diamond growth was first patented in the United States in 1962, and latterly microwave-plasma CVD reactors became commercially available in the late 1980s.^{16, 27} The process works by utilising a carbon source, commonly methane, and growing highly crystalline films on crystalline substrates using a principally hydrogen-based plasma.¹⁶ Plasma is sustained throughout the growth by ensuring that the pressure isn't too high, or the microwave power isn't too low, as these two variables are dependent on each other.²⁸ As is seen in figure 4, the growth of CVD diamond is metastable, and it sits in carbon's graphitic phase. The thermodynamic conditions for growth of diamond via CVD favour graphite, therefore, and so hydrogen is used to suppress the deposition of graphite.⁸ Gas

phase atomic hydrogen sustains film growth by producing sites on the surface for methyl components to adsorb, and hydrogen radicals also remove any non-diamond carbon (e.g. graphite) that may form.^{3, 16} This is due to hydrogen strongly interacting with graphite but not with diamond, so called “selective etching”.²⁹

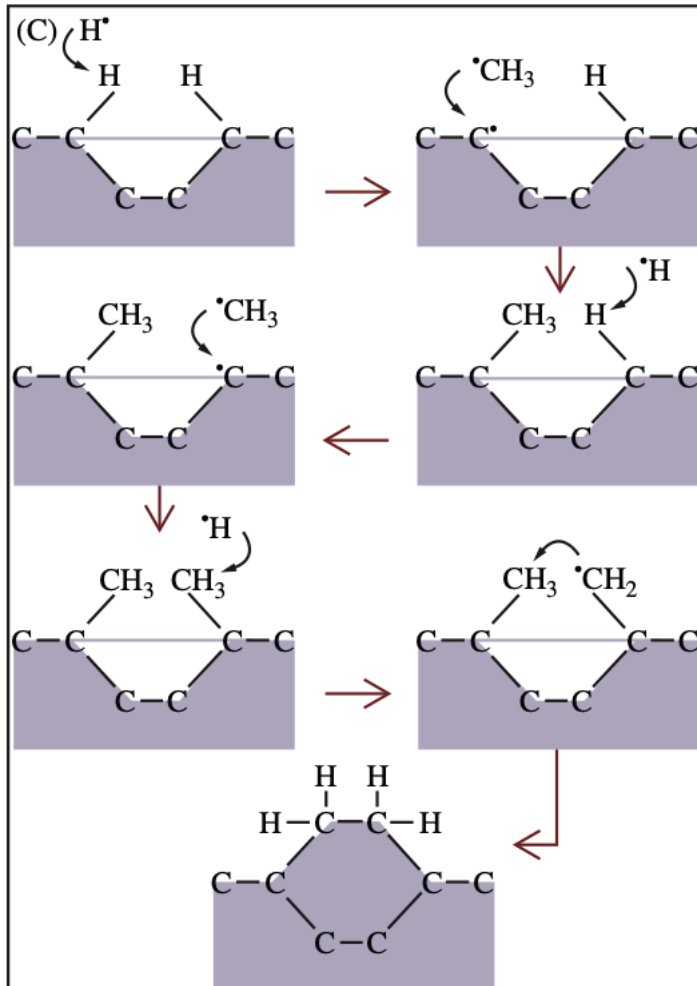


Figure 6- schematic of the stepwise addition of methyl species for diamond deposition (from M. Chandran)³⁰

Diamond growth was found to only be possible when the carbon gas source contained a methyl group, and that other hydrocarbon gases (e.g. benzene) that don't contain methyl groups, didn't contribute to thermal growth of diamond.⁸ This is because the methyl radicals generated in the CVD process are necessary for diamond growth.⁸ The process of the methyl and hydrogen radicals interacting to form a diamond lattice is shown in figure 6. This diagram is indicative of the generic mode of CVD deposition, and visibly shows why gases with a methyl group are necessary.

CVD utilises low pressure to form diamond, and this has been described as a “kinetic non-equilibrium process”, due to graphite also being thermodynamically stable under the same conditions.³¹ However, these traditional kinetic models of diamond growth are unable to account for “the nucleation of diamond on non-diamond surfaces”, therefore a quasi-thermodynamic model, comparing the change of binding energy caused by vacancies in the

diamond lattice, is useful to understand how diamond can form on silicon.³¹ These energetics models came from the 1989 study from Bar-Yam and Moustakas, which also outlined that diamond became more stable than graphite due to vacancies on the diamond surface, as these changed the relative binding energies.³¹ This proved that a large vacancy concentration, caused by low-pressure conditions, aided the growth of diamond films.³¹ Their work also proved that due to the vacancies stabilising the diamond, defect free diamonds were very difficult to grow, and as such they proposed doping to be an effective way to grow diamond with lower vacancy concentrations.³¹

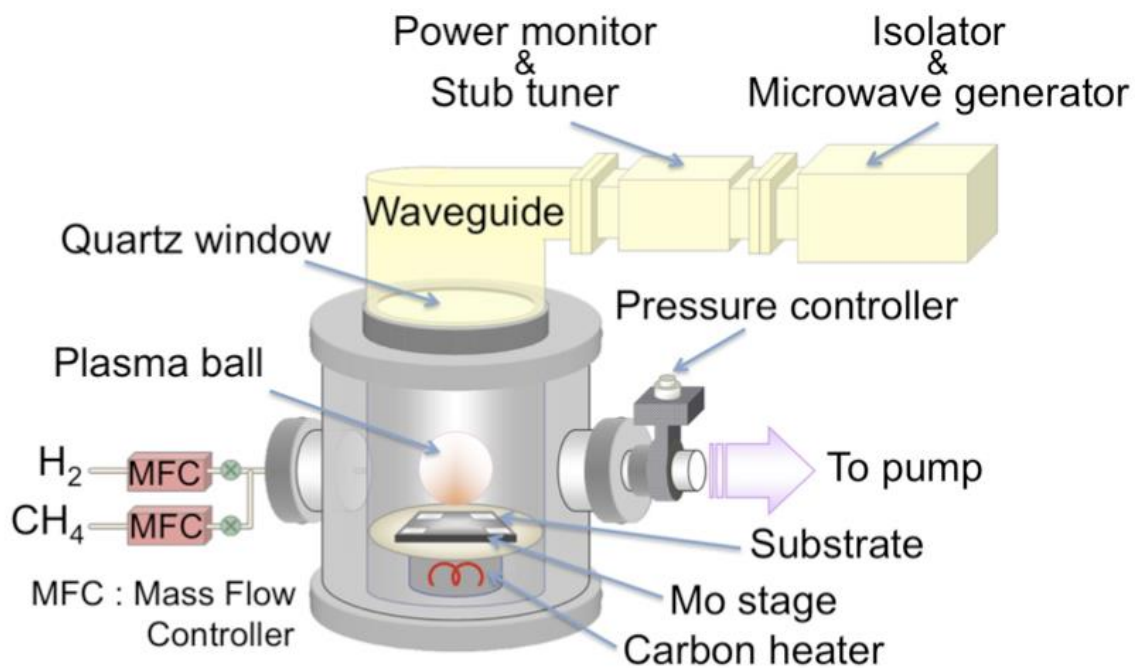


Figure 7- A diagram of a standard MW CVD reactor (from M. Hiramatsu et al, 2014²⁸)

It has been found that MPCVD with a high plasma density (~5 kW MW) gives a higher growth rate for diamond growth, compared to growth with a lower plasma density.³² A high growth rate has been found to cause a decrease in impurity incorporation per unit time from the atmosphere.³² Having a high growth rate (R_g) of diamond whilst maintaining crystal quality is a barrier to MPCVD being used more extensively. The growth rate depends upon “the ratio of methane flow to the total source gas flow”, increasing proportionally to the R_g, however this comes at the detriment of the diamond layer quality.³ The methane ratio can be calculated using equation 1.

$$C_{me} = CH_4 / (H_2 + CH_4) \quad (1)$$

Increased carbon atom concentration in the gas mixture causes a less effective sp² etching process, by hydrogen.³ This contributes to increased surface roughness and defects caused by the “formation of secondary-nucleated non-epitaxial crystallites and non-diamond phases”.³ A C_{me} below 1.0% gives rise to the high-quality (100) diamond films and the typical

R_g is < 1 μm / h although this can be improved with higher MW power.³ Figure 7 shows the set up of a standard MPCVD reactor, with the plasma, source gas input and substrate labelled.

1.2.3 Substrate choice & preparation

Diamond can be grown on both single crystal diamond substrates and non-diamond substrates (commonly silicon and molybdenum). This growth on non-diamond substrates can be made possible by the addition of atomic hydrogen into the reaction, due to its graphite removing properties.²⁹ Growth on non-diamond substrates can also be achieved as the substrate surface forces have a weak effect on the nucleation, when compared to the strong effect of CVD.²⁹ The preparation of the substrate plays a large role in the growth, as “spontaneous nucleation of diamond crystals” is seen predominantly on defects on the substrate surface, like grain boundaries and scratches.²⁹ A focus on this can prove that diamond nucleation takes place on the substrate itself and not in the gas phase.²⁹

Silicon can be used as a substrate due to its similar thermal properties to diamond, and its much lower cost, and it was used in the research conducted for this project.¹⁶ There are two ways to prepare the substrate; either by manual abrasion of the silicon surface with fine diamond powder, or by electrospray apparatus. It has been found that substrate preparation ensures diamond growth layers ‘stick’ onto the substrate and enhances the diamond nucleation density.³³ Once diamond nucleation has occurred, diamond crystals grow horizontally and then vertically, demonstrated in figure 8.

The rate of diamond nucleation depends on various factors. The method of substrate preparation affects the nucleation, and as does the substrate itself.²⁹ Substrates that form carbides (silicon, molybdenum, tungsten) have a rate of nucleation 1-2 orders of magnitude greater than non-carbide forming substrates, such as copper or gold, this has been found to be especially dominant in their polycrystalline forms.²⁹

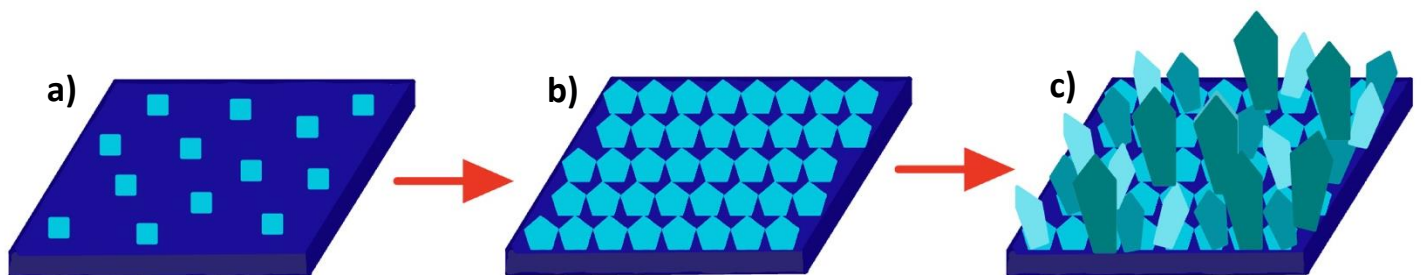


Figure 8- A diagram showing the steps of growth of diamond on a Si substrate, a) Si surface seeded with fine diamond powder, b) nucleation of individual diamond crystallites, c) rapid vertical columnar growth (inspired by work from L. Krishnia and P.W. Tyagi, 2018)

1.2.4 Crystal orientation

The orientation of the diamond crystals grown can vary due to the substrate orientation, whilst also being affected by increases in the substrate temperature.⁸ Crystal shape can change from octahedral to cubic via cubo-octahedral intermediates, this pathway is shown in figure 9.⁸ When considering the orientations of the diamond made in this project, these intermediates have been referred to.

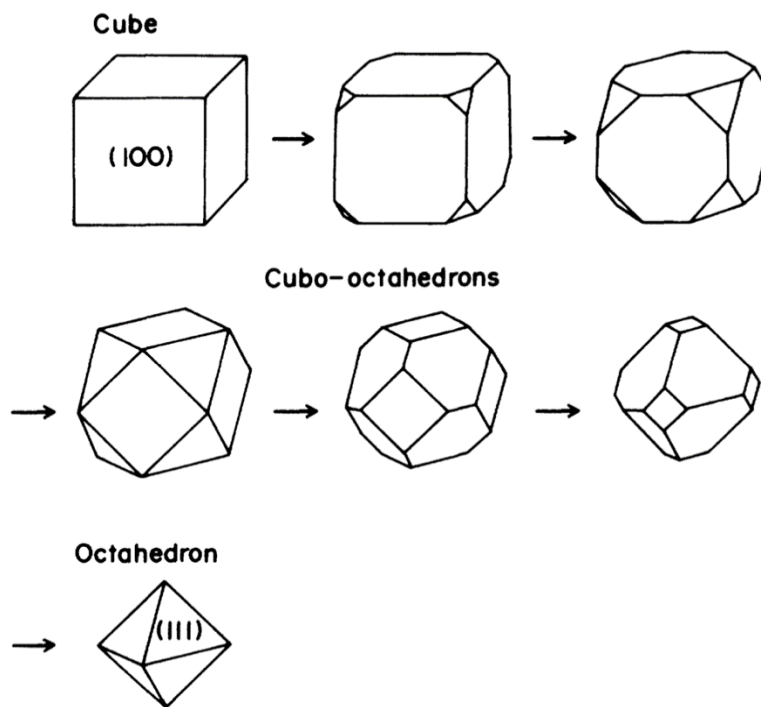


Figure 9 – The polyhedrals of diamond. The process of crystal shape changing from cubic to octahedral via cubo-octahedral states. (from K. Kobashi et al 1988)⁸

1.3 Band gap theory

The band gap is the space between the conduction and the valence bands in a material. The size of the band gap determines whether the material is a semiconductor or an insulator, these are shown compared to metal (no band gap) in figure 10.

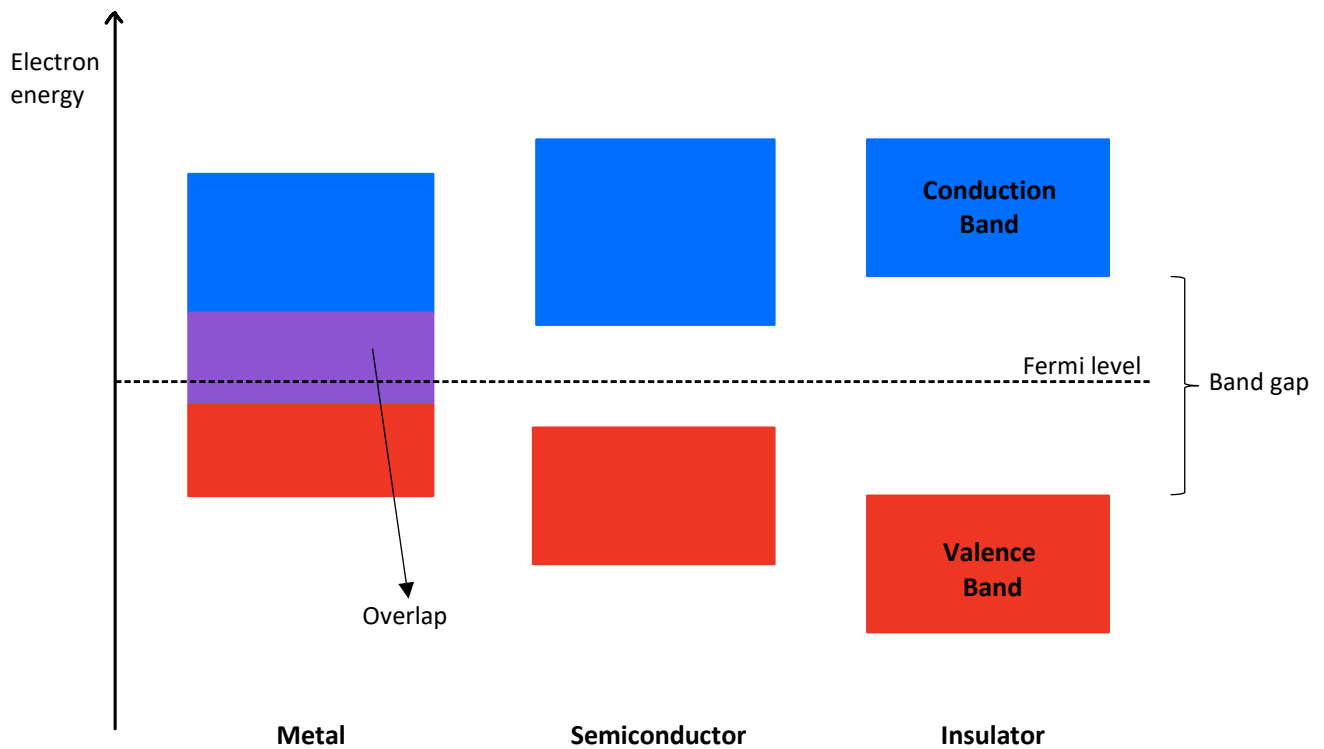


Figure 10- diagram showing the conduction and valence bands of metals, semiconductors, and insulators

1.3.1 Semiconductors

An intrinsic semiconductor exists when the Fermi energy (E_F) of a material is exactly in the middle of the band gap (E_g). This is demonstrated in figure 11:

- (a) shows an intrinsic semiconductor ($E_F = \frac{1}{2} E_g$)
- (b) a n-type semiconductor ($E_F > \frac{1}{2} E_g$)
- (c) a p-type semiconductor ($E_F < \frac{1}{2} E_g$)

Intrinsic diamond has p-type semiconductor characteristics.³² For this project we are aiming for n-type materials, and so for a fermi level close to the conduction band, this is illustrated in figure 11b.

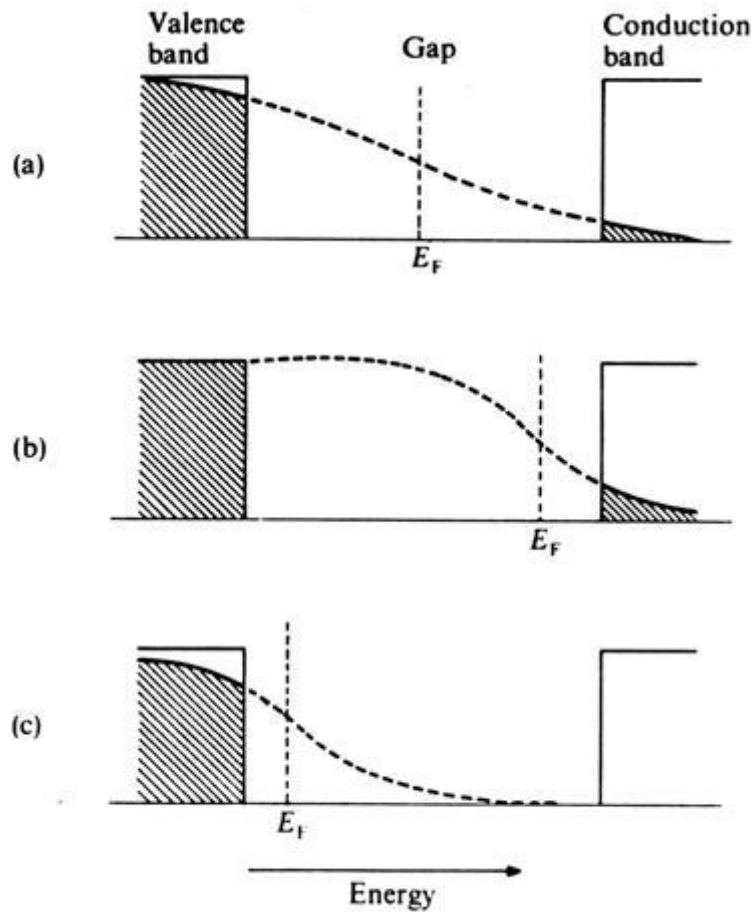


Figure 11- Fermi-Dirac distributions in semiconductors (shading represents occupied levels). (a) pure solid, (b) n-type, (c) p-type, semiconductors. (From P.A. Cox, 1987)³⁴

1.3.2 Fermi level

Analysis techniques can determine positions within the band structure. In this project UPS is used, and this technique is explained in section 1.6.4. The information received from UPS is the work function and the valence band maximum. Shown in figure 12 is the vacuum level (E_{VAC}) which is defined as being the “energy level of an electron with zero kinetic energy with respect to the sample surface”.³⁵ The vacuum level is “strongly influenced by the nature of the surface”, and the difference between this and the VBM is the ionisation energy of the system.³⁵ The valence band maximum and conduction band minimum can also be referred to as the HOMO and LUMO, respectively.³⁵

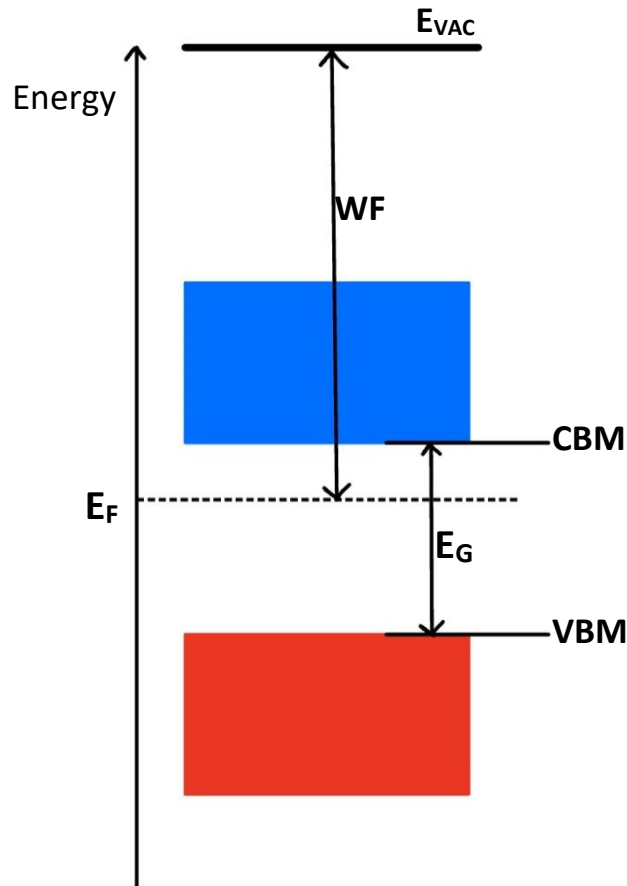


Figure 12- Representation of the key parts of the band structure referred to in this project (adapted from A. Kahn, 2016)³⁵

The work function is the difference between the positions of E_{VAC} and E_F and can be determined by UPS, it is therefore dependent on both E_{VAC} and E_F .³⁵ The WF can be influenced by temperature, carrier density and, most pertinent to this project, by concentration of dopants.³⁵ It is expressed as $WF = E_{VAC} - E_F$.³⁵

As Fermi energy can be “controlled by electron bombardment”, Bar-Yam and Moustakas’ 1989 paper theorises that electron-rich conditions facilitate easier growth of p-type materials whereas electron-poor conditions, from a positive ion, are conducive to n-type growth.³¹ Kato et al stated in their 2016 paper the importance of the Fermi level when considering diamonds applications.³² Their research confirmed that within diamond the charge of a nitrogen vacancy complex (NV^+ , NV^- , NV^0), impacted upon the diamond layer’s Fermi level.³² They also stated that quantum and magnetic sensing applications are reliant upon the NV^- charge state, showing the importance of band structure for applications of diamond.³² These papers both confirm the principle behind dopant impurities (holes or carriers) causing a shift in the Fermi level.

Since Fermi energy is proportional to the work function, this known theory of Fermi energy shifting due to doping could be used by way of an explanation for the changes in the value of the WF. It has been demonstrated that p-type doping shows a trend of increasing the WF

of the material, which can be explained using the band structure diagram in figure 12.³⁶ With p-type doping the E_F moves towards the VBM, and thus the distance between it and the E_{Vac} , also known as the WF, increases and the opposite effect would be expected for n-type doping, with a lowering of the WF.

1.4 Doping in diamond

Dopants are an impurity in the diamond lattice which can be used to manipulate the properties of the diamond made. The principle behind doping is “adding a material that can donate or remove electrons” which in turn alters the electronic properties of the starting material.³⁷ There are various types of dopants, methods of incorporating them, and ways in which they are successfully incorporated.

1.4.1 n-type vs p-type dopants

N-type dopants are a donor impurity that contribute free electrons, whereas p-type dopants are an acceptor impurity and create holes for electrons to fill, this is demonstrated in figure 13. In n-type conductivity, electrons are the main carriers and holes are the minority carriers, which leads to a Fermi energy level closer to the conduction band, (b) in figure 11. This project aims ultimately to achieve n-type conductivity.

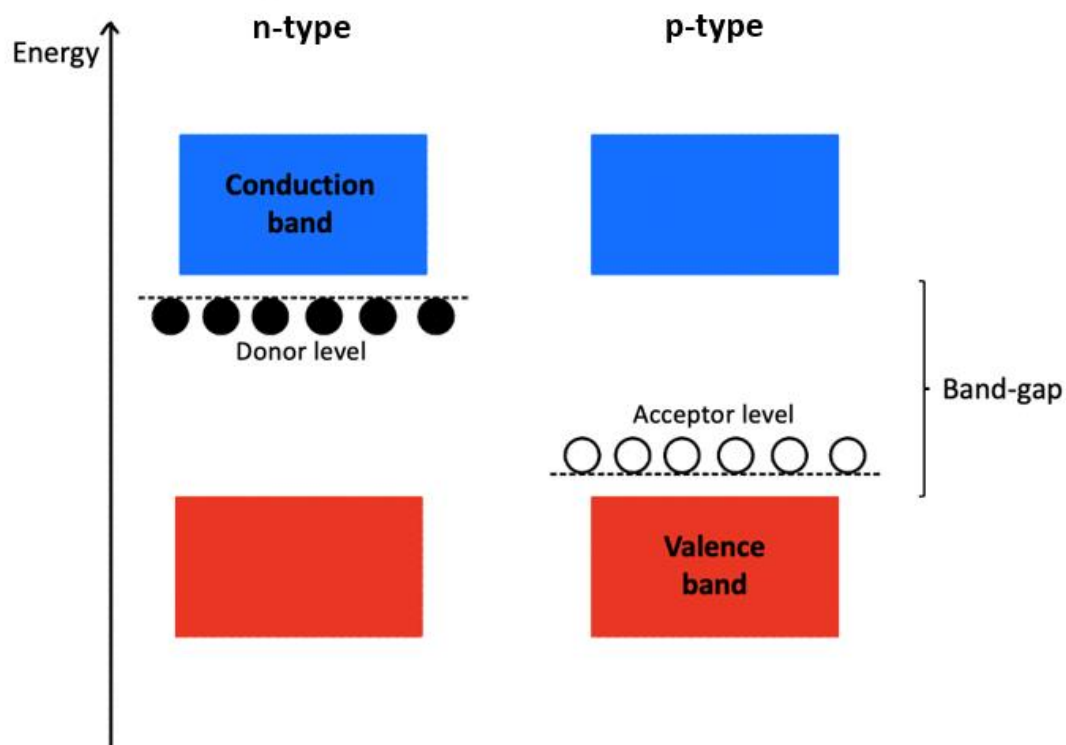


Figure 13- A demonstration of how p-type and n-type dopants sit within a material's band structure

Common n-type donor elements for diamond include Li, Na, N, S, P and O, with the majority of studies focused on N and P.³⁸ P's donor level sits closer than N below diamond's conduction band minimum, making P a more effective donor, with P = 0.57 eV and N = 1.7 eV.³⁸ However, the limitation of using phosphorous as a donor atom over nitrogen is their atomic size difference. Nitrogen sits beside carbon in the periodic table, so carbon's atomic radius 0.77 Å is similarly sized to nitrogen's 0.74 Å, especially when compared to phosphorous' atomic radius of 1.06 Å.³⁸ Too dissimilarly sized atoms (such as C and P), will ultimately lead to "terminal failure" of n-type diamond semiconductors due to increased defects and deformed crystal grains.³⁸ This is the basis behind pushing for N to be perfected as an n-type dopant in diamond.

1.4.2 Nitrogen doped diamond

Nitrogen is the major impurity in both synthetic and natural diamond, and it fosters the establishment of sp² carbon.^{39, 40} As previously mentioned, nitrogen is an n-type dopant, giving rise to deep donor levels of 1.7eV, which can only be activated > 420°C, hence n-type doping at room temperature is a challenge.^{25 40 41} However, when nitrogen is a donor pair complex, the N-N pair has been shown experimentally by R. J. Eyre et al to have donor level -3.8 eV, agreeing with previous data.⁴⁰

When nitrogen is used as a co-dopant (eg in BNDD), the concentration of nitrogen strongly influences the growth rate of the crystal.²⁵ A small amount of nitrogen accelerates the growth, whereas as the amount of nitrogen increases too much, the growth is inhibited, and the crystallinity of the crystal is affected.⁴² Nitrogen doping in small amounts also affects surface morphology, creating rougher surfaces and forming more 100 instead of 111 diamond faces.⁴¹ Higher amounts of nitrogen are party to less-well orientated and smaller crystals, with a higher amount of sp² carbon.⁴¹ Nitrogen is not seen as being a useful dopant for electronics when by itself.

1.4.3 Boron doped diamond

Boron is an electron accepting dopant in the diamond lattice, having one less valence electron than carbon and therefore creating holes in the valence band to make p-type diamond.^{1, 25} Like nitrogen, boron also sits next to carbon in the periodic table meaning it is an ideally sized atom for diamond doping. The boron acceptor level has been found to be 0.37 eV above diamond's VBM, which gives it advantageous properties for use in electrical devices such as: electrochemical sensors, wastewater treatment, electron field emission devices and as electrodes for supercapacitors.²⁵ Boron doping mostly has the effect of increasing conductivity, with literature stating that a "doping concentration of ~ 10¹⁸ cm⁻³, transforms insulating diamond to semiconducting diamond".⁴³ However, high pressure and high temperature BDD preparation produces diamond with high resistivity, so this method of diamond growth isn't conducive to high conductivity, and CVD should be used instead.¹

In conjunction with its good conductive properties, high B doping does also degrade the quality of the diamond crystal, affecting the mechanical and optical characteristics, and thus causes ~10% of doped B atoms to be unable to act as acceptors.^{1, 43} As such, it is important to ensure that the B concentration allows the diamond to sit in a happy medium of good

diamond growth and good acceptor and electronic properties. There is discussion surrounding the effect of boron doping upon the growth rate of diamond films, some literature illustrates that boron decreases the strong nitrogen growth effect, whereas others demonstrate boron increasing the growth rate.^{25, 44-46}

When boron is used in a reactor, subsequent samples will have an inevitable contamination of boron, therefore the boron concentration in these reactors can never truly be zero. This is known as the “memory effect” and describes the deposition of boron oxide in the reactor due to boron usage and means that boron is continually reintroduced in the gas phase.²⁵ This is important to note when considering ratios of boron, as it will likely be higher than anticipated.

1.4.4 Theory of co-doping

Co-doping is a method used in wide band gap semiconductors, such as diamond, to improve their electronic properties by decreasing their resistivity. In this project it is used with the aim of realising nitrogen as an n-type dopant.

Co-doping works by:

- *Reducing the formation energy of the complex:* the attractive acceptor-donor interaction overcomes any repulsive interactions due to reduced lattice relaxation and Madelung energies.⁴⁷ A low formation energy (ideally negative) ensures the effective incorporation of co-dopants.
- *Increasing carrier mobility:* from short-range dipole scattering.⁴⁷
- *Reducing energy level of acceptors:* as forming a donor-acceptor complex raises a donor energy level and lowers an acceptor level.⁴⁷

Katayama-Yoshida et al, state that “co-doping is an efficient and universal doping method” to avoid carrier compensation, increase activation rate and increase carrier mobility.⁴⁸ The same authors had written a theoretical prediction of co-doping 3 years prior (1998) which detailed the challenge of creating low-resistivity n- and p-type wide band gap semiconductors as ‘uni-polarity’ or ‘mono-polarity’ occurred.⁴⁷ For diamond, it was very difficult to produce low-resistivity n-type diamond, hence they found that co-doping was necessary.⁴⁷ Acceptors and donors were doped simultaneously, which produced a meta-stable acceptor-donor-acceptor complex in p-type semiconductors, or donor-acceptor-donor complexes for n-type.⁴⁸ The chemical trends of these D-A-D structures are, shallower donor levels when moving down a group, and reduced binding energy.⁴⁰ The D-A-D arrangement is optimal when large atoms are involved, however for smaller atoms the lower energy arrangement is D-D-A.⁴⁰

1.4.5 Methods of dopant incorporation

Substitutional doping

This is the most common method of doping in literature, which works by incorporating dopants in the gas phase. Carbon atoms are substituted by dopant atoms, for example in a

diamond lattice and this method has also been used when doping graphene by H. Yoo et al.³⁷ This can be done using CVD apparatus, by including the dopant gases in with the methane and hydrogen for the diamond growth. This method was used for this project and involved N₂ and B₂H₆ gases being injected into the reaction chamber simultaneously with hydrogen and methane.

Thermal decomposition

The work of Q. Liang et al utilised a decomposition method of dopant incorporation.⁴⁹ An inert hexagonal boron nitride powder was placed between molybdenum substrate holders, and as it decomposed, boron was supplied into the reaction system (*via* solid state diffusion).⁴⁹

Surface doping

K.G. Crawford et al call their surface dopant method “surface transfer doping”.⁵⁰ It involved exposure of hydrogen terminated surfaces to other gases, including NO₂, NO, SO₂ and N₂.⁵⁰ It was found that the exposure to NO₂ lowered the sheet resistance of the sample.⁵⁰

Thermal diffusion of doped substrates

Thermal diffusion of heavily boron doped silicon substrates was demonstrated by J-H Seo et al to boron dope single crystal diamond.⁵¹ Their method consisted of a “vacancy exchange boron doping mechanism” at the silicon-diamond boundary, which was said to reduce graphitisation and increase crystal quality.⁵¹ Y. Yang et al also employed a novel thermal method to nitrogen dope diamond films.³⁸ A Si₃N₄ substrate was used with HF CVD to provide a high enough temperature to pyrolyze the substrate, providing higher levels of nitrogen than if nitrogen was just introduced in the gas phase.³⁸ Their work provided a method to synthesise “super high-concentration” N-doped diamond films.³⁸

1.4.6 Boron nitrogen co-doped diamond (BNDD)

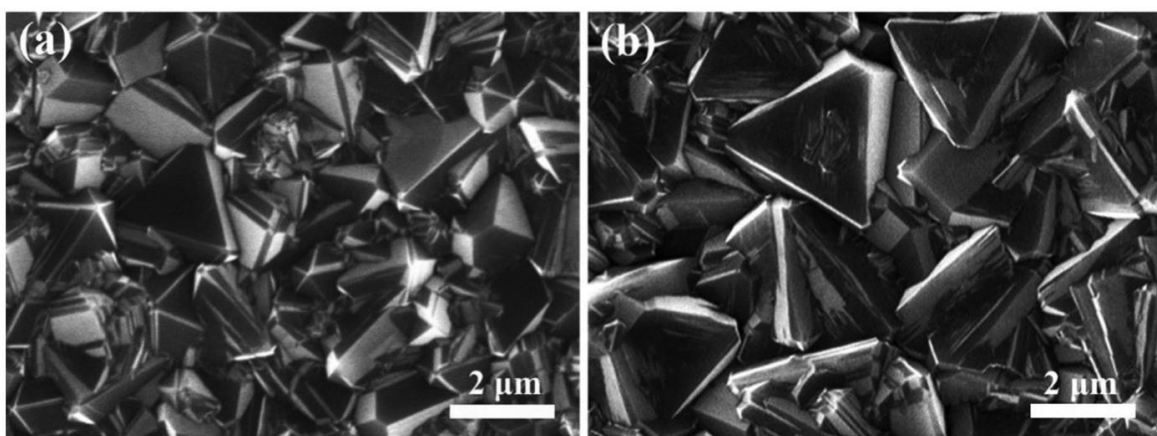


Figure 14- SEM images of the morphology difference between (a) BNDD and (b) BDD (images from the research of J. Li et al, 2021)⁵²

The choice of boron and nitrogen as co-dopants in diamond is due to their atomic size, as explained earlier in this section. They sit either side of carbon in the periodic table which

makes them ideally sized for effective dopant incorporation, and boron's p-type nature and nitrogen's n-type nature can work together to achieve n-type conductivity. As stated by R. J. Eyre et al "it is extremely difficult to achieve excellent performance of diamond semiconductors via single-element doping" and therefore co-doping became a useful way to achieve this.¹ BN co-doping improved the electrical and electrochemical properties of the diamond, and a change to the morphology and composition of the diamond grains was induced, as seen in figure 14.⁵³

Work by Q. Liang et al (2009) proves that when boron and nitrogen are present within the diamond lattice, they contribute to "enhanced fracture toughness" of the material showing that their uses as dopants also extend beyond the electronics field.⁴⁹ This isn't explored within the scope of this project however, but is interesting to note when exploring the benefits of doping in diamond.

When compared to just single doped diamond, it can be said that the "enhanced incorporation" effect of nitrogen allows BNDD to have greater boron concentrations than for just BDD.³⁹ BNDD is also shown to be a superior electrode with improved electrochemical performance compared to BDD electrodes.³⁹ Via XPS spectra, T. Guo et al proved that BNDD films have greater fractions of carbon (in C=O and C-O bonds) and higher sp²/sp³ ratios than BDD films, suggesting that the introduction of nitrogen into the film is responsible for these differences, as nitrogen induces sp² carbon growth.³⁹

1.5 Previous synthesis of B N co-doped diamond

The Katayama-Yoshida group calculated a low-resistivity n-type diamond using *ab-initio* molecular dynamics simulations with co-doped acceptor-donor supercell complexes with relaxed atoms (64 of C, P, N, B and H).⁴⁷ This ab initio molecular dynamics simulation showed N-B-N to be the most stable atomic configuration in diamond.⁴⁷ Using an N donor and B acceptor pair for co-doping reduced the lattice relaxation energy, through B boosting the solubility limit of N, and avoided bond breaking by creating a delocalised shallow donor state.^{43, 47} The BN co-doped diamond raised the N donor level to the vicinity of the CBM from 1.7 eV below.⁴⁷ The proposed diamond structure was B + 2N, and this was published in both the 1998 and 2001 papers.^{47, 48}

Results from Eyre et al (2007) were in agreement with the aforementioned Katayama-Yoshida et al group, confirming N-B-N to be the ideal configuration in diamond.⁴⁰ Both of these groups used modelling to achieve this result, (Eyre's group used first principles density functional simulations) so it became pertinent to prove that this could be done in practice as well as in theory.⁴⁰

The need for nitrogen-rich diamond rather than boron-rich was also reported by Hartmann et al (1997). They detailed that a high concentration of boron favoured the deposition of

graphite, and that the influence of B and N co-doping was the formation of graphite alongside the formation of diamond.⁵⁴

Croot et al (2018) also suggested that boron-rich doping would be detrimental to n-type diamond, asserting both BN_2 and BN_3 to be ideal structures.⁵⁵ These are shown in figure 15, alongside other potential BN clusters: BN and BN_4 .⁵⁵ It was stated that doping both B and N atoms into diamond would have the effect of increased electrochemical potential and decreased charge-transfer resistance, whilst catalyst active sites for redox reactions would also be created.⁵²

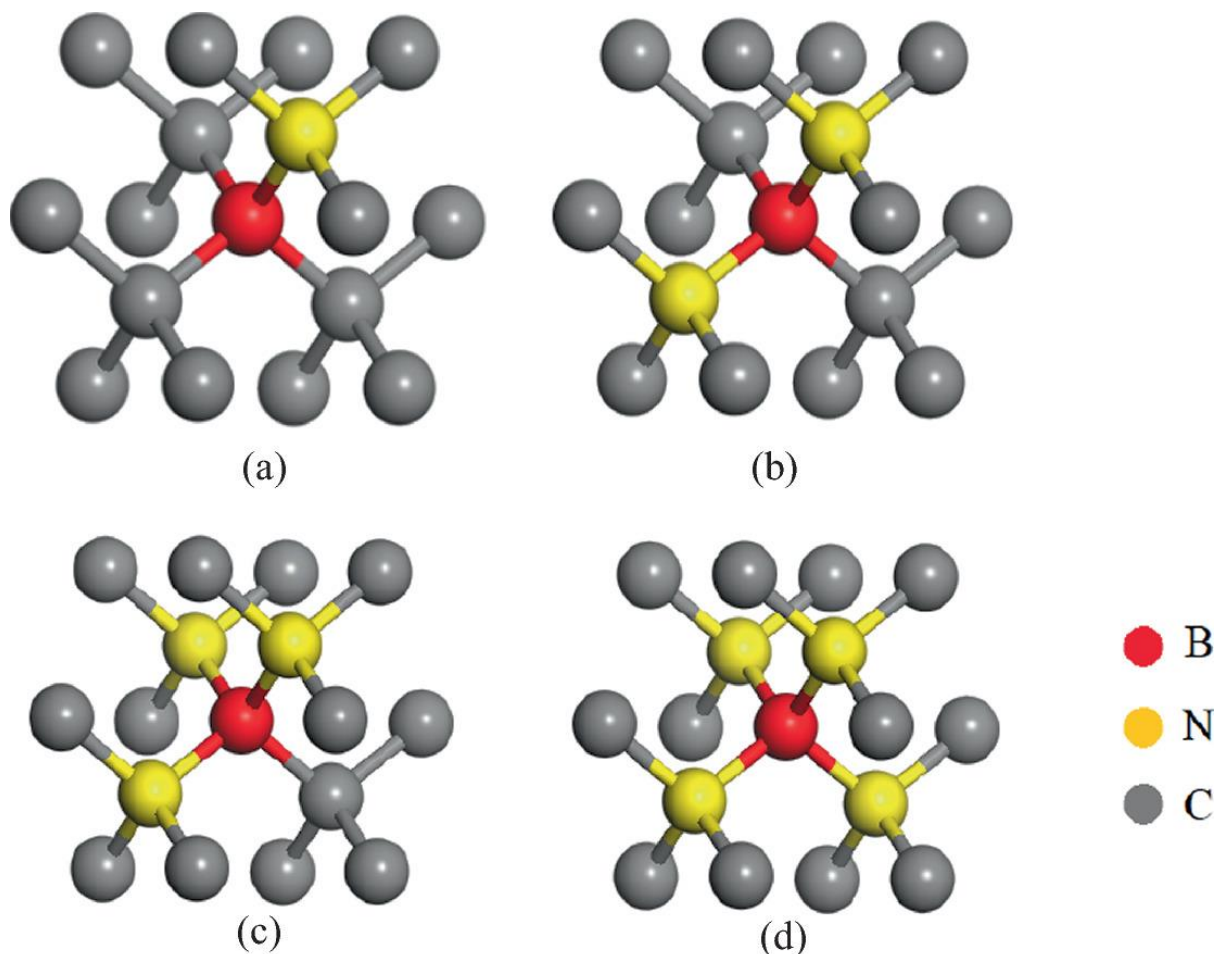


Figure 15 -BN1, BN2, BN3, BN4 clusters within a diamond lattice (from D. Zhou et al, 2022)⁵⁶

An experimental method *via* microwave plasma CVD was listed by D. Y. Liu et al (2021).⁵⁷ CH_4 had a flow rate of 20 sccm and H_2 of 500 sccm.⁵⁷ The B_2H_6 to CH_4 ratio was at 50 ppm for all the samples, whilst the N_2 to CH_4 ratio was varied at 0%, 2.5%, 5.0%, 7.5% and 10%.⁵⁷ Other conditions included: substrate temperature at 900°C , chamber pressure at 3.8 kW and chamber pressure at 160 Torr.⁵⁷ Increasing the nitrogen ratio increased the thickness of the substrate.⁵⁷ The group's results demonstrated n-type conductivity at 773K in boron nitrogen co-doped diamond in the form N-B-N.⁵⁷ This structure practically confirmed the previous *ab initio* work.^{40, 47, 48, 54, 55}

The focus of all prior research mentioned, was that the diamond doped clusters must be more N-rich than B-rich, and, as such, the research for this project ensured that it agreed with this.

In 2017, Y. Liu et al created BNDD for use as an electrode for CO₂ reduction via HF CVD, using a CH₄ /B₂H₆ /N₂ /H₂ gas mixture with constant 2.5% CH₄ and 12.5% B₂H₆ and varied N₂ levels of 2.5, 5 and 10%.⁵⁸ It was found that only at 2.5% N₂ did the diamond have (111) morphology, whereas at higher (5% and 10%) N₂ levels, morphology changed to predominantly (220).⁵⁸ This attests that the higher nitrogen levels cause significant variation in the crystal growth direction of BNDD. As this paper criticised high nitrogen concentrations, and previous research stated it being key, it is still important to vary nitrogen concentration to find the optimal amount when carrying out research for this project.

MP CVD BN co-doped diamond was produced by S. Kunuku et al (2022), by keeping hydrogen, methane, and nitrogen constant and varying the boron concentration.⁴³ Generally, syntheses vary the N/C ratio, so this was especially interesting to see. The B/C ratio was varied at 2500, 5000 and 7500 ppm, fixing the nitrogen flow to 0.12 sccm giving a N/C constant ratio 0.02.⁴³ They concluded that the variation of B concentration had a significant effect on the composition of the diamond layer and the chemistry of the plasma.⁴³ They concluded by XPS analysis that “higher B concentrations impacted the increase of N incorporation into the diamond layers”.⁴³ Increased B/N ratios were also shown to form increased density NV centres, due to the reduction of nitrogen precipitation.⁴³

High pressure high temperature methods have also been used for BNDD. The 2017 paper by M. Hu et al, details a methodology of creating BN co-doped diamond crystals by doping a carbon system with B and N atoms, using an FeNiCo solvent catalyst via a temperature gradient of 1300-1550°C at 5.3-5.8 GPa.¹ A “China-type large volume cubic high-pressure apparatus (CHPA, SPD-6 x 1200)” was used.¹ The group’s research shows B, C and N to form stable chemical bonds with each other, and the (100) and (111) crystal faces displayed different surface characteristics and growth due to their one vs two unsaturated bonds, respectively, for atoms on the surface.¹ The (100) face appeared to show a defect more easily than that of the (111) crystal face.¹

A 2023 synthesis from Wang et al followed on from this by using the same CHPA SPD-6 x 1200.⁴² The conditions were 5.6 GPa and 1300-1350°C, using a temperature gradient like before, but the catalyst contained manganese not iron, and is a Ni-Mn-Co alloy.⁴² Results showed the growth rate to peak and fall again with continued addition of nitrogen, and their XPS results showed that boron and nitrogen formed B-N bonds within the diamond crystal.⁴²

Within the aforementioned literature, n-type BNDD was only seen at 773K by D. Y. Liu et al, or computationally. Research is still on-going to create an n-type BN co-doped diamond at room temperature, hence the need for this project.

1.5.1 Applications of BN co-doped diamond

Wide band gap semiconductors can be used for “electric transport and energy generation and distribution”.³ Diamond, once any electronic limitations are bypassed, with its extraordinary properties could pave the way for novel concepts, for example by providing diodes and transistors to withstand >10 kV.³ A way to bypass diamond’s limitations for use in electronics, is by doping. Previous results have shown BN to be textbook co-dopants for creating n-type diamond, as the “B increases the solubility limit of N in diamond, reduces the relaxation energy of the crystal, and improves its doping efficiency”.⁵³ The boron and nitrogen impurities can alter the already impressive properties of diamond for the better. Diamond has a large resistivity of $\geq 10^{13} \Omega\text{cm}$, excellent thermal conductivity, negative electron affinity, intrinsic carrier mobility and a large band gap of 5.4 eV.^{25, 59} A large band gap gives low background current, which is useful in detectors.¹⁸ Diamond that contains multiple nitrogen vacancy centres (>1ppm), inspires improvement in quantum sensor sensitivity, however poor N solubility in diamond impedes this in practice.^{25, 60}

CVD diamond’s wide band gap, doping capabilities and stability make it the perfect contender for electrochemical electrodes. CVD diamond films with B-doping greater than 10^{20}cm^{-3} , are conductive and have shown that they have the required conductivity for electrochemical applications.¹⁶ Miyake et al demonstrated in their 2023 paper that BN co-doped diamond exhibited higher performance as an electrode than diamond just doped with boron.¹¹ The BNDD was prepared via microwave plasma CVD, and it was found that the greater the levels of nitrogen doping, the more efficient the CO_2 reduction reaction.¹¹ Nitrogen doping promoted intermediate generation, allowing the reaction to progress through an alternative pathway.¹¹

BNDD was used in 2017 by Y. Liu et al as an efficient and stable electrode for the electrochemical reduction of CO_2 to ethanol.⁵⁸ This was due to the B and N atoms controlling the electronic structure of the diamond, which allowed the formation of “defect-induced active sites” for the reduction of CO_2 .⁵⁸ CO_2 with higher Faradic efficiency was made possible due to a “more negative H_2 evolution potential” for BNDD than for other possible electro-catalysts.⁵⁸

Other applications include aqueous capacitors made with BNDD, which were created by W. Nie et al (2022), and the BNDD was prepared by HF-CVD.⁵³ The capacitor was assembled with a “BNDD/BDD positive electrode and etched BNDD/BDD negative electrode”.⁵³ Their results showed that excellent stability was achieved with the BNDD capacitor, and that it had exceptional potential when filtering high-frequency AC signals and broadband.⁵³

J. Li et al fabricated BN co-doped diamond for use in detectors and noted that these electrodes were more effective as detectors than diamond doped solely with boron.⁵² The group used the same method of producing diamond as in this project, *via* microwave plasma CVD on p-type silicon substrates with deposition taking place over 8 hours.⁵² Gas concentrations $\text{CH}_4 / \text{H}_2 / \text{B} / \text{N}_2$ were 2/200 / 2 / 2 sccm with a temperature of 850°C and chamber pressure of 7 kPa.⁵² The solely BDD used the same conditions and concentrations, just without including nitrogen, thus providing a fair test for the evaluation of the benefit of nitrogen.⁵² The thickness after 8h of growth was $9\mu\text{m}$ and $10\mu\text{m}$ respectively for boron

doped and boron-nitrogen co-doped, whilst the morphology of both mainly showed (111) orientation.⁵²

The methodologies included in this section demonstrate the expansive range of applications of BNDD even without it having n-type properties. An expected application of n-type BNDD once produced would be in a pn-junction device for use in a battery.

1.6 Characterisation techniques

1.6.1 SEM – Scanning Electron Microscopy

SEM is used to determine grain size, morphology, and thickness of a diamond film by being able to zoom in to a micron scale. A primary electron beam is focused onto the sample surface, and the intensity translates into a surface image.²⁵ T. Guo et al analysed BN co-doped films by SEM proving them to have “similar morphology to that of polycrystalline diamond films”.³⁹ They reported that grain sizes were between 0.4-1.2 μm , and so this would be around the range I would expect to see.³⁹ Results from A. Dychalska et al showed that increased methane vapour levels in the gas mixture caused a decrease in the grain sizes in the film.³³ The methane level was kept constant within the samples grown in this project, but the effect of excess methane addition is important to understand the surface structure of diamond films.

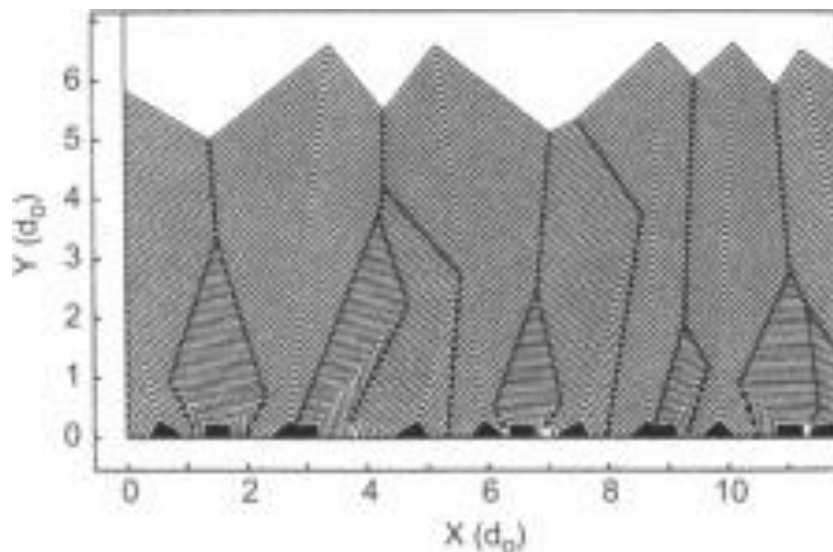


Figure 16- a diagram demonstrating the phenomenon of “columnar growth” (from K. Kobashi, 2005)⁶¹

In a SEM image you can see grain boundaries between crystals. These are important “since grain boundaries are the strongest barriers and traps for transport of electrons and holes”.⁶¹ These will therefore contribute to any strong electronic effects of the film. SEM images can show large amounts of contrast depending on what is present in the sample and its roughness. Heavier atoms appear brighter in an image as they scatter more electrons back to the detector.⁶² Conversely, lighter atoms appear darker.⁶² To this end, it would be

expected that if contrast differences were present in the SEM images taken in this project, the lighter patches would be expected to be nitrogen, and the darker boron or carbon.

As well as SEM being used for surface analysis, it can also be used for cross sectional analysis to confirm the thickness and vertical growth effects. Figure 16 reinforces the concept that diamond orientation is, on average, more random when films are thinner.⁶¹ When horizontal growth is complete (where crystals are in contact with each other), the vertical growth begins. Thus begins the columnar growth phenomenon, as specific diamond grains grow more quickly than others, and this growth competition dictates the surface orientation of the diamond layer.⁶¹ This is what can be seen in figure 16. It has been found that as the film thickness increases, the tendency for diamond grains to be aligned along the (110) direction increases, and this is also documented as a characteristic orientation for diamond crystals grown by CVD.⁶¹ Doped diamond, however, may have different orientations due to the dopant impurities present in the diamond lattice.

1.6.2 Raman Spectroscopy

Raman spectroscopy is a non-invasive, infra-red technique alongside a polarizability shift so that diamond (with a lack of changeable dipole) can become visible in the IR region.²⁵ Raman can be used to evaluate sp^2 vs sp^3 bonding, strain, and crystalline structure.¹⁶ Carbon has multiple bonding configurations: diamond with sp^3 fourfold bonding and graphite with sp^2 threefold.¹⁶

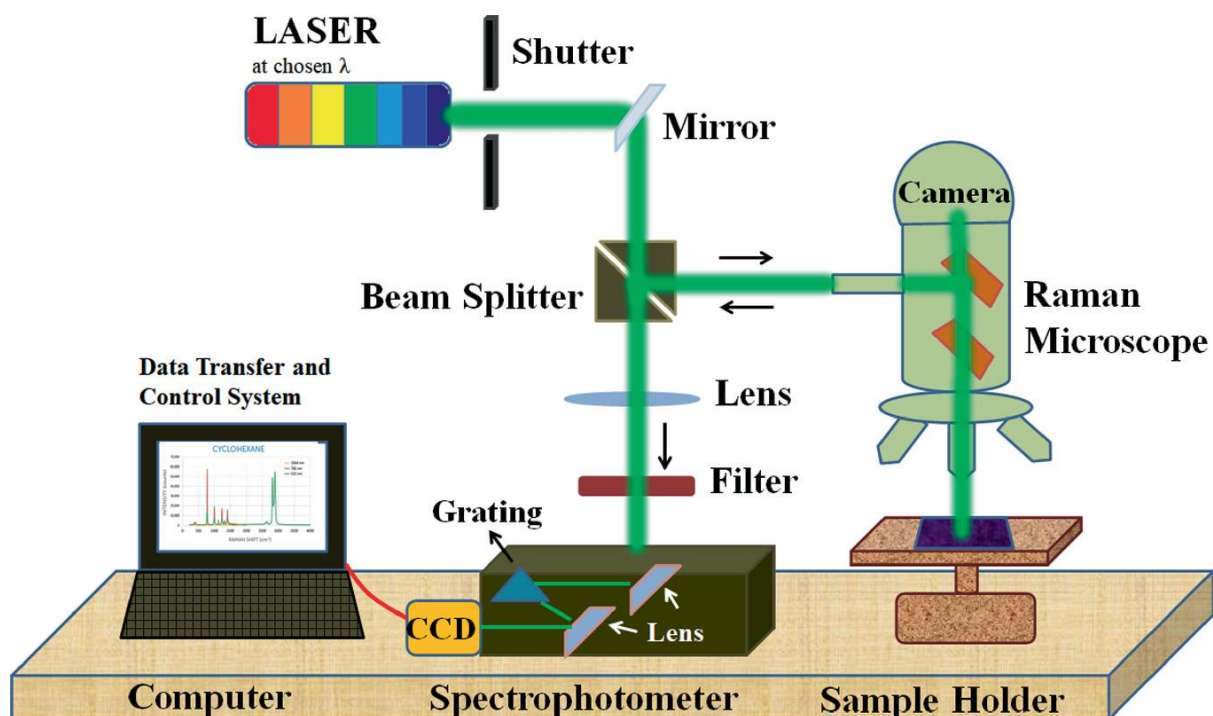


Figure 17 – A schematic of a Raman spectrometer, (from D. K. Pandey et al, 2021)⁶³

The method of Raman spectroscopy utilising a laser light source as shown in figure 17, and is based upon the “Raman effect”, the secondary scattering of radiation, discovered by Sir Chandrasekhara Raman and published in 1928.⁶³ The “inelastic scattering of light by the

object” is detected and read by the computer, and this data is displayed as peaks.⁶³ The spectral peaks can be used to determine the bonding in a material by comparing the location of peaks to those in literature.

The typical Raman peak for diamond would be expected to be $\sim 1332 \text{ cm}^{-1}$, also with a broad peak at $\sim 1580 \text{ cm}^{-1}$ which results from bond stretching of sp^2 atoms, known as the “G band”.^{18, 39} Raman spectra can also show non-diamond carbons produced by CVD, including graphite, and amorphous sp^2 carbon.³³ Generally, CVD diamond films are made up of small microcrystal diamonds which are surrounded by amorphous carbon or graphite.³³ This means that a CVD diamond film will contain a variety of Raman shifts compared to pure diamond. These carbon forms and their corresponding shifts are shown in table 2.

The difference between Raman spectra of samples with varying amounts of nitrogen is minute. Figure 18 is taken from the work of Z. W. Wang et al and shows the Raman spectra peaks of various BNDD.⁴² When looking at Raman spectra from work in this project I would also expect to have very consistent peaks like these (changes only within 2dp).

Table 2- Position of Raman spectra peaks for carbon and their interpretations (adapted from the work of A. Dychalska et al 2015)³³

Raman shift (cm^{-1})	Interpretation
1580	Monocrystalline graphite
1546	Disordered graphite
1500-1600	Amorphous carbon sp^2 (G-band)
1430-1470	Trans-polyacetylene in grain boundaries
1345	Amorphous carbon sp^2 (D-band)
1332	Diamond band
1220	Disordered diamond
1150-1237	Nanodiamond
1100-1150	Trans-polyacetylene segments at grain boundaries

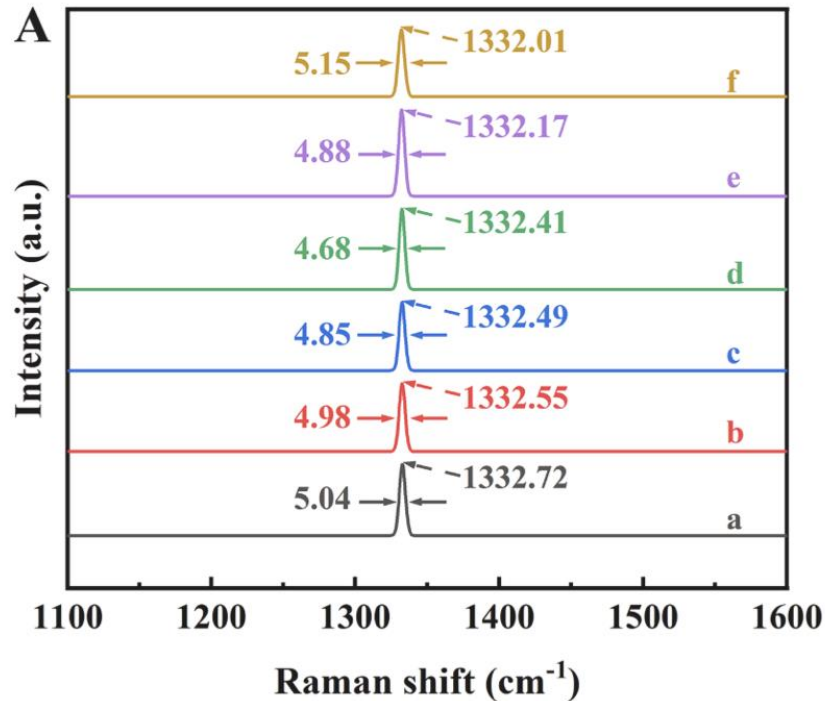


Figure 18- Raman spectra of samples prepared with 0-0.5% h-BN (from the work of Z. W. Wang et al, 2023)⁴²

1.6.3 XPS – X-ray Photoelectron Spectroscopy

A non-destructive technique used to characterise the chemical bonding of elements and molecular structure of the sample.^{42, 64} It is a surface level technique and requires the film thickness to be small enough to ensure that photoelectrons can escape for analysis.⁶⁵ XPS can be explained by the photoelectric effect, incident photons from the x-ray excite surface electrons and their kinetic energy is measured.⁶⁶

Oxygen impurities are likely to be visible in non-terminated diamond films due to post-growth exposure to the oxygen in the air. Oxygen and carbon atoms may be attached by either single or double bonds, or oxygen may be a bridging atom between two adjacent carbon atoms.⁶⁵ Looking at the C 1s spectrum can help classify the structure of the diamond surface.⁶⁵ An example C 1s centred XPS spectra is shown for a pure diamond sample in figure 19a, whilst a table of how different C bonds and states are represented in XPS spectra is shown in table 3. The table shows some of the key carbon states expected in this project. The values are very similar to each other and in the case of sp^3 C and C-C, the exact same. This means care must be taken when determining XPS peaks.

The use of XPS to determine bonding within a sample is demonstrated in figure 19b. The N 1s spectra of a BNDD film shown demonstrates how the nitrogen dopant is well incorporated into the lattice from the N-C bond and demonstrates how BN clusters were made from the N-B bond. The N-O bond is expected from a sample that has been exposure to the oxygen in the air. These peaks would be expected from the samples made in this project.

Table 3 - Binding energies of common C 1s compounds (adapted from Watts and Wolstenholme, 2020)⁶⁷

Chemical state	C 1s Binding energy (eV)
sp ² carbon	284.4
sp ³ carbon	284.8
C-C	284.8
C-O	286
C=O	288
O=C-O	288.5

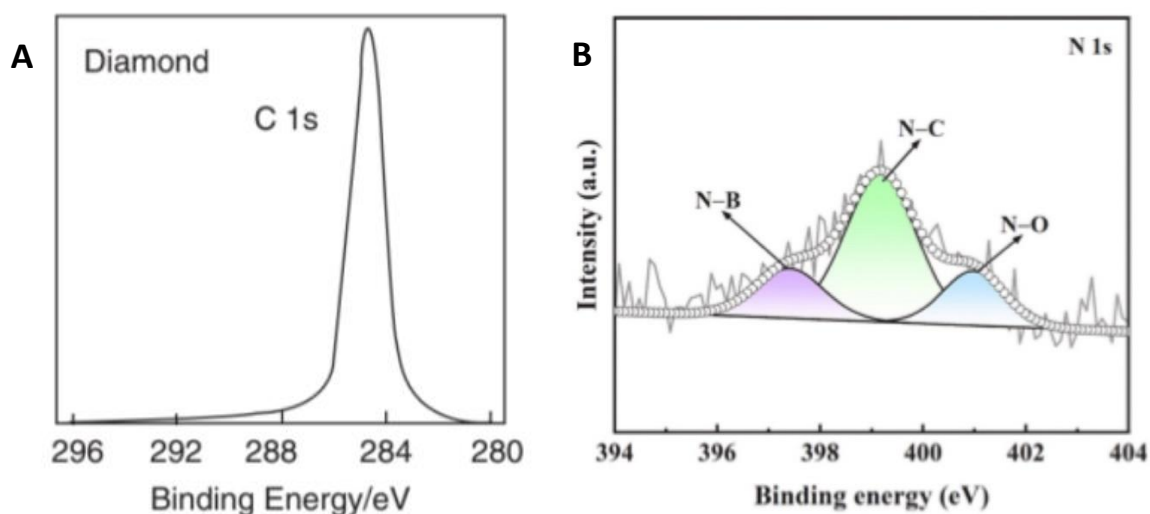


Figure 19 – a) Demonstration of the expected results from a C 1s atom analysis by XPS of a pure diamond sample (From Watts and Wolstenholme, 2020)⁶⁷ b) representation of expected N 1s peaks (from the work of Z. Wang et al, 2023)⁶⁴

1.6.4 UPS – Ultra-violet Photoelectron Spectroscopy

The UPS technique is very similar to that of XPS but ultraviolet photoelectrons are directed at the sample, and these high energy photons have the capability to probe valence band electrons, so different information is received.^{66, 68} This technique gives an insight into the distribution of energy levels in the sample, including the valence band maximum and work function.

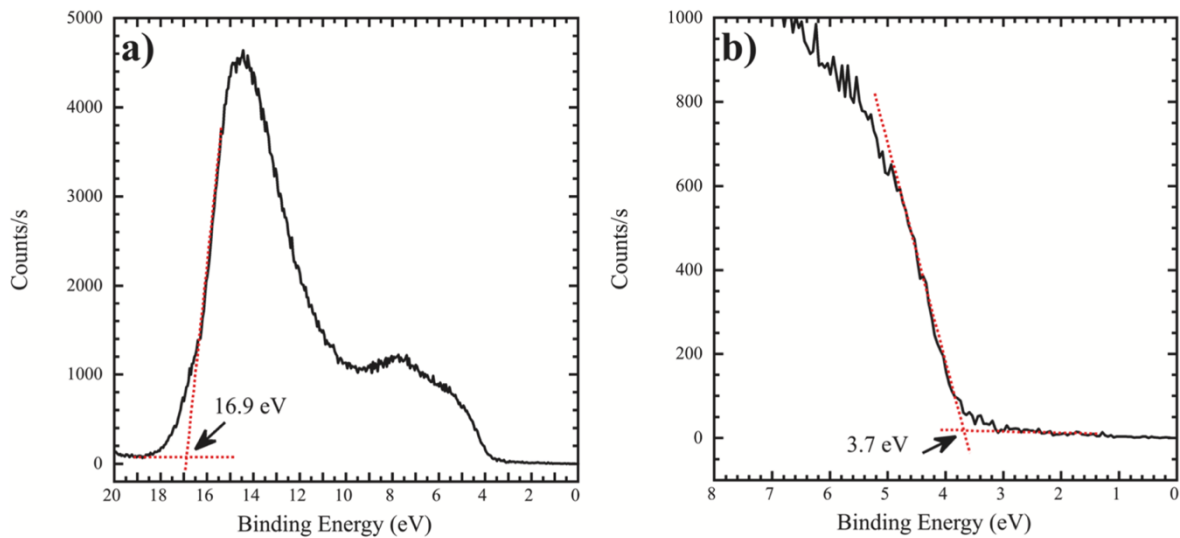


Figure 20- Diagrams indicating the process of analysing UPS spectra, a) shows the determination of the high-energy cut-off for use in determining the WF, b) shows the VBM. (from the work of J. E. Whitten, 2023)⁶⁸

The spectra in figure 20 indicate the process of determining values from UPS. Ya) shows the high-energy cut-off also known as the SECO (secondary electron cut-off), and the work function can be found as the difference between this and the UV source energy, whilst Yb) shows the VBM.⁶⁸

1.6.5 PEEM – Photoemission Electron Microscopy

A technique utilising the acceleration of photons, by an extraction lens, from the excitation of the incident beam (in this project this is from UV photons, however X-rays are also used in literature).⁶⁹ A contrast aperture is used to “limit the angular acceptance of the photoelectrons”, and the electrons pass through a series of lenses to reach the area detector where an image is formed.⁷⁰ A diagram outlining the PEEM technique is included in figure 21.

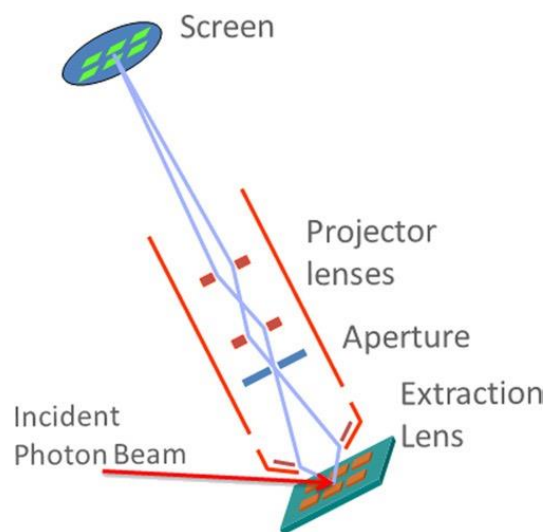


Figure 21 - A schematic of the PEEM technique of analysis (from X. M. Cheng et al ⁶⁹)

1.6.6 SIMS – Secondary Ion Mass Spectrometry

Another characterisation technique is SIMS, which can be used to measure the specific composition of B and N atoms in the diamond film. A primary heavy ion beam causes a secondary output of electrons, radicals, and ions for analysis.²⁵ This technique is somewhat destructive, leaving behind a hole in the sample, so may need to be carried out after other analysis is complete. SIMS allows analysis throughout the sample, comparing the elemental composition with a depth profile. This makes it an especially useful technique since so many of the other analysis techniques listed are only surface level.

1.6.7 Sheet resistance measurements

Sheet resistance can be calculated from current/voltage measurements by plotting an I/V graph and determining the resistivity from the gradient. The resistivity of the film can then be used to get a specific sheet resistance value in Ω/square . This can simply be calculated by dividing resistance by the thickness of the sample, but it can also be calculated from known parameters without the thickness data being necessary. This equation is listed in section 3.3.2 as it was utilised in this project.

1.6.8 Hall measurements

Discovered in 1879 by Hall, Hall effect measurements give the carrier concentration and type, giving mobility values in combination with the measured resistivity.^{71, 72} Carrier mobility is “the most important property for any electronic device” as it shows the speed at which electrons or holes are able to move through a material.⁷³ Hall measurements are also able to show whether n-type conductivity has been achieved or not, the former indicated by a negative Hall coefficient.³² When a current carrier is exposed to a magnetic field, perpendicular to the current direction, the Hall effect occurs.⁷¹ If both the current and the magnetic field are flowing in the x and y directions, a potential gradient will appear in the z direction.⁷¹ The “particle nature of conduction” can explain the basis of the Hall effect.⁷¹ The Hall constant can be shown mathematically in equation 2.⁷¹

$$\text{Grad } V_H = - RiH \quad (2)$$

Where $\text{Grad } V_H$ is the transverse potential gradient, R the Hall constant, i is the current density, and H the applied magnetic field.⁷¹

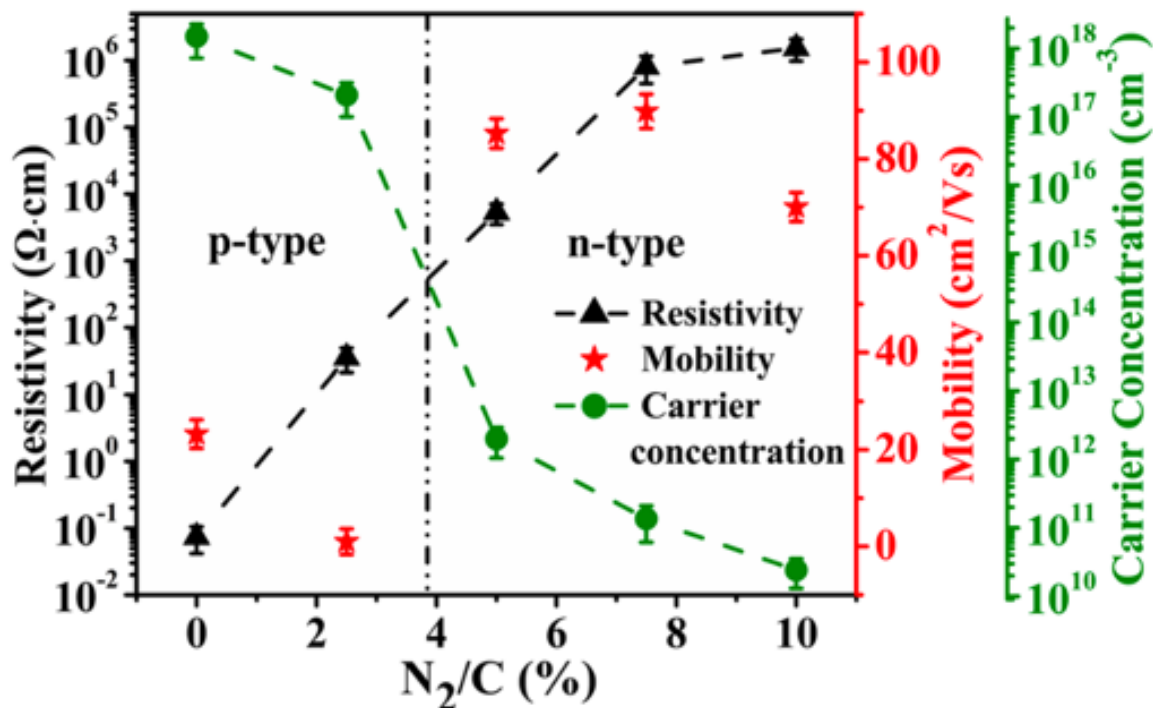


Figure 22- The resistivity, mobility and carrier concentration at 773K of BDD and BNDD (from the work of D. Y. Liu et al, 2021)⁵⁷

As is seen in figure 22, as the N₂/C ratio increases, so does the resistivity, whilst the carrier concentration decreases. Some of the BNDD films created here do exhibit n-type conductivity at 773K. The mobility values increase once the materials exhibit n-type properties. It is important to note that Hall measurements taken as part of the research for this thesis were at room temperature, and so cannot be directly comparable to those in figure 22. Published results state that the Hall effect measurements of BDD synthesised by CVD show the maximum mobility to reach 1840 cm² / V s at 290 K.³²

1.7 An alternative dopant gas: N₂O

Traditionally the nitrogen doping of CVD diamond came from N₂, but recent research suggests an alternative nitrogen source: N₂O. It has been found that utilising N₂O over N₂ can limit macroscopic defects formed and improve the nitrogen vacancy centres' stability.⁶⁰ It creates low donor concentration and therefore improves BNDD electrical performance due to increased hole mobility.⁷⁴ The use of N₂O gas is therefore something that would be beneficial to explore in creating n-type BN doped diamond.

Ngambou et al (2022) used 100ppm concentration of N₂O in the gas phase, total gas flow was 500 sccm, 200 mbar pressure and 3000 W power.⁶⁰ Temperature was varied between 850°C to 1000°C, and methane concentration between 3% and 7%.⁶⁰ A post growth treatment of electron irradiation at 2.3 MeV at room temperature was completed to improve nitrogen vacancy density.⁶⁰ It was found that nitrogen vacancy doping was higher for the sample grown at lower temperature (850°C) and lower methane concentration (<4%).⁶⁰ Their research showed that N₂ gas has a low doping efficiency and can lead to

growth defects at higher concentrations, compared to N_2O which has good optical properties and obtains high NV densities.⁶⁰ N_2O has lower bond dissociation energy (N-O, 197.6 kJ/mol) vs (O=O, 490.4 kJ/mol) which means O radicals are created more easily in the plasma, and crystal quality is improved.⁶⁰

Work by D-Y Liu et al (2023) has also been completed utilising N_2O . Their results show that the oxygen in N_2O has “a strong inhibitory effect on formation of NV centres” and that this effect strengthens as the N_2O concentration increases.⁷⁴ Their method was MPCVD with CH_4 at 20 sccm and H_2 at 500 sccm, with the B_2/C ratio fixed at 50 ppm.⁷⁴ The N_2O/C ratio is varied as 0%, 2.5%, 5.0%, 7.5% and 10% whilst pressure is fixed at 135 torr, power 3.8 kW and temperature 800-850°C.⁷⁴ They found that growth rate decreased as the N_2O/C ratio increased, showing the typical effect of nitrogen improving growth rate to be non-existent here.⁷⁴ The group believe the etching and inhibiting effect of oxygen to outweigh nitrogen’s growth effect, and their optimum crystal quality was at a 7.5% N_2O/C ratio.⁷⁴

The Ngambou group showed that N_2O increased the presence of NV, whereas the Liu group found N_2O to inhibit the presence of NV. It would therefore be interesting for future work to include studies into the effects of N_2O as an n-type dopant in diamond.

2 Project aims

The overriding motivation behind this research project is for the creation of an n-type diamond that functions at room temperature. This would allow the advancement of thin film diamond electronic applications, through the creation of a diamond-based pn-junction device. Through computational studies, it is understood that BN clusters within the diamond lattice can realise this n-type conductivity, thus presenting the challenge of its creation in practice.

This project focuses on understanding the effects that boron and nitrogen doping individually have on the properties of BNDD. The findings from this project aim to assist in finding n-type diamond, through further understanding of how each dopant influences the diamond surface, the band structure and the conductivity.

Following on from E. Requena's MSci project, which didn't achieve n-type diamond due to the conclusion that BN_2 clusters weren't formed, this project gave more consideration to the gas concentrations used by the successful D.Y. Liu group.^{57, 75} A greater breadth of nitrogen to carbon ratios, and a lower boron concentration were used, with the hopes of ensuring that N-rich BN clusters were made.

Two sets of BNDD growths were completed during this project, with one set varying the nitrogen concentration and pinning the diborane concentration, and *vice versa* for the other set. The samples were grown using MP CVD, and all other reaction conditions were constant. This allowed trends to be drawn from the effects of increasing each of the dopant atoms.

Samples were analysed by SEM, for surface morphology and cross-sectional analysis. Sheet resistance measurements were taken using four-point probe apparatus, and Hall measurements determined the carrier concentration and mobility of the samples. XPS, UPS and PEEM were used for further understanding of the bonding and the band structure of the samples.

3 Experimental

3.1 Preparation of substrate

P-type silicon wafers with resistivity 800-1200 Ω cm and thickness 675 ± 15 μ m, were cut to 10x10 mm by a laser cutter. Then using a natural micron diamond powder, their surfaces were manually abraded to ensure better nucleation for diamond growth. The substrate surface was then cleaned with isopropanol to remove any residual powder.

3.2 Microwave Reactor

The substrate was loaded into a microwave plasma reactor, centred on a Mo disk, on top of a 0.5mm Mo separating wire. Emissivity was set to 0.19 ϵ in line with the guideline value for silicon. Plasma was struck with just hydrogen gas, 15 torr pressure and ~ 0.5 kW power. The microwave power was brought up to 1.1 kW and the pressure to 100 torr, and simultaneously the other 3 gases were switched on. It was ensured that the reflective power inside the reactor was at 0.00 kW by utilising the tuning dials.

Two sets of reactions were carried out. One where the concentration of nitrogen was varied, and everything else kept constant, and one where the concentration of diborane was the only component varied.

3.2.1 Nitrogen variation runs

The volumes of B_2H_6 , H_2 , CH_4 were kept constant whilst the volume of N_2 was varied as a ratio to the CH_4 concentration, as shown in table 4. Each sample growth was run for 3 hrs, and the temperature range was $\sim 900^\circ C$. The reactor is only accurate with respect to gas concentrations to 1dp, so N_2 values were rounded up or down to 1dp.

Table 4 – the gas concentrations for experiments varying the nitrogen to methane ratio

N2/C	CH4 (sccm)	H2 (sccm)	B2H6 (sccm)	N2 (sccm)
0%	25	500	0.5	0
2%	25	500	0.5	0.5
2.50%	25	500	0.5	0.625
3%	25	500	0.5	0.75
3.50%	25	500	0.5	0.875
4%	25	500	0.5	1
4.50%	25	500	0.5	1.125
5%	25	500	0.5	1.25
7.50%	25	500	0.5	1.875

3.2.2 Boron variation runs

Further MPCVD growths where CH₄, N₂, H₂ volumes were kept constant and the B₂H₆ concentrations were varied were carried out. The growth conditions were also consistent with those used for the nitrogen variation growths: 3 h growth time and ~900°C substrate temperature. The complete set of gas concentrations used is listed in table 5. The 2% B₂/C sample is the same as the 4.5% N₂/C sample listed above in table 4, so that the two datasets can be more easily compared. This sample was chosen due to its low resistivity and large amount of single crystal diamonds present on the sample surface, and the diborane concentrations were varied either side. The diborane concentration was never raised higher than the nitrogen, since all the literature agrees upon boron-rich doping being detrimental to n-type conductivity.

Table 5- *the gas concentrations for experiments varying the diborane to methane ratio*

B ₂ /C	CH ₄ (sccm)	H ₂ (sccm)	N ₂ (sccm)	B ₂ H ₆ (sccm)
1%	25	500	1.1	0.25
1.5%	25	500	1.1	0.375
2%	25	500	1.1	0.5
2.5%	25	500	1.1	0.625
3%	25	500	1.1	0.75
4.5%	25	500	1.1	1.1

NB: due to limitations with the function of the microwave reactor, the 3% and 4.5% samples were not carried out. They are included in this table, however, for completion and as a guide when discussing expected trends within this dataset.

3.3 Analysis

3.3.1 Raman

Measurements were taken using a Renishaw 2000 laser Raman spectrometer, using a 514 nm green laser. When measurements were taken the spectral range centre was set to 1332 cm⁻¹, and 15 accumulations were taken with a 10s exposure time at 60% laser power. Raman measurements were taken at RTP in air.

3.3.2 Resistivity

Both a 2-point probe and a 4-point probe were used to take I/V measurements and determine resistivity.

Two-point probe

The 2-point probe utilised a Keithley source current meter. The readings were taken at RTP, and probes were placed on the films by hand ~ 1mm from the edge of the film. An I/V

reading was taken to determine the resistivity in Ωcm^{-2} . This is not a very reliable source of analysis due to the large amount of human error present. The probes had to be placed by hand and this means natural inconsistencies of the distance between probes. As such, the results of these measurements are in the appendix as they don't contribute to the trend achieved by the 4-point probe.

Four-point probe

4-point probe measurements were taken using a Keithley 2400 Sourcemeter (Keithley Instruments, USA) at RTP. The system had 0.012% basic accuracy with 5 ½ digit accuracy. Measurement settings were as follows: initial current 0.01 A, 4 steps and a current step size of 0.001A. The target voltage was 0.003 V, and the compliance 20 V. Samples were loaded so that the 4 probes lay across the diagonal of the thin film square, as shown in figure 23, avoiding the very corners to ensure diamond contact. 2 readings were taken on one diagonal, and 2 taken on the opposite diagonal and a mean was found of the 4 readings. Generally, these readings had very little variation, and therefore seemed reliable. These I/V readings were converted into V/I and then put into equation 3 to find the sheet resistance, of which the units are ohms per square. The sheet resistance can also be found by dividing the resistance by the thickness of the sample.

$$R_{\square} = \frac{\rho}{t} = \frac{\pi}{\ln(2)} \frac{V}{I} f_1 f_2 \quad (3)$$

The geometric factors f_1 and f_2 incorporated the thickness and width of the sample into the sheet resistance value calculated. f_1 is equal to 1 for samples where the thickness was smaller than the distance between the probes (3.3mm), which was the case for these samples. f_2 referenced the length and widths of the samples, and it is a known value based upon the length of the sample compared to the spacings of the probes.

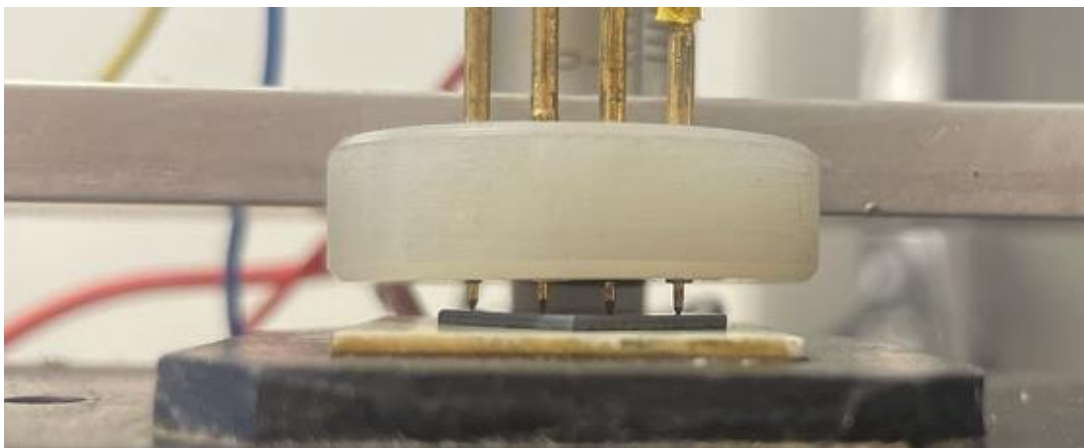


Figure 23 – A photograph of one of the samples set up in the 4-point probe apparatus

3.3.3 Hall measurements

Measurements were taken using Ecopia, Hall Effect Measurement System (HMS-5000). Indium contacts were welded onto samples in the corners, and the probes were positioned on top of them as shown in figure 24. It is important to note that these measurements will have a lot of inconsistencies as they assume a perfectly symmetrical, homogeneous sample at constant temperature.⁷² However, these samples were not perfectly symmetrical as the growth on the edges was different to the centre, there are many grain boundaries, and crystals of different sizes amongst the film, as shown by the SEM analysis. The temperature was “room temperature” which was inconsistent as the temperature was not controlled by the measurement system and instead by variables, such as the heating/windows/doors, in the analysis room. Contact resistance could also have been present due to the indium contacts.



Figure 24- A photograph of a sample with indium contacts loaded into the Hall effect measurement system

3.3.4 SEM

The scanning electron microscope is located in the Bristol Chemical Imaging Facility. The system is JSM-IT300 from JEOL, Japan. All images were taken at an acceleration voltage of 15 kV and a working distance of 10mm to detect secondary and backscattered electrons. Images were taken at various levels of magnification, consistently across the different samples. The surface of the films was inspected for analysis into the surface morphology. For cross-sectional analysis the samples were cleanly broken in half and mounted on 70°

angle mount. This angle means that when working out the film thickness, trigonometry is used to mitigate the difference in visible thickness caused by a non-perpendicular angle of incidence. The equation used is written in equation 4.

$$\sin(70^\circ) = \frac{\text{Visible thickness}}{\text{Actual thickness}} \quad (4)$$

3.3.5 XPS

Specific samples were selected for XPS analysis and they were mounted on molybdenum or stainless-steel sample holders with no adhesive. XPS took place in a ScientaOmicron Argus analyser with monochromatic Al K α X-ray source, of 1486.7eV. The system operates under ultra-high vacuum (UHV), with XPS chamber base pressure of 2×10^{-11} mBar. Samples were annealed at 300°C for 1 hour in $\sim 1 \times 10^{-8}$ mBar pressure, before undergoing XPS. Analysis was carried out with aperture A4, pass energy at 50 eV for survey scans and 20 eV for individual atom high resolution scans, with the sample centred.

A survey run was taken first of the sample, and this allows us to see what is present, as the peaks at specific binding energies correspond to a specific atom. We can then scan a specific area which gives us more information about the exact type of bonding present in that atom. The data is returned as kinetic energy, and this is converted to binding energy by subtracting the KE from the excitation energy, of 1486.7eV from the x-ray source.

3.3.6 UPS and PEEM

After XPS analysis, samples stayed under UHV and were transferred into another analysis chamber for UPS and PEEM analysis. The measurements were carried out in Focus/ScientaOmicron NanoESCA II, with monochromatic He I 21.2 eV and base chamber pressure 1×10^{-11} mBar. The field of view was 120 μm , the pass energy 50 eV and the slit width 0.5 mm. UPS can be used to determine the valence band maximum and the high-energy cut-off of a sample. The difference between the latter and the He I source energy (21.2 eV), can be used to find the work function.

When work function PEEM measurements were taken, a contrast aperture was inserted into the back focal plane to improve the lateral resolution. PEEM data can be plotted using MATLAB to give a heatmap diagram of the difference in work function across the sample surface.

4 Results & discussion

4.1 Raman spectroscopy

4.1.1 Nitrogen variation runs

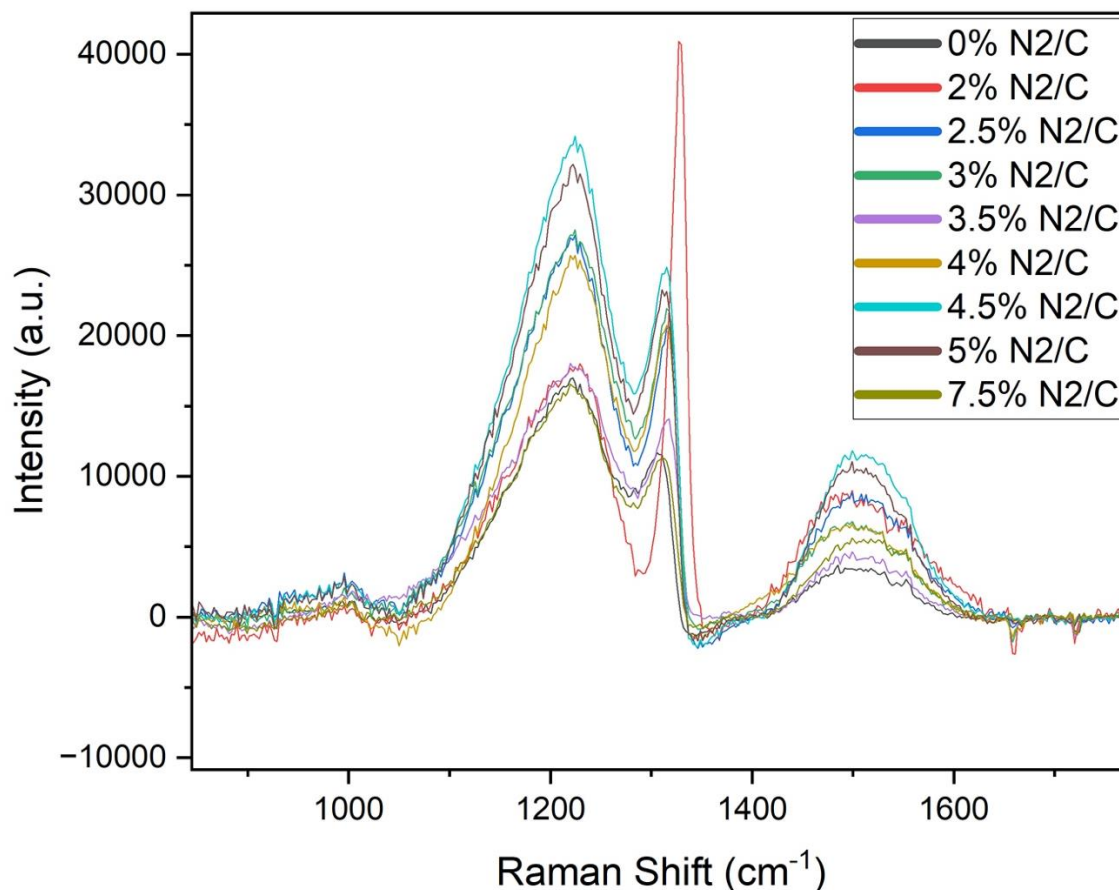


Figure 25- Raman shift graph of all nitrogen variation runs. The baseline has been subtracted so that it lays flat for easier viewing. The y-axis units are arbitrary.

The Raman spectra from the N₂/C 0-7.5% growths produced a distinctive boron peak around 1200, due to all samples being B-doped, and this is shown in figure 25. The size of the boron peak had no correlation to the amount of boron present within the samples. A characteristic diamond band peak was shown near to 1332 (between 1320-1332), and the broad peak around 1500 was found to be the G band: amorphous sp² carbon. The diamond peaks for all the samples, bar the 2% N₂/C sample, indicated diamond peaks with lower Raman shifts. This could have been due to the increased doping causing distortion in the sp³ carbon, diamond lattice.

The 2% N₂/C sample showed the cleanest diamond peak at 1332 cm⁻¹. Since the purely boron doped sample, 0% N₂/C, showed a shifted diamond peak, it can be said that the inclusion of N atoms, at this dopant concentration, were conducive to the continuation of the sp³ carbon lattice in BNDD. This change in the position of the diamond peak could corroborate that nitrogen was present within the diamond lattice, as the only change in

composition between this sample and the 0% sample was the inclusion of nitrogen. As the nitrogen concentration increased above this to 2.5% N₂/C, the diamond peak yet again shifted which validated that the now higher nitrogen doping caused further distortion within the diamond lattice. The clean diamond peak at 2% did not determine if the electronic properties of the 2% sample were the most desirable, and so further analysis was required to explore this.

4.1.2 Boron variation runs

The same main peaks are shown in figure 26a as in figure 25, amorphous sp² carbon, the boron peak and the characteristic diamond peak again shifted slightly lower due to the inclusion of dopant impurities into the diamond lattice. It can be seen upon closer inspection that the diamond peak ~1332 cm⁻¹, had a gradually lower shift as the concentration of boron doping increased, confirming that the dopant incorporation had influenced this. This portion of the graph is expanded for ease of looking and is shown in figure 26b.

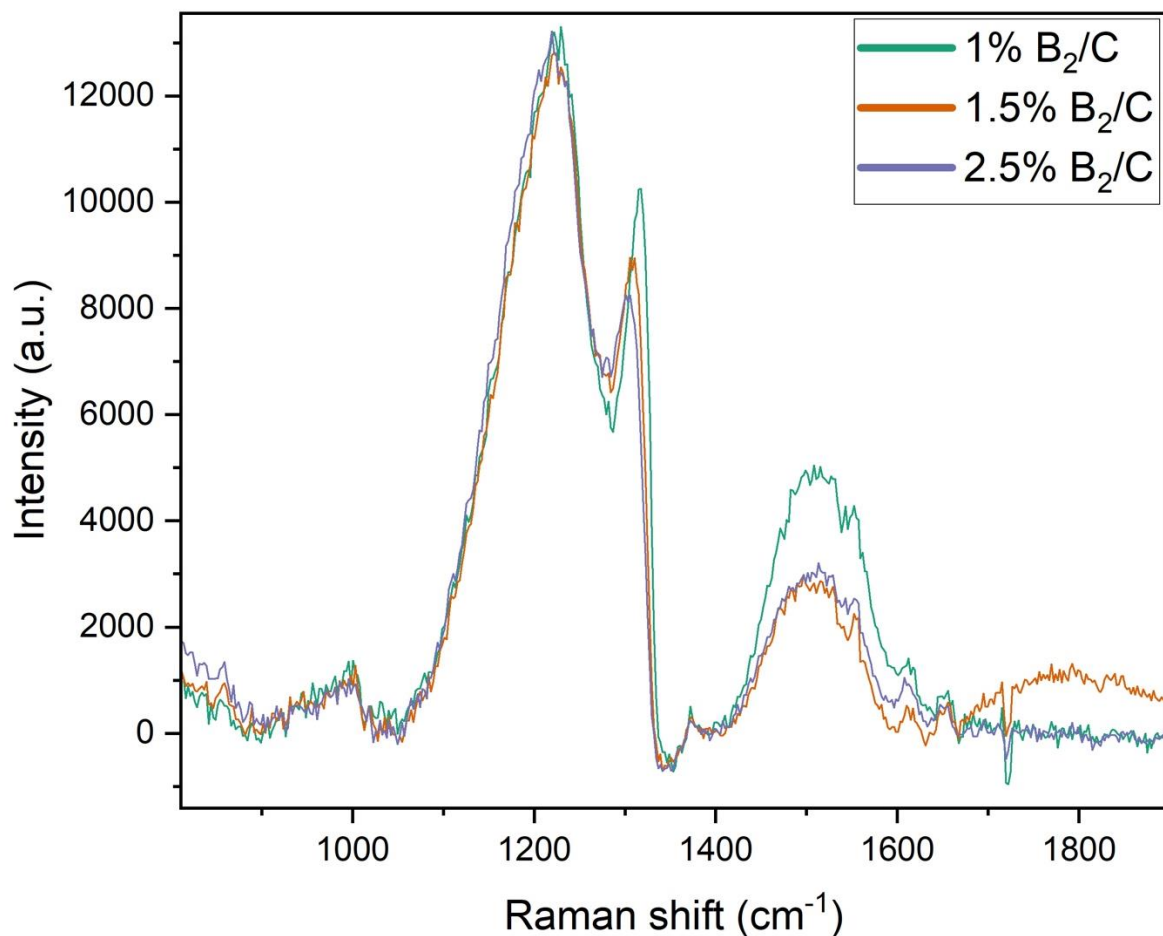


Figure 26a- Raman shift graph of boron variation runs. The baseline has been subtracted so that it lays flat for easier viewing. The y-axis units are arbitrary.

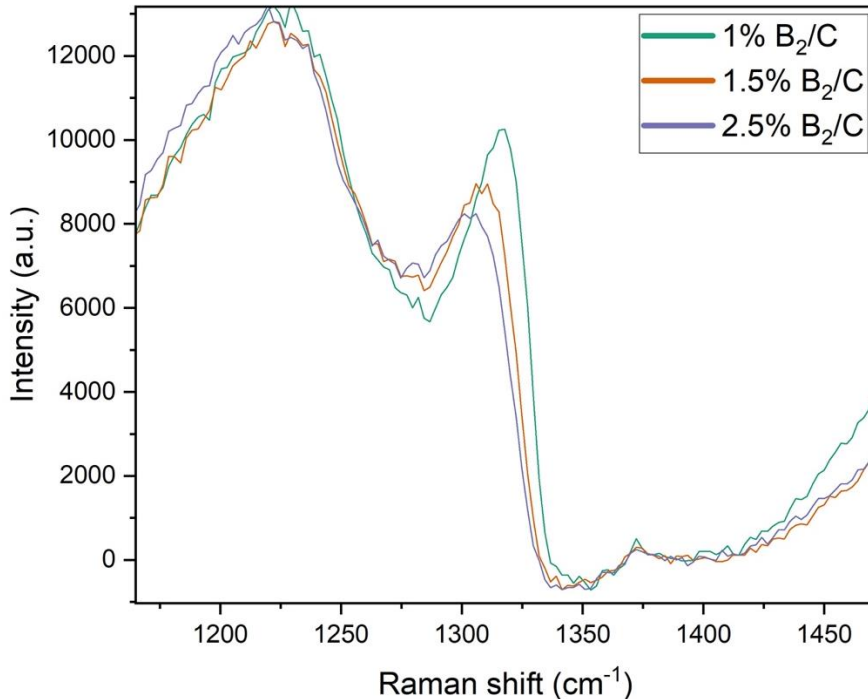


Figure 26b – Zoomed in portion of the boron variation Raman spectra centred around the diamond peak to demonstrate how increased dopant incorporation caused a shift

Since pure single crystal diamond gives a smooth bump-free Raman spectra with a single peak at 1332 cm^{-1} , it may be deduced that the bumpiness present in these spectra is also an effect of the doping. The dopant atoms cause distortion within the diamond lattice, and this translates onto the spectra.

The spectra of all samples confirmed that diamond was made, and that boron was present within the diamond lattice, as well as graphitic regions due to the dopant incorporation. These results provide an initial understanding of the composition of the diamond made, confirming both boron and nitrogen's presence.

4.2 SEM

4.2.1 Surface morphology

Nitrogen variation runs

Figure 27 shows images taken at a magnification of x5,000 and an acceleration voltage of 15 kV, with the images centred around a single crystal diamond in each of the films. BNDD with 0% nitrogen, a purely boron doped film, showed larger crystals surrounding the large central one, compared to its nitrogen doped counterparts. The 2, 2.5 and 3.5% samples all showed relatively similarly sized single crystals, and it was not until BNDD 7, 4.5% N₂/C, that the crystal showed a large increase, and a greater density of single crystal diamonds. BNDD 9 indicated a change in the shape of the diamond, and this was when the nitrogen concentration was at its very highest.

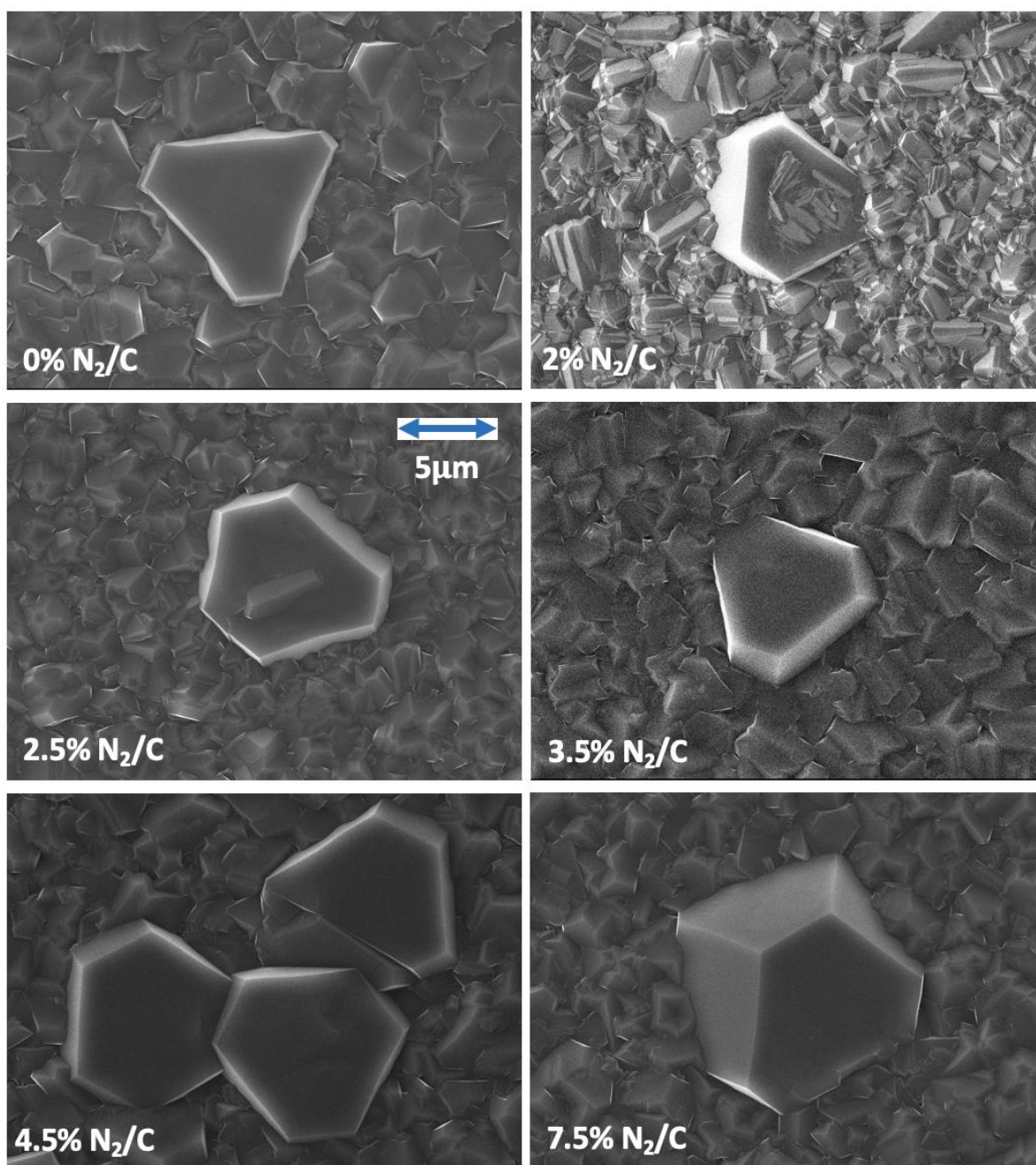


Figure 27- SEM images of nitrogen variation growths at x5,000 magnification

The large microcrystal diamonds centred in these images measure between 6-8 µm in width. The smaller crystal grains were larger in the purely boron doped sample (0% N₂/C) at ~2 µm, and their size decreased down to ~1.5 µm for the 7.5% N₂/C sample. This was in line with the work of J. Li et al who also found introducing nitrogen to decrease grain sizes.⁵² From this, it may be concluded that the raised level of nitrogen doping, decreased the size of the bulk grains in the diamond layer. The large central crystals in the nitrogen doped samples (2-7.5% N₂/C) showed a difference in their surface morphologies. In line with the literature, as the level of nitrogen increased, the surface of the films became rougher, as nitrogen had the effect of increasing the amount of sp² carbon present.³⁹⁻⁴¹ The SEM images showed that the 7.5% N₂/C sample had a different crystal orientation. The face of the diamond microcrystal is tilted, whereas in the other growths, it is face up. This agreed with

the literature that large amounts of nitrogen doping affected the crystallinity which caused crystals to become less well-orientated.⁶⁴ Figure 28 showed a crystal structure that was much closer to the cubic (100) shape than the other cubo-octahedron shaped crystals. These crystal shapes are referenced in figure 9. The high level of nitrogen doping had the effect of making crystals more cubically orientated. It is well documented that increased nitrogen increases the tendency for these grains to have (110) direction, so this may explain the change, however whether this sample had (110) orientation, would have required x-ray diffraction confirmation.⁶¹

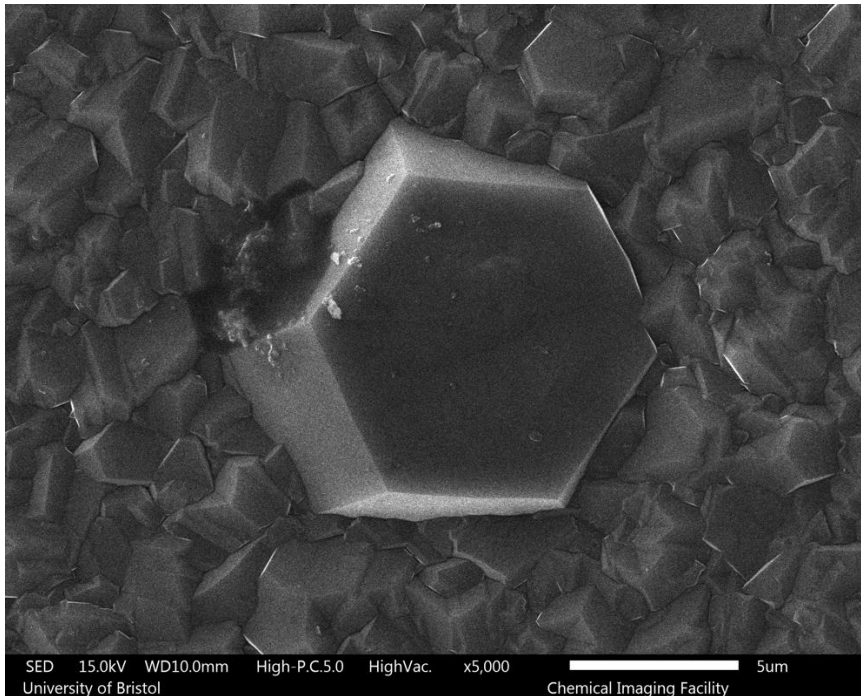


Figure 28- SEM image showing the 7.5% N₂/C sample with a different crystal face shape to other samples.

The 2% N₂/C sample in figure 27 showed a very different image to the rest. There was a distinctive “checkerboard effect” where the bulk grain crystals had very distinctive light and dark patches. This effect is due to different atomic weights of composite elements, which caused their backscattering electrons to appear differently. Nitrogen, as the heaviest atom present in the films, was the most likely cause of the brighter patches in the 2% sample. This contrast of light and dark in the film can be explained as better integration of the dopants into the diamond lattice. In this sample, the diborane and nitrogen gas concentrations were equal (excluding any potential residual boron inside the reactor). The results feasibly proved this to be a more optimal level of doping to maintain crystallinity and equal dispersion of dopant elements, as when the nitrogen levels were too high the morphology was adversely affected.

Boron variation runs

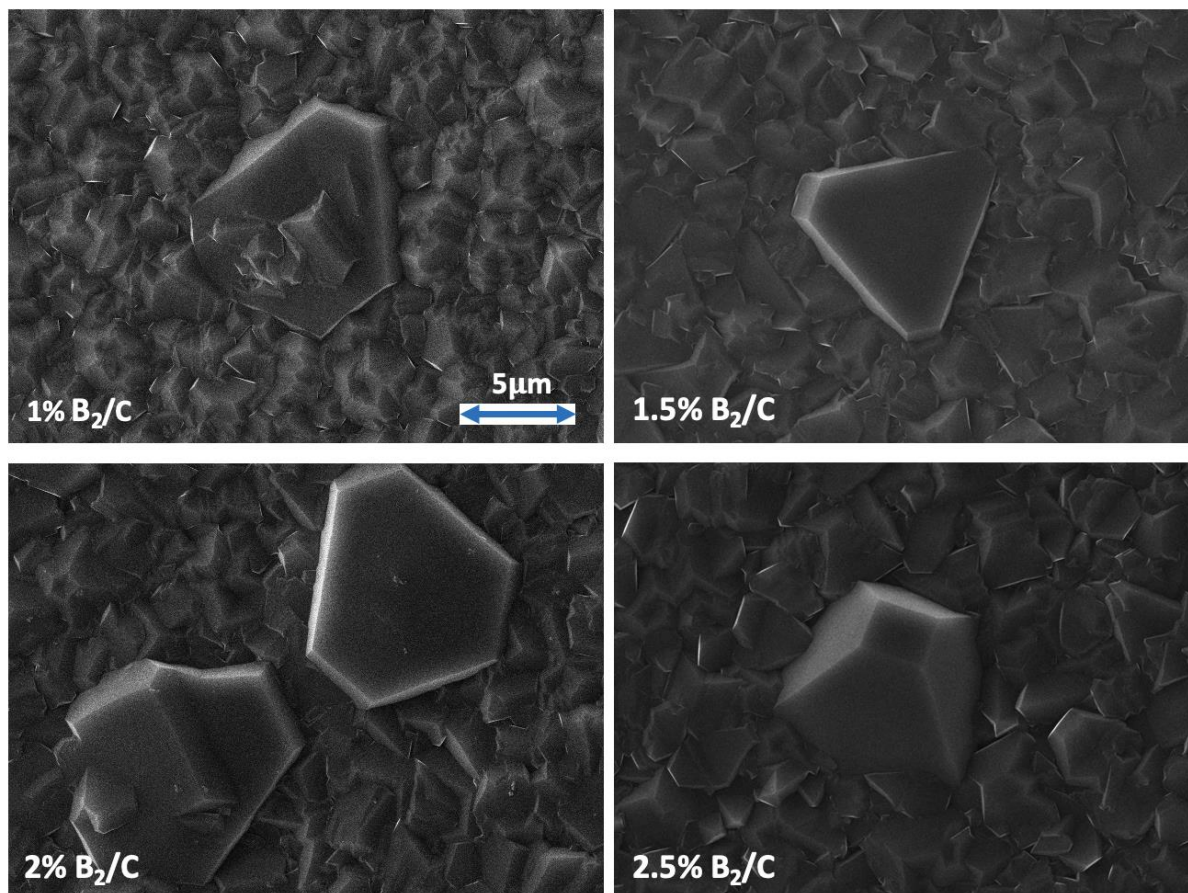


Figure 29- SEM surface images of diamond films grown with increasing levels of boron doping at x5,000 magnification

As the concentration of diborane increased gradually, from 1% B₂/C to 2.5%, the surface morphology changed considerably. Immediately obvious from the SEM images in figure 29, was the change in the size of the bulk crystals, as they became much larger with increasing boron dopant levels, from ~2 μm to ~3 μm. This was in direct contrast to the trend from increasing nitrogen, as N had the effect of decreasing grain size. The single nanocrystal diamonds in these films were also a little larger than for the nitrogen variation growths, ranging from ~7 μm for 1% B₂/C to ~8 μm for 2.5% B₂/C.

Again, with these growths, the most heavily doped sample indicated a change in crystal orientation, as the large nanocrystal diamond in the 2.5% sample was angled differently to the other samples. This begged the question of what the film surface would have looked like if the complete set of boron variation growths had been completed. It would have been likely that the grain size would have continued to increase until a point of plateau, and the orientation of the large crystals would have continued to change. However, high boron doping would have had the effect of degrading the crystal surface, and so perhaps the increased dopant level would have just had a negative effect on the morphology of the diamond surface.⁴³ As all of these samples were still more nitrogen doped than boron doped, it may have been that the nitrogen to boron ratio change caused these effects more than the change in boron level itself.

A non-dopant cause that may have also affected the surfaces of the films, is the concentration of methane present. As the concentration of methane in these growths exceeds 1% of the total source gas flow, it has been found that the methane will cause increased surface roughness of the sample.³ If the concentration of methane is not kept very low, defects on the surface can be formed.³ However, with a lower concentration of methane it is possible that the diamond wouldn't have grown at a quick enough rate to incorporate dopant clusters effectively, so these defects may not necessarily be a bad thing.

4.2.2 Film thickness

From cross-sectional SEM analysis it was categorically seen that the influence of nitrogen doping increased the growth rate, in line with the literature.²⁵ This was visually obvious and was shown in the images that make up figure 30, as the difference in thickness from the 0% nitrogen sample to the 7.5% N₂/C sample is seen.

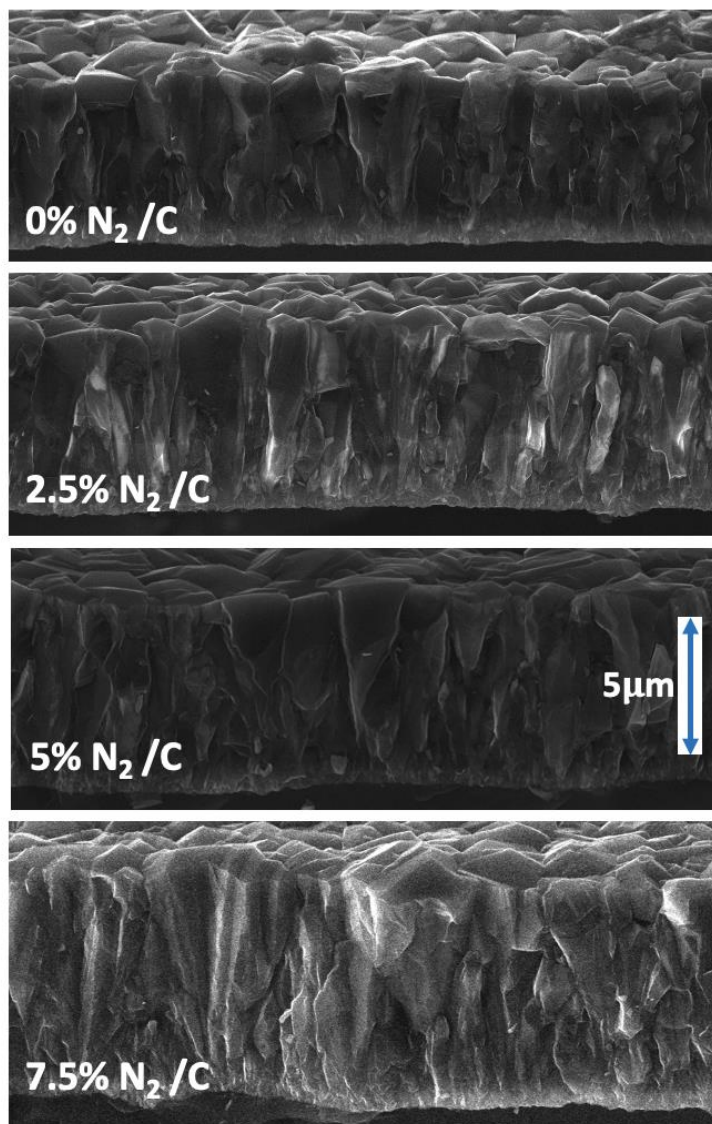


Figure 30 – SEM images showing the cross sections of diamond films with varied nitrogen concentrations at x5,000 magnification

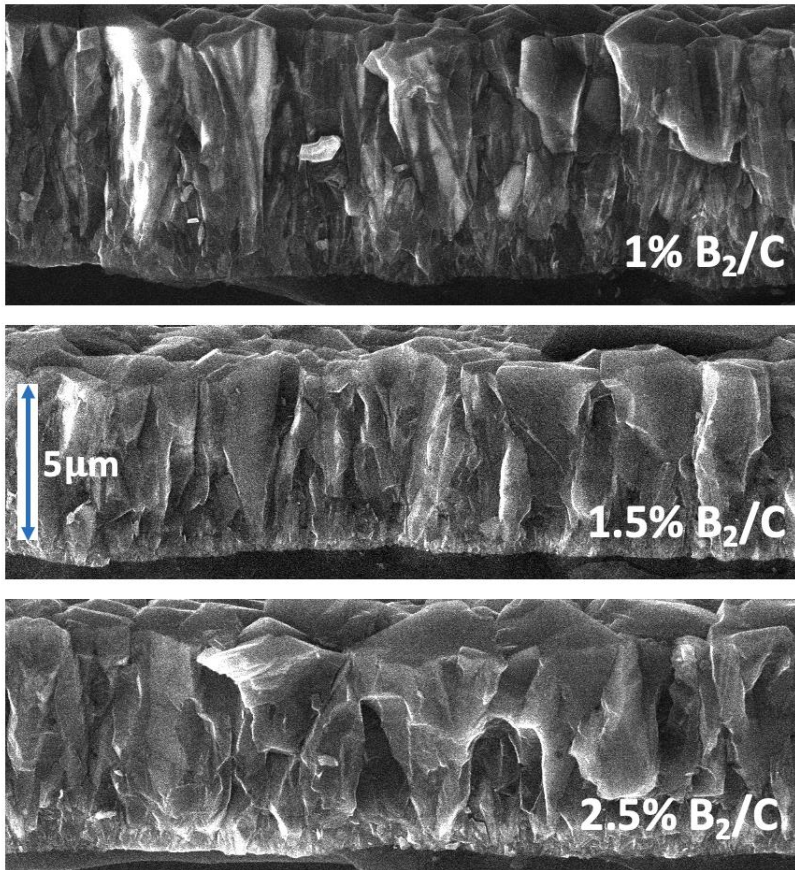


Figure 31- SEM images showing the cross sections of diamond films with varied diborane concentrations at x5,000 magnification

The effect of boron doping on the film was not as apparent as the effect of nitrogen doping to the film thickness. It appeared that the increased boron doping had little effect on the thickness or that it decreased it slightly. These observations were hard to define to just being an effect of the increased diborane concentration, as it may have been the reduced nitrogen to boron ratio, as the diborane level increased, that had more of an influence. The cross-sections of these films did display a difference to those of the nitrogen variation ones, more specifically the 2.5% B₂/C sample. It showed a dramatic and sudden increase in the surface grain size, as opposed to the more gradual 'upside-down cone' shapes seen in other samples. This may be attributed to increased B doping causing more horizontal growth effects than vertical.

Both figures 30 and 31 displayed diamond growth that fit the "columnar growth" phenomenon stated in literature.⁶¹ The images demonstrated how the diamond grains started off small, and then as they grew bigger and grew upwards, growth competition caused some grains to grow in preference to others, thus the 'upside-down cone' shape was formed. These preferential grains also then dictated the orientation of the surface.

The thicknesses of the films were plotted in figure 32 as growth rate per hour compared to the B₂ and N₂ to C percentage.

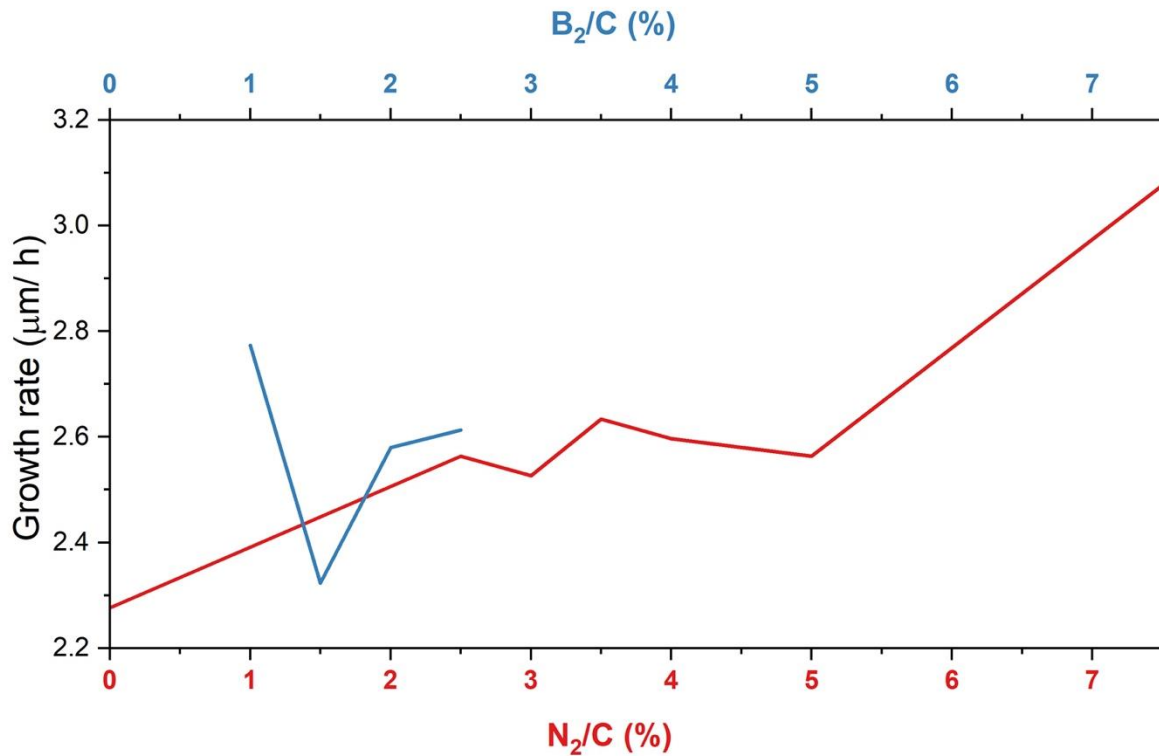


Figure 32- graph showing the comparative growth rates of diamond films in $\mu\text{m} / \text{h}$. The nitrogen varying samples are shown in red, and the boron varying samples in blue.

The diborane varying growths were not able to be completed in their entirety, and so the trend is hard to determine. The apparent general trend shown with the blue line in figure 32 was that the increasing boron level caused a decrease in the growth rate, however this could have been due to the aforementioned effect of the decreased B/N ratio. Since boron's effect upon film thicknesses is debated, the indefinite trend here was likely. As expected, and as shown in figure 30, increased nitrogen levels had a positive correlation to the growth rate. Commonly, the nitrogen concentration reaches a level where it inhibits the growth rate, so perhaps the continued increase in film thickness, despite the high nitrogen level, was due to BN cluster incorporation effects.⁶⁴

4.2.3 Substrate growth

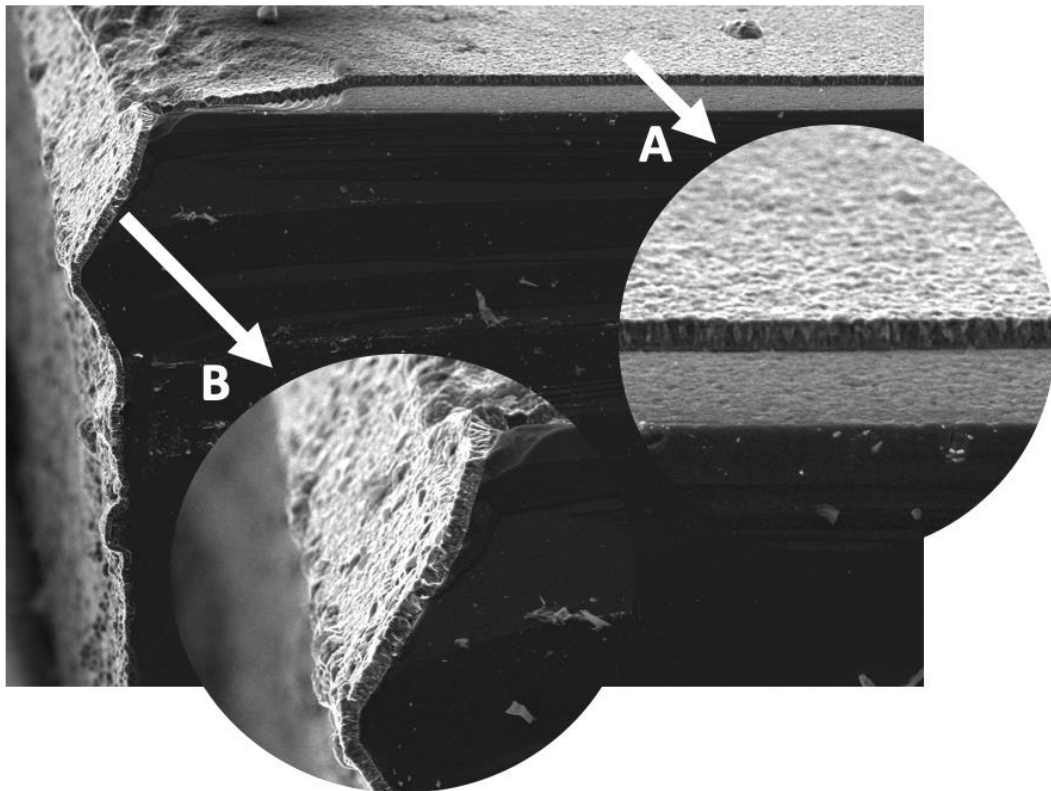


Figure 33 – SEM image showing the cross section of a silicon substrate with diamond growth at x200 magnification, a) an area of growth with the substrate prepared by manual abrasion, b) an area of growth with no preparation

The image shown in figure 33 indicated the way in which diamond grew onto a substrate. Although not relevant to the discussion of co-doping effects, this image provided some level of insight into the growth process, and therefore was worth mentioning.

Figure 33 showed that the diamond growth existed down the edge of the substrate despite the manual abrasion preparation technique that had only taken place on the surface of the silicon. The growth appeared to be similarly thick on the side, however its surface seemed much rougher and more heterogeneous than the diamond grown on the prepared surface. The smooth, more homogeneous surface magnified in figure 33a was due to good nucleation of the diamond surface from the manual abrasion preparation technique. This reinforced the necessity of good substrate preparation and showed its nucleation had an influence on the diamond growth.

4.3 Four-point probe

The samples all displayed linear relationships between current and voltage, which showed the conductivity of the samples to be ohmic, where resistance was constant despite variations in the current. The averaged measurements of each sample were plotted in figure 34 to demonstrate the linear relationship. The 4.5% and 5% N₂/C samples had average readings of the same values; therefore they had identical resistivity values.

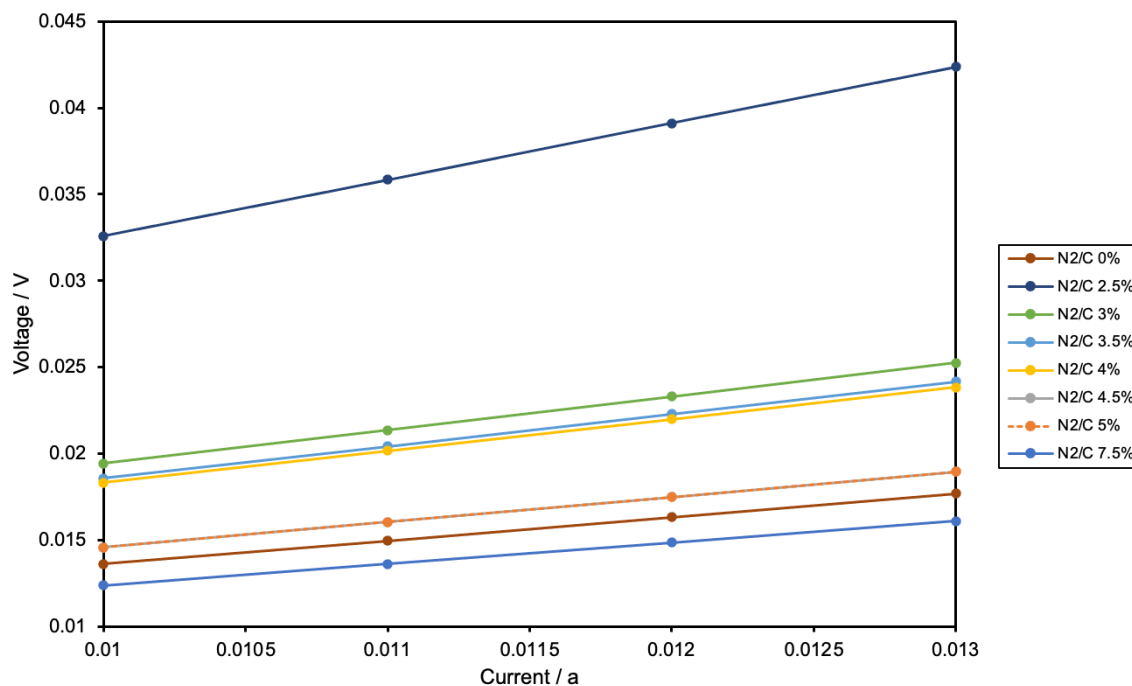


Figure 34- The averaged 4-point-probe I/V measurements for nitrogen-varying samples

NB: the 2% N₂/C sample was left out of this graph as its voltage values were so high it made viewing the discrepancies between the other lines very difficult. This graph was included in the appendix however, for completion.

The gradient of these lines determined the resistivity of the samples, and the sheet resistance was then calculated from this using the equation mentioned earlier. The boron variation samples also showed linear relationships.

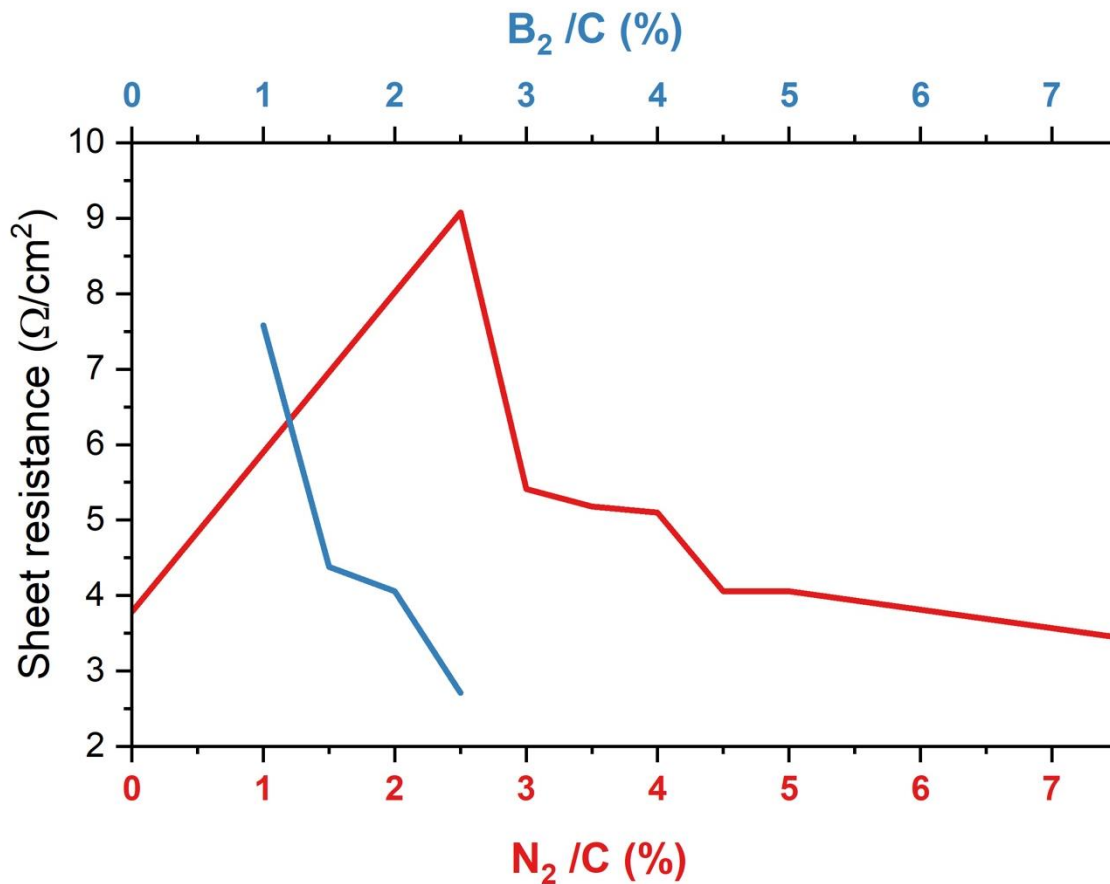


Figure 35 – comparison of sheet resistance at RTP of samples compared to their nitrogen to carbon and boron to carbon ratios. B₂/C samples are shown in blue, and N₂/C samples shown in red.

Despite the small dataset for the boron variation samples, both trends showed that increased boron and nitrogen dopant levels in N-rich samples, directly decreased the sheet resistance as indicated in figure 35. These results were consistent with repeats, thus showing this trend to be definitive at RTP. The low resistances must have occurred due to an increased defect level in the lattice, from doping.

These results agree with those produced by S. Kunuku et al, who confirmed that an increased boron doping level had the effect of decreased resistivity, thus making samples more conductive in line with the expectation for boron doping.⁴³ The sample with the lowest resistance was the sample with the highest level of B doping (2.5% B₂/C). On the other hand, nitrogen doping was not expected to have so much of an effect on the conductivity. However, the results seen here show how an initial introduction of nitrogen into the diamond lattice caused a sharp increase in the resistance, but that as the nitrogen dopant level increased further, the resistance was brought back down. The gradient of the boron variation line had a much steeper decline in resistance than those from nitrogen, however, an acknowledgement that this was not a complete dataset is necessary, conceivably as the boron level gets increased further this gradient may flatten somewhat.

The sample with the highest resistance, 2% N₂/C, was the sample with the most well integrated dopants into the diamond lattice due to SEM and Raman analysis. This proved that a cleaner diamond lattice was not conducive to high conductivities, much like pure diamond, which is a very good insulator.

4.4 Hall measurements

Hall measurements were taken despite the knowledge that these often contain a large error, consequently, these results were not comparable to other measurements taken in literature. However, despite this, the measurements were still comparable to one another and so were still a useful tool for trend determination between the samples made for this project. Excluding obvious outliers as there was significant variability, the means of the carrier concentrations recorded per sample were plotted. The mobility and resistivity values demonstrated much greater consistency so the average of each of these results was used without the need for exclusion. The values recorded for the bulk carrier concentrations are included in tables A.1 and A.2 in the appendix for further understanding into their variability, and the error bars for mobility and carrier concentration values were plotted and included in figures A.3 and A.4 in the appendix.

4.4.1 Nitrogen variation runs

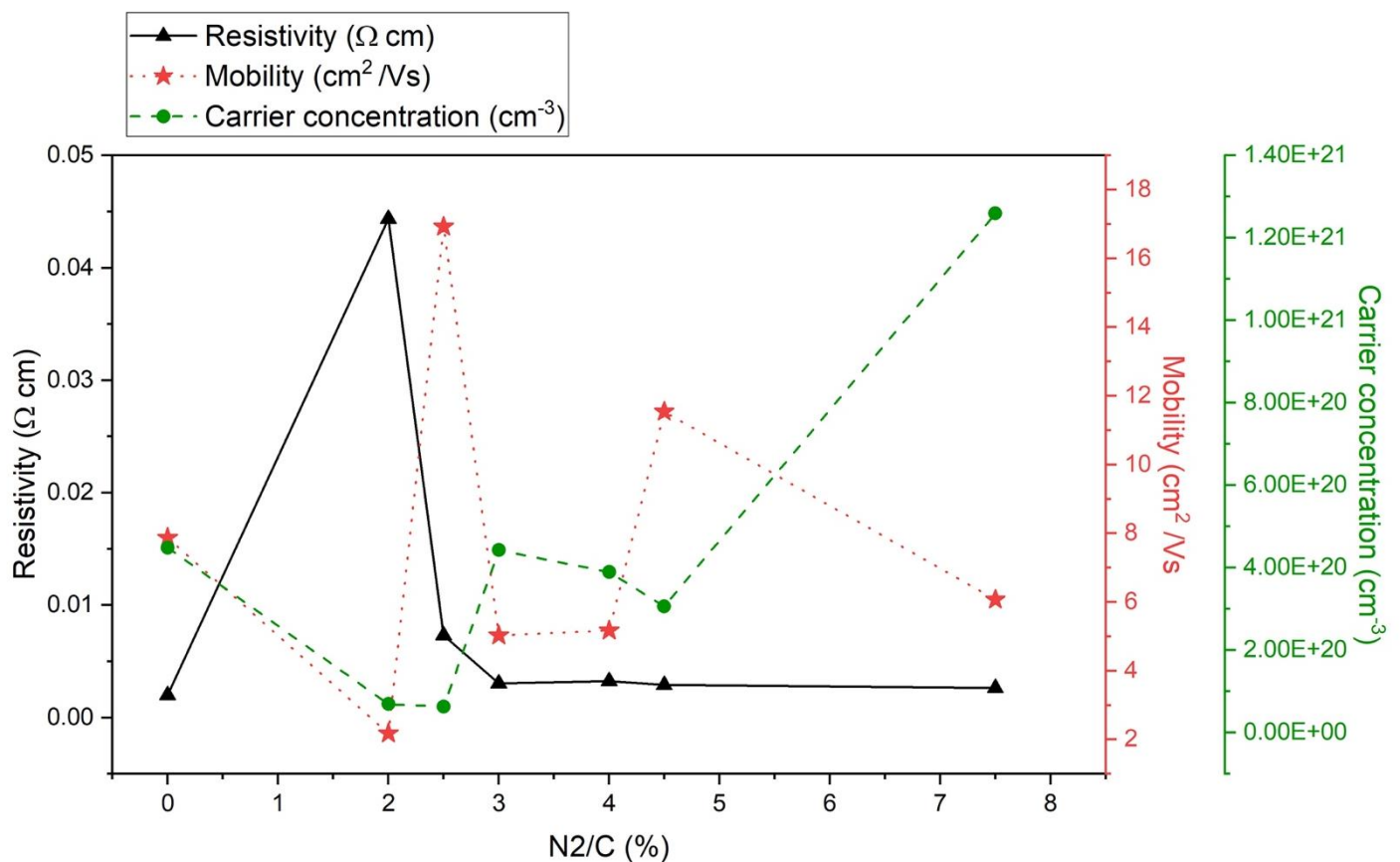


Figure 36- A graph of 3 different measurements taken of nitrogen variation samples using a Hall measurement system at RTP. Resistivity, mobility, and bulk carrier concentration are shown.

The resistivities measured by the Hall measurement system showcased the same trend as the four-point probe of a sharp increase at the 2% N₂/C sample, and then a decrease and flattening of the resistivity curve. The exact values of the resistivity differed from those recorded by the four-point probe, however, as the trend remained the same it allowed a level of trust into other trends recorded. The recorded resistivities were all very low, proving all samples to have been extremely conductive. The overall trend was that as the nitrogen doping level increased, so did the carrier concentration. This effect on the carrier concentration was explained due to increased grain boundaries from nitrogen doping.⁸

Table 6 – Bulk carrier concentration values of 2% & 4.5% N₂/C samples recorded by Ecopia Hall measurement system at 500 μA

2% N ₂ /C	4.5% N ₂ /C
6.7 E+19	1.9 E+20
8.8 E+19	- 8.8E+20
6.5 E+19	- 4.1E+20
6.5 E+19	4.3 E+20
6.2 E+19	- 1.9 E+20

The data in figure 36 showed the 2% sample to have the lowest mobility and the highest resistivity, coupled with the consistent, positive carrier concentrations recorded in table 6, this sample was definitively confirmed to be p-type. Comparatively, the 4.5% sample demonstrated low resistivity and high mobility, both of which established signs of a more n-type material when compared to the strong p-type nature of the 2% sample. Its carrier concentrations varied between positive and negative values, shown in table 6, which meant that it could not be verified as being n-type conclusively. A full list of carrier concentrations recorded is listed in the appendix, tables A.1 and A.2.

The variability in the carrier concentrations was likely due to the thermal diffusion effect of the boron doped p-type silicon substrates.^{38, 51} The J-H Seo research group demonstrated how doped substrates could be an efficient method of dopant incorporation, so it can be concluded that the substrate had the inadvertent effect of diffusing p-type carriers into the diamond lattice, which caused the positive and negative variability.⁵¹ The negative values proved that n-type carriers were present within the diamond lattice at room temperature, which demonstrated promise towards creating a permanently n-type material.

The carrier concentrations in the graph are all positive values to ensure easier comparison, however, much like the 4.5% sample's results shown in table 6, most samples showed some variation between positive and negative values. This indicated the presence of both p-type and n-type regions in the samples, either from the effect of co-doping with both p and n-type dopants, or due to the influence of the p-type substrate.

It is important to note that the 7.5% N₂/C sample included in these results was post UPS analysis and UV surface degradation explained in section 4.8. This may have meant that the

pre-UV sample with its excessive free electrons from heavy N-doping may have exhibited n-type behaviour pre surface change. This can provide an explanation as to why the mobility of this sample did not continue the upwards trend from the 4% sample onwards.

4.4.2 Boron variation runs

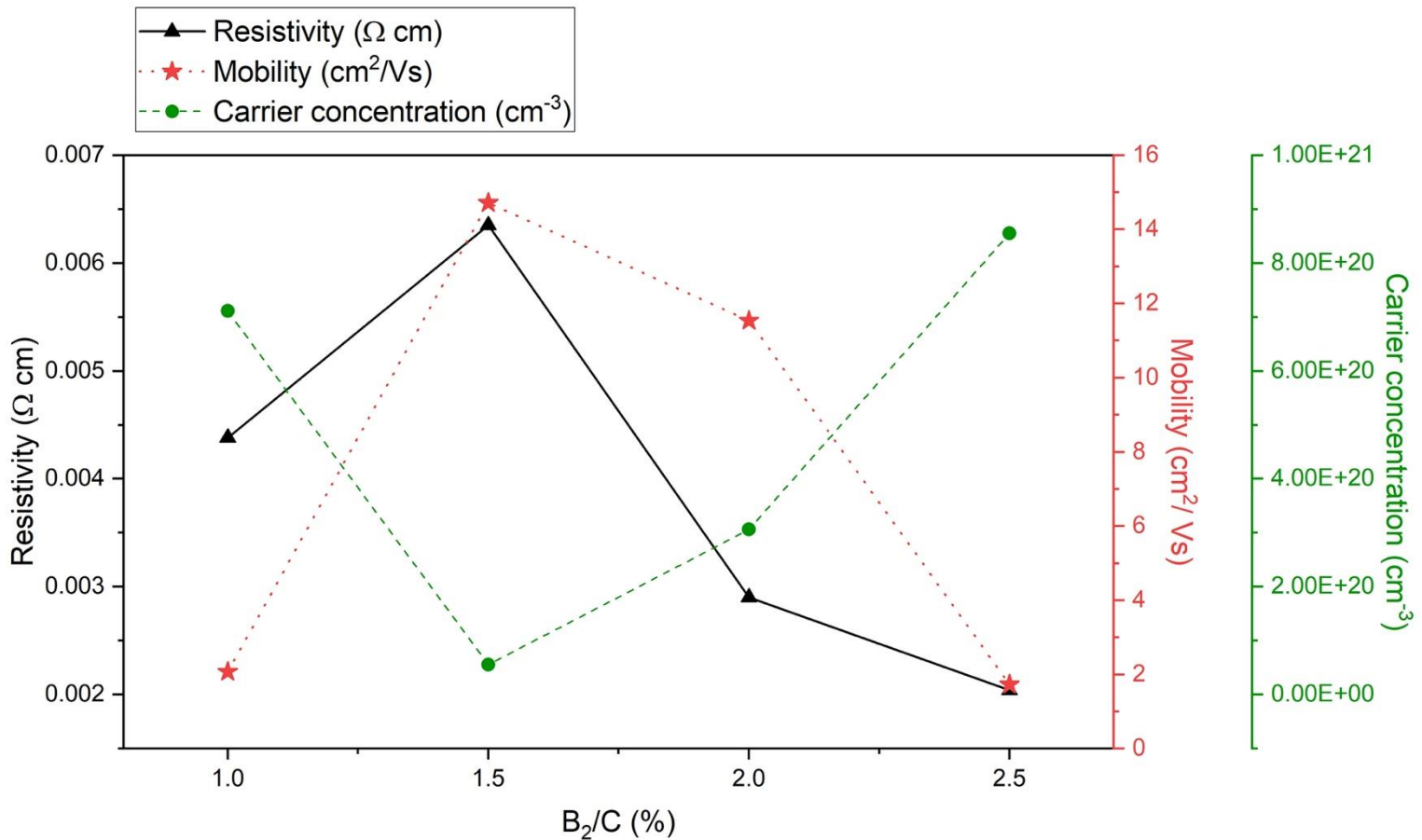


Figure 37- A graph of 3 different measurements taken of boron variation samples using a Hall measurement system at RTP. Resistivity, mobility, and bulk carrier concentration are shown.

Comparatively, the same measurements were taken of the boron variation samples which were visualised in figure 37. The resistivity trend taken here slightly varied from the measurements taken by the four-point probe, but the overall downward trend remained, and this may have been to do with contact resistance from the indium contacts. This set of results displayed a more noticeable set of trends. The resistivity and the mobility followed a similar trend of a peak at the 1.5% B₂/C sample, and then a decrease as B doping increased further. The carrier concentration had the opposite trend. It significantly decreased for the 1.5% sample to 5.6 × 10¹⁹ cm⁻³, before it returned to the order of +20 as the boron concentration increased more. The increased carrier concentration along with a low mobility at a higher B doping level, showed a characteristic p-type trend. This effect can be explained from the increased boron level, as this caused the concentration of carrier holes to increase, and hence the carrier concentration was at its highest.

For n-type characteristics of diamond at room temperature to be confirmed, a negative carrier concentration would have been needed. This reduction at 1.5% B₂/C was therefore significant, as the mobility value was also the highest, demonstrating likelihood of n-type behaviour. Despite the resistivity of this sample being the highest of the dataset, the variation is in the region of 10⁻³ which is low, and without indium contact resistance this sample recorded lower resistance with the four-point probe, thus this should not cause this sample to be discarded.

These results cannot be directly compared to those in literature mentioned previously, namely to figure 22 from the work of D.Y. Liu et al, who made n-type BNDD. The Liu group showed that at percentages of 4% N₂/C and above, the BNDD films exhibited n-type characteristics. Their films were grown on single crystal diamond and their measurements taken at 773 K, neither of which are in common with the films in this project. What was in common with D. Y. Liu, however, was that the ratio of N₂/C and the levels of hydrogen, methane and diborane were relatively similar. This may therefore show that the results from this project can give an indication of what the Liu group's results would have been at room temperature.

4.5 XPS

4.5.1 Survey spectra

The survey spectra of the samples show an overview of which atoms are present.

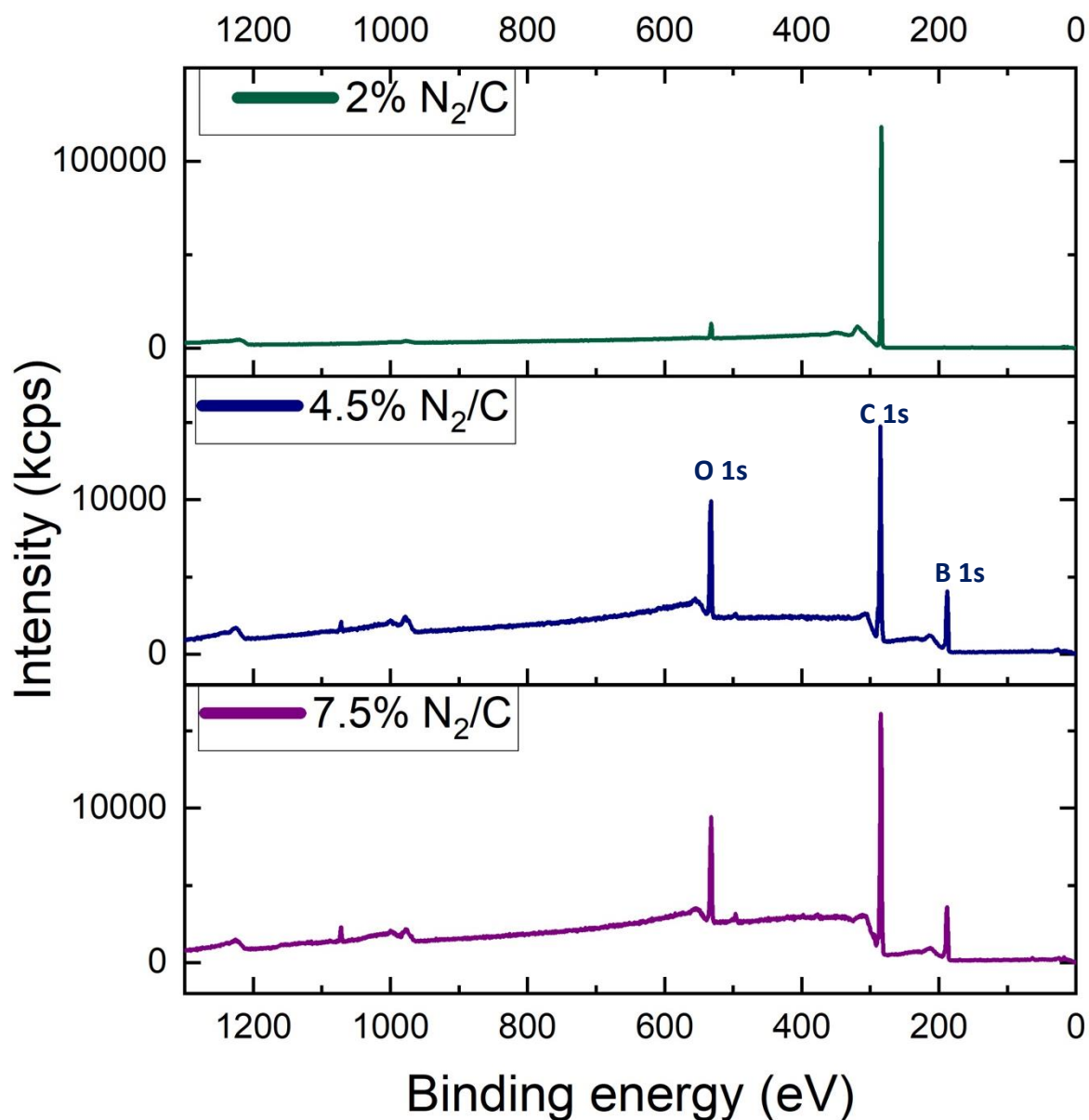


Figure 38 – stacked graphs showing the XPS survey of the 3 samples that underwent XPS analysis. The key peaks are labelled. (Top to bottom: 2% N₂/C, 4.5% N₂/C, 7.5% N₂/C) NB: the 2% graph has much greater intensity so peaks other than C 1s appear much smaller than they are.

As can be seen in figure 38 the 2 common strong peaks were C 1s and O 1s. N 1s should have existed in the region ~400 eV, however, it did not seem obvious in these samples. A plausible explanation for this could have been that the N atoms were not present on the surface of the sample, and that oxygen may have replaced the surface N as the sample was

exposed to air. The level of oxygen present was relatively large compared to the level of carbon present, the difference between the level of oxygen and the level of carbon present was largest in the 2% N₂/C sample, leading to the postulation that the increased level of nitrogen meant a smaller amount of carbon present and a larger presence of oxygen due to the nitrogen-vacancies produced.

4.5.2 C 1s spectra

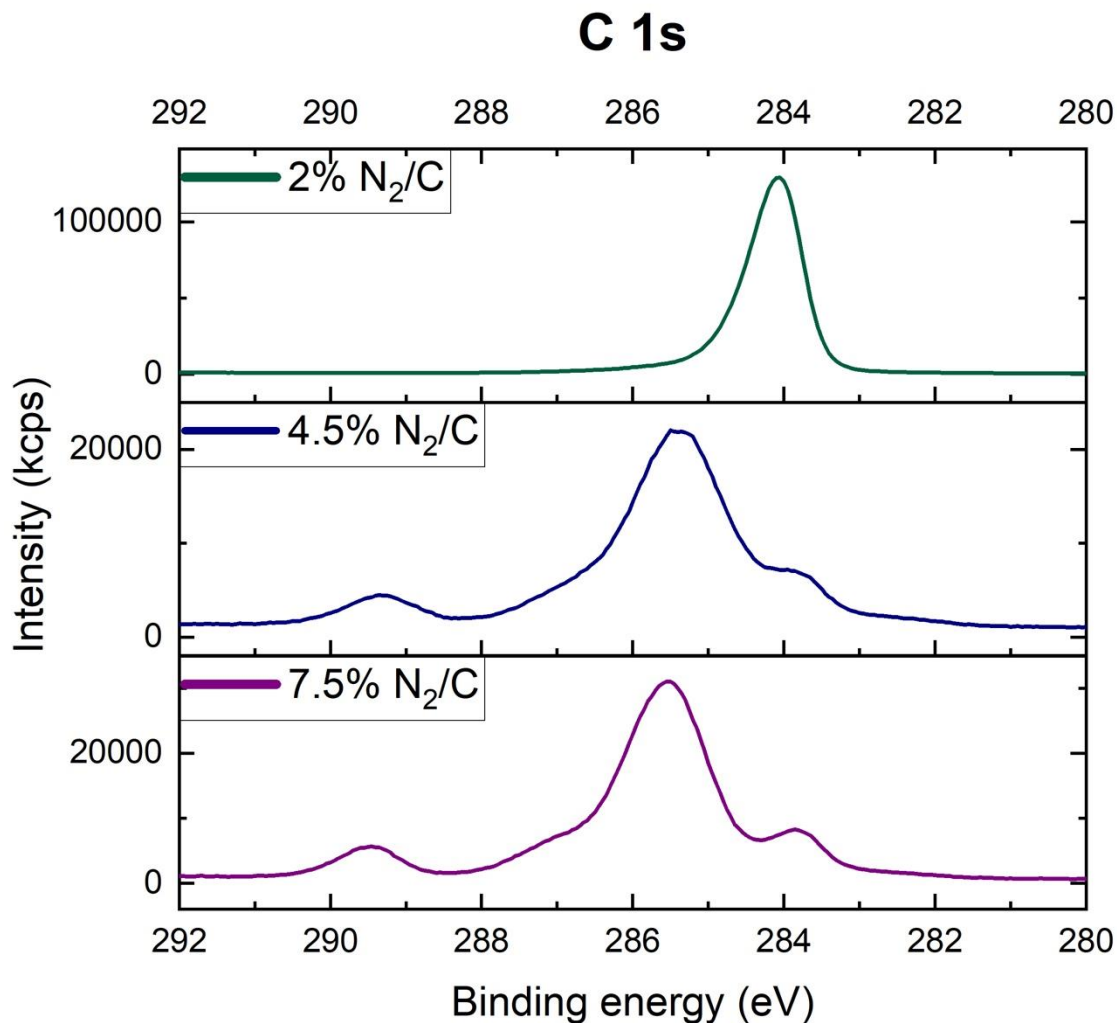


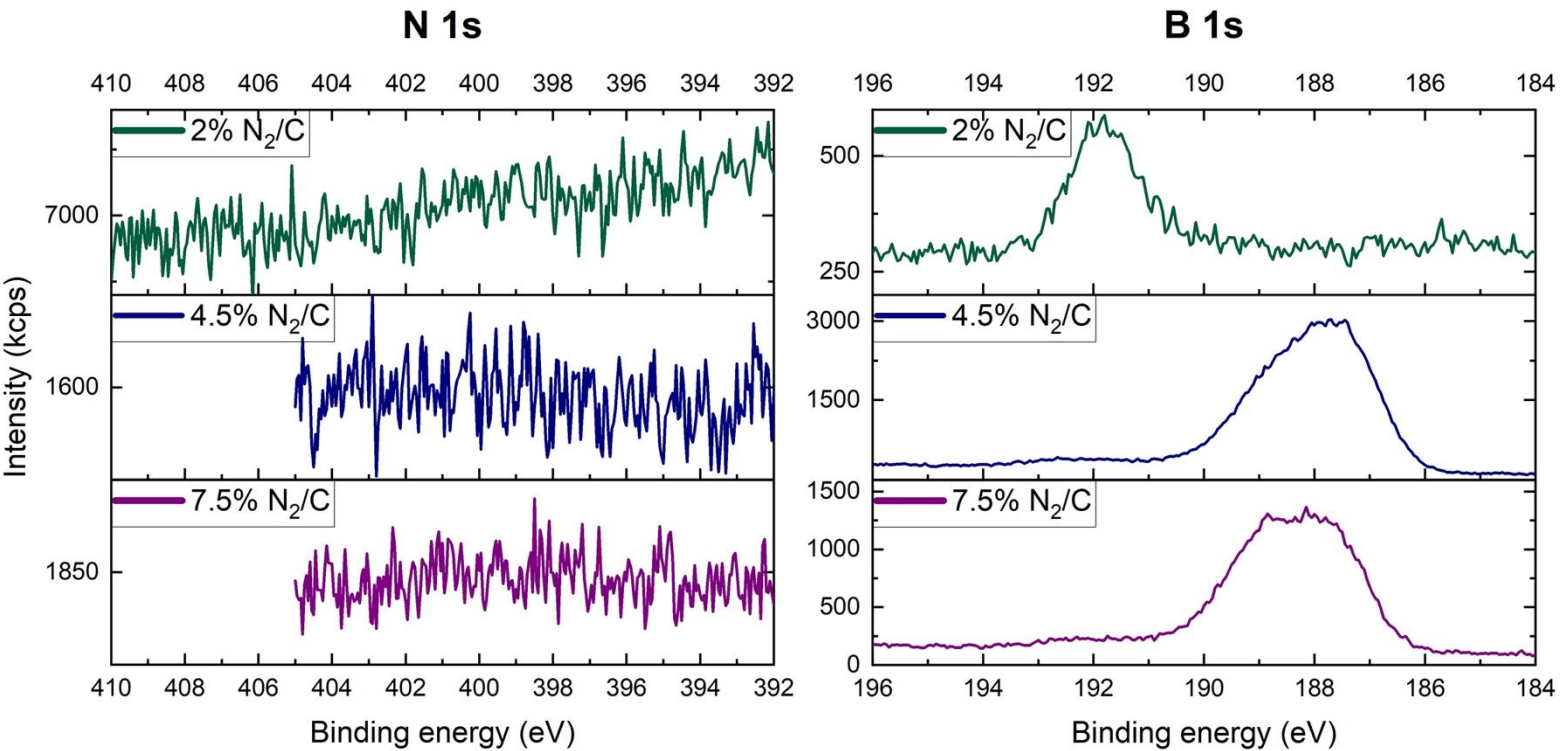
Figure 39- graphs showing the XPS peaks of the C 1s atoms in 3 BNDD samples

As can be seen in figure 39, the 2% N₂/C sample had a very strong C-C peak, and no other interference in the carbon bonding, which indicated a strong sp³ carbon diamond lattice. This showed a definitive diamond sample peak and reinforced the aforementioned idea that the dopant incorporation shown in figures 25 and 27 was of a perfect level to not disrupt the diamond lattice.

The 4.5% and 7.5% N₂/C samples, however, showed the carbon to be bonded in other ways too. The C-C bond peak was shifted slightly higher in energy, and this could have been due to dopant incorporation, as the C-N and C-O peaks were found to be at 286 eV, so these may have been included within this broad diamond peak.⁷⁶ The peaks between 289-290

refer to C=O, which showed the oxygen exposure to have disrupted the diamond lattice only at higher dopant concentrations.⁷⁶

4.5.3 N 1s and B1s spectra

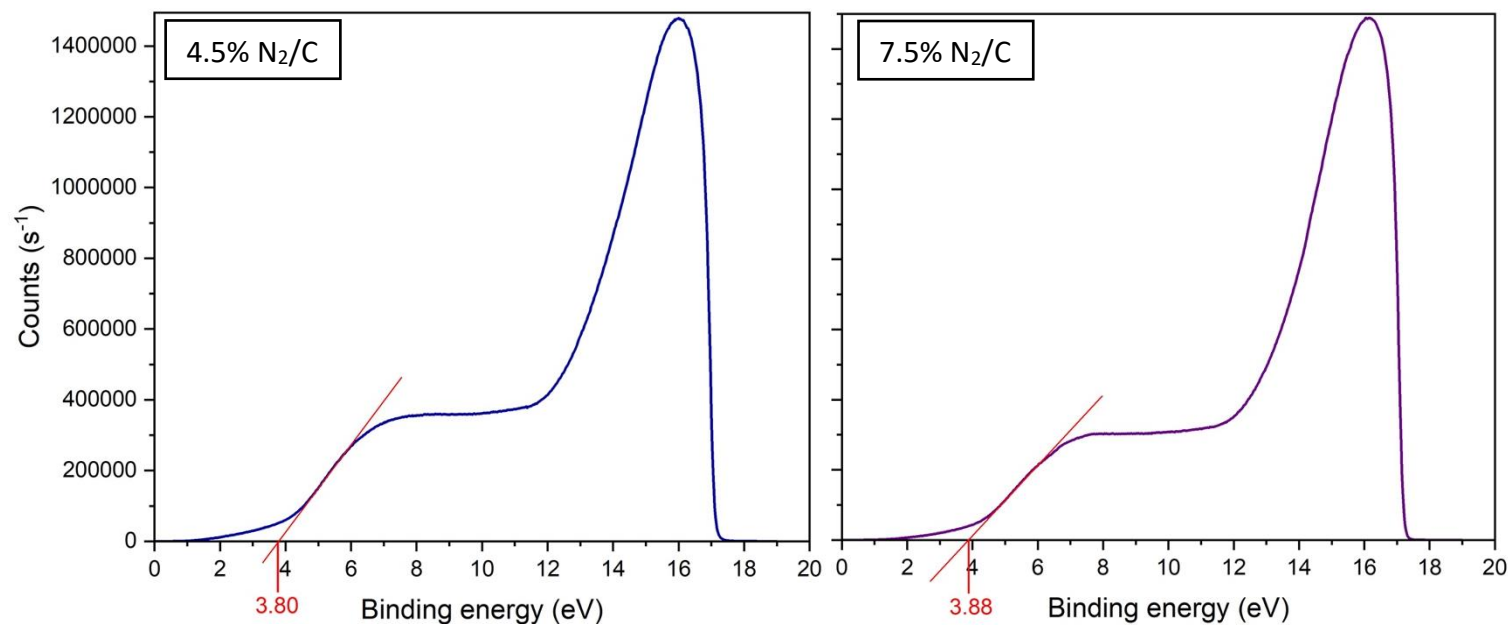


Figures 40 & 41- N 1s and B 1s atom bonding in 3 BNDD samples that underwent XPS analysis

The XPS spectra showed how boron atoms were definitively present in the diamond lattice, but nitrogen was not obviously present from its spectra. It had been seen before on the nanoESCA used for these measurements that nitrogen often did not show a strong peak, so this was not of concern, not proving that nitrogen was not present.⁷⁷

4.6 UPS

4.6.1 Valence band maxima



Figures 42 & 43 – UPS curves for L) 4.5 N₂/C and R) 7.5% N₂/C. The VBM is labelled in red where the tangent crosses the x-axis.

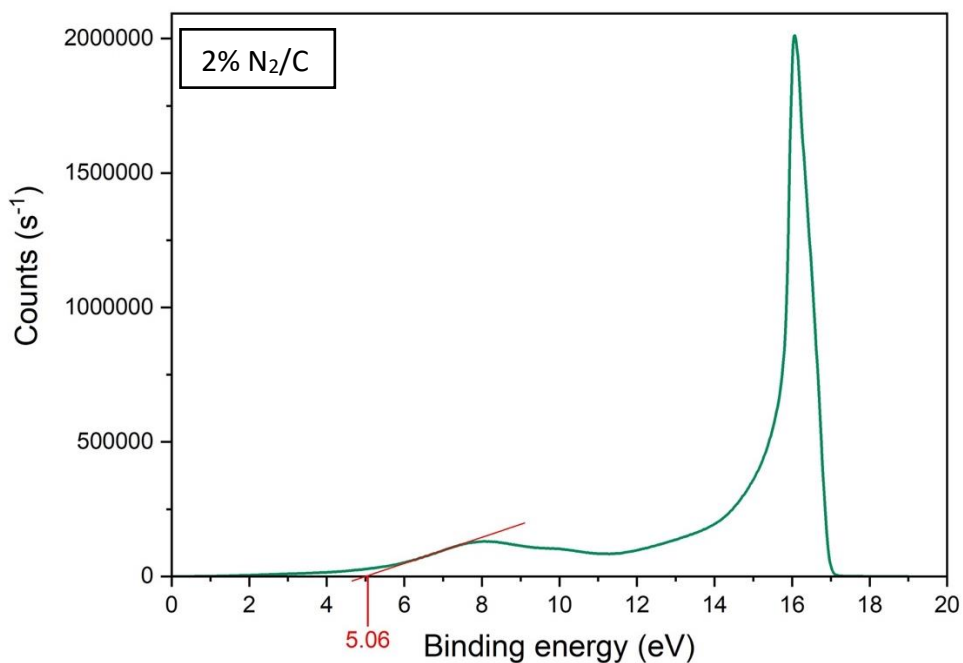
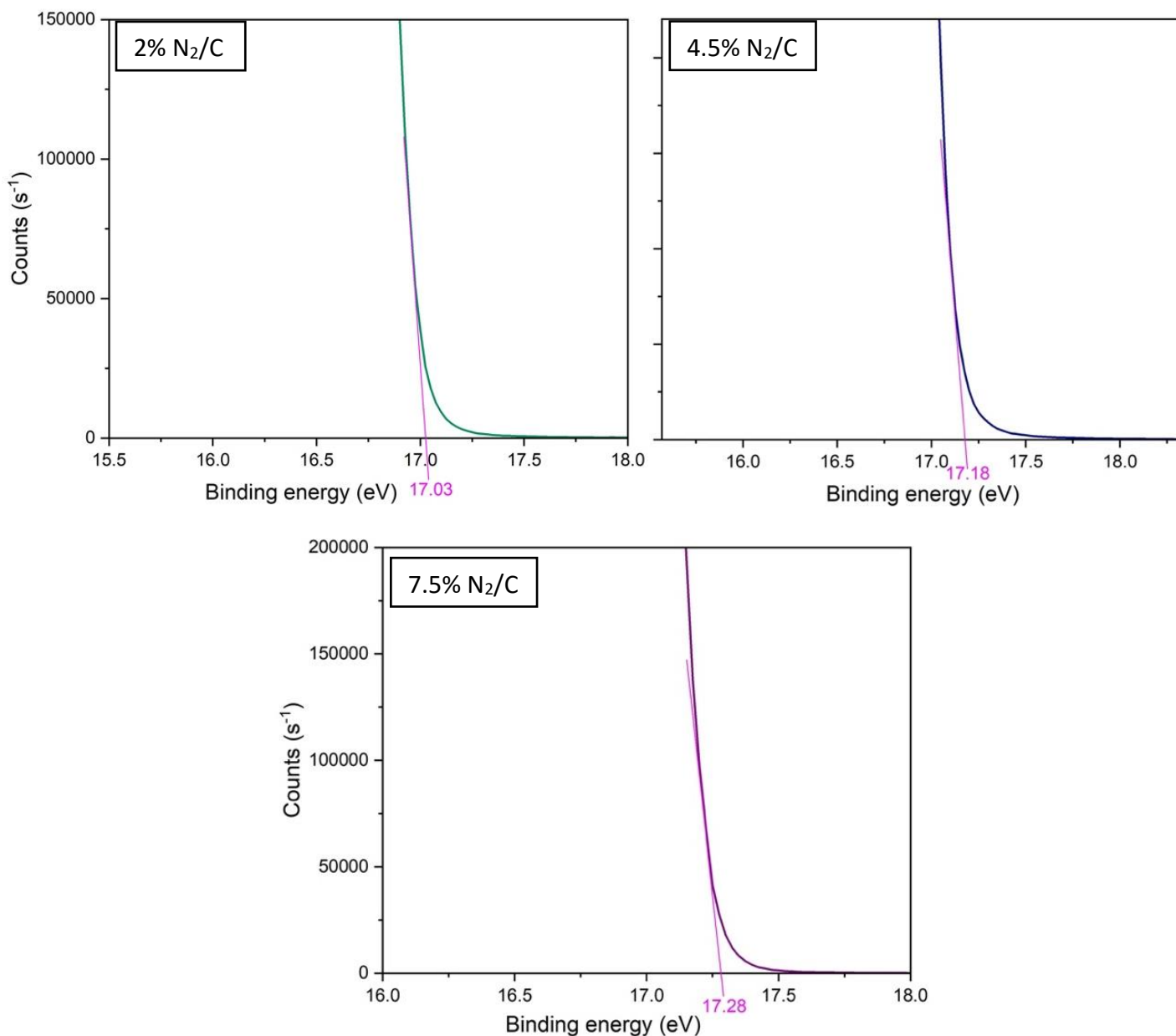


Figure 44- UPS curve of 2% N₂/C sample. VBM labelled in red where the tangent crosses the x-axis.

4.6.2 Work functions



Figures 45, 46, 47 – The tangentially found high-energy cut-off points for 2, 4.5 and 7.5% N₂/C samples labelled in pink.

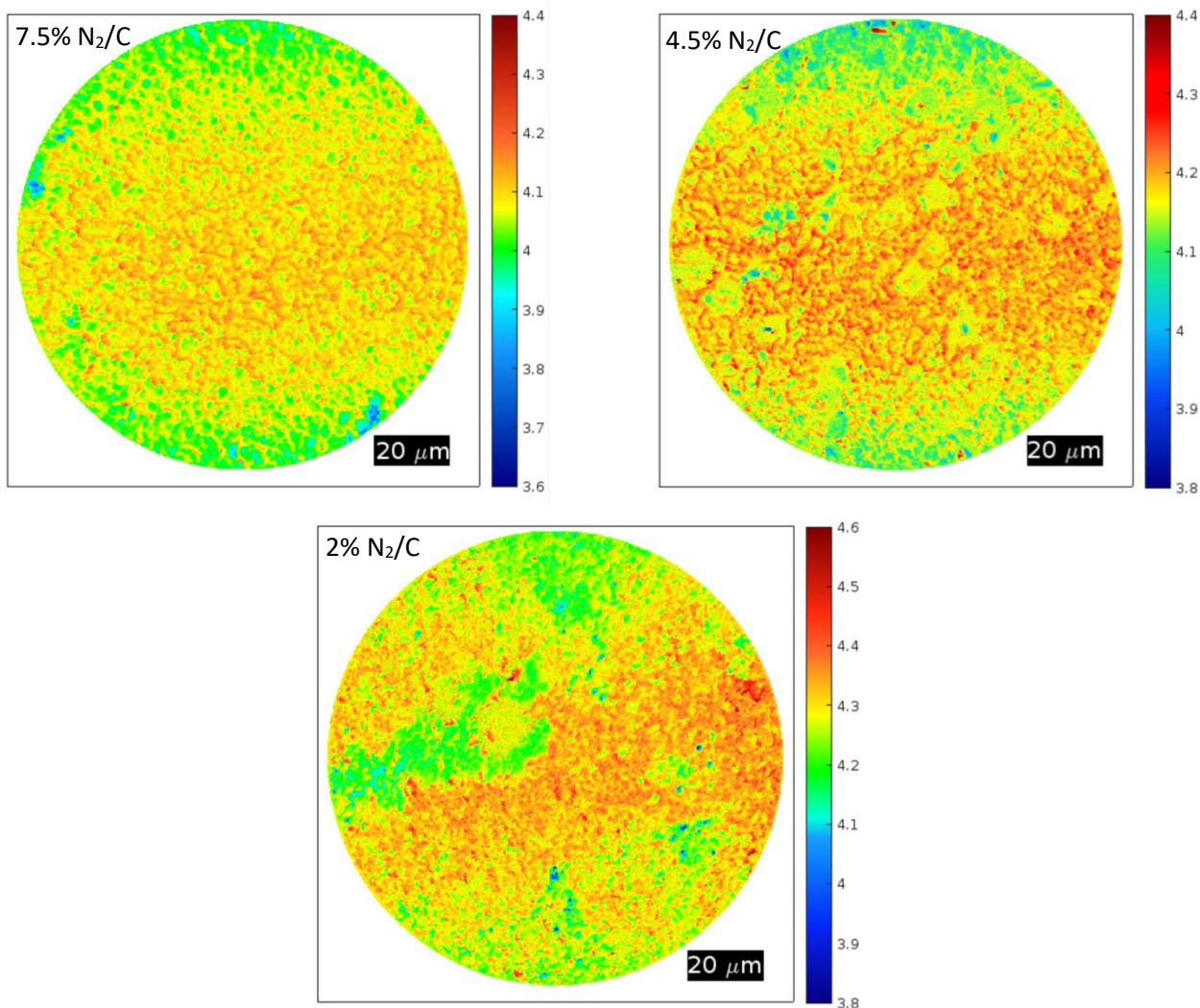
The work function was calculated by finding the tangent of the secondary electron peak, and this was found to be the “high-energy cut-off”. This was labelled in pink on the graphs. The work function was the difference between the high-energy cut-off and the UV source energy (21.2 eV for the monochromatic He I used). This gave us WF: 4.17, 4.02, 3.92 eV respectively for 2%, 4.5% and 7.5% N₂/C samples. There was therefore a steady decrease in the WF of the diamond thin film layer as the concentration of nitrogen increased. The WF of pure diamond has been found to be 6.1 eV, which showed that the addition of dopants caused a decrease in the work function.^{66, 78} The calculated VBM and WF are shown in table 7.

Table 7- The valence band maxima and work functions of BNDD samples with increasing level of nitrogen doping

N₂/C	Valence Band Maximum (eV)	Work Function (eV)
2%	5.06	4.17
4.5%	3.80	4.02
7.5%	3.88	3.92

Increased levels of n-type doping would have been expected to have decreased the work function which was demonstrated here.³⁷ This showed that despite the nitrogen not showing up in the xps spectra, there was nitrogen present as its n-type doping had varied the work function. The same thing can be said for valence band maximum. As it reduced, it became further away from the fermi energy level, which is also consistent with n-type doping. Up until this point there did not appear to be published work especially focused on BNDD and the effect that varying dopant concentrations had on VBM and WF, therefore these trends should be confirmed under different growth conditions.

4.7 PEEM



Figures 48, 49, 50 – Heat maps showcasing the variable WF across each sample recorded with PEEM and plotted using MATLAB. Y.1 = 7.5% N₂/C, Y.2 = 4.5% N₂/C, and Y.3 = 2% N₂/C

NB: the heat maps have differing colour scales on the side as they were plotted to ensure that the contrast between different areas was evident on a sample-by-sample basis.

The heat maps shown in figure y indicated how the surface of the films was not homogeneous, and how the WF measured from the tangent of the graph was not definitive of the WF of the entire surface. Focusing initially on the 7.5% N₂/C sample, which was expected to have WF of 3.92 eV by the tangential analysis, the heat map showed green (~4 eV) to have dominated the bulk of the surface. The position of the green 4 eV WF areas were scattered around the surface, leading to the conclusion that these could have been caused by a specific dopant impurity, with the orange areas of a higher WF that surrounded the green, caused by another dopant. It was difficult to definitively associate a specific WF to a specific atom but based upon the previous theory that n-doping lowers the WF, a hypothesis could be that the green areas were dominated by N doping. Since there were

also a couple of even lower WF blue areas, it may have been that these were more likely represent the N doping as the absence of N in the XPS spectra owed to its surface presence not being large.

The 4.5% and 2% N₂/C samples showed more clusters with the same WF than the more spread out 7.5% N₂/C sample. The same discussion surrounding areas of different WF corresponding to different areas of dopants can be applied. Again the 4.5% sample showed a higher dominant WF on the map (~4.15 eV) than from the UPS graph tangent (4.02 eV). This was likely due to errors when the tangent was measured, but also it was important to note that the area of the sample that underwent PEEM analysis was smaller than that for UPS analysis, and so the snapshot of the sample shown in these heat maps did not define the entire sample surface.

The 2% sample, however, had a dominant heat map WF (~4.2 eV) that approximately matched the value found from the tangent (4.17 eV). This was most likely due to the large cluster of this WF that was clearly visible on the sample surface, which caused the average WF to match. The WFs across this sample were the most heterogeneous, with values stretching from ~3.8 eV up to ~4.6 eV, positioned in a random way. It was interesting to see this since its SEM surface analysis showed such a distinct “checkerboard” pattern due to the dopant incorporation, demonstrating that the electron beam in SEM has much stronger capabilities when viewing surface discrepancies than UV photons.

4.8 UV surface effects:

An unusual effect was recorded after UV exposure to the sample with the highest nitrogen doping. As was indicated in figure x, the after UPS line in red showed a change in the C bonding. The peaks for each line were labelled. As seen in figure x, the effect of the UV on the sample was predominantly the reduction of the surface oxygen, and the increased surface graphite. A hypothesis can be drawn that the UV has graphitised the diamond surface to some extent, potentially from the expulsion of surface oxygen due to UV. Thus, it may be assumed that the carbon that was once bonded to oxygen, latterly formed sp^2 C=C graphitic bonds. This was only observed for the highly nitrogen doped sample, which strengthens the argument against nitrogen doping of this level, as its structure was not wholly robust. Published literature indicates that UV exposure during growth suppressed diamond deposition, a finding that may be used to further this hypothesis.⁷⁹

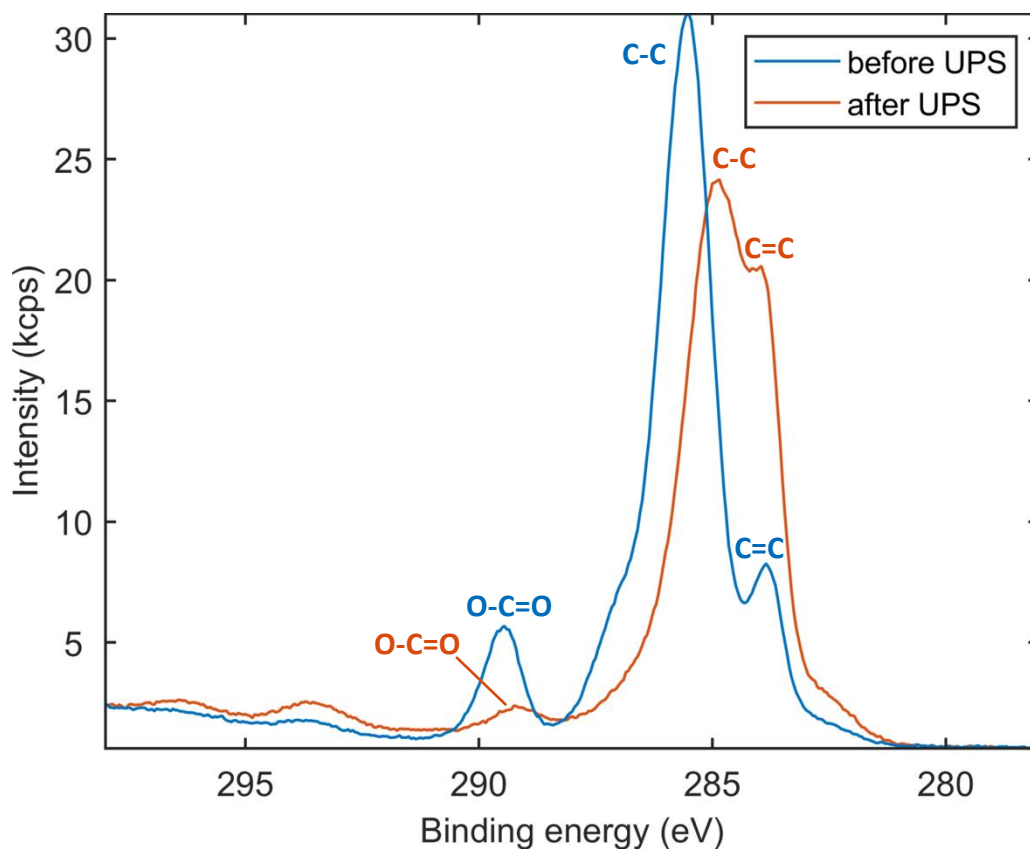


Figure 51- XPS analysis showing the effect of UV exposure from UPS analysis on the C 1s atom in the 7.5% N₂/C sample. Blue: original XPS C1s analysis, red: post-UPS XPS C1s analysis

5 Conclusions and future work

5.1 Conclusions

The effect of nitrogen doping on BNDD is relatively well researched, and the results from this project agree with most literature values and trends. Nitrogen doping was shown to accelerate the growth rate of films as expected, whereas boron doping had little to no effect on growth rate, but overall caused a slight decrease. Despite not having a large increase in the thickness of the films, increased boron doping enlarged the individual grain sizes within the films significantly compared to nitrogen doping. It therefore seems that boron doping has more of an effect upon the surface structure of the diamond films than nitrogen doping does. This was demonstrated in the cross-sectional SEM images in figure 31, as the columnar growth showed grains to grow more quickly horizontally, rather than vertically, when the concentration of B atoms was increased, compared effects from increased N atoms. S Kunuku et al indicated that at high B concentrations, N is less well incorporated into the diamond lattice which may explain the increased effects boron has on the surface.⁴³

As expected, increased boron doping had the effect of decreasing the resistance of the films, and therefore shows increased boron doping to increase the conductivity of BNDD. This is in line with results also achieved by S. Kunuku et al.⁴³ The effect of increased nitrogen doping also exhibited a decrease in the resistance of the samples, in line with the work of E. Requena, whose work this project followed. This increased conductivity effect from the n-type dopant nitrogen, may be due to the increased level of free electrons in the diamond lattice enhancing the conductivity of the sample. The extent of the decreases in sheet resistance appears to be much stronger for the increased B doping as the gradient of the line showed a much steeper decrease. The effect of the increased holes from B doping therefore has a much stronger effect on the conductivity than N doping, and this is in line with expectations. Despite the smaller dataset for B doping changes, the results are believed to be definitive, as they confirm expected trends. These results also demonstrate that nitrogen doping is not detrimental to the conductivity of a sample, instead having a positive effect.

Due to the adverse surface effects from UV on the heavily N doped (7.5% N₂/C) sample, it may be concluded that this isn't a feasible dopant level due to its instability. This "UV effect" may have come about due to excessive oxygen incorporation onto the surface of the sample, perhaps due to NV centres, so a termination step may be necessary in future to mitigate this. The 7.5% N₂/C ratio was seen to exhibit n-type characteristics at 773K in Liu et al's work, so a more promising result was expected out of this sample, as its inclusion into the dataset was due to this n-type characteristic. From this it can be concluded that high N-doping only contributed to n-type behaviours at higher temperatures and was not beneficial at room temperature. The change in surface bonding from UV may be attributed to the lack of BN clusters present, as well integrated, strong bonds would be expected to be more chemically stable under UV irradiation.

UPS analysis showed the work function and the valence band maximum to both conclusively reduce due to increased N-doping. This effect with BNDD is not documented widely within literature, and so these results can help to provide improved understanding of the way that the band structure of BNDD is influenced by dopants. The PEEM data showed the diversity

of electron environments on the diamond surface due to dopant atoms, which helped to confirm that the BN doping was present and had an effect. Since N atoms were not obvious from the XPS spectra, the changes in WF and VBM are indicative of n-type doping, and validate that N exists within the diamond lattice.

Despite dopant incorporation being apparently most effective in the 2% N₂/C sample, due to the “checkerboard” effect seen from SEM imaging, it was the least conductive sample and the most firmly p-type sample by Hall measurements. This perhaps can prove that well integrated dopants are not conducive to n-type materials, as perhaps the excess electrons from n-type dopants are required to be freer and not as strongly bonded to maximise their n-type properties. It may be that the well-integrated dopants are just BN clusters within the diamond lattice, not N rich clusters, hence the p-type characteristics displayed.

The variability in the Hall measurements cannot be attributed to definite categorisation of p or n-type substrates for the most part. The 2% N₂/C sample, however, showed definitively p-type characteristics which fitted with earlier analysis to strongly conclude this. The composition of this sample was 0.5 sccm of both N₂ and B₂H₆, but with acknowledgment to the residual boron in the reactor, this sample was most likely more B-doped than N-doped. The most promising n-type samples were the 1.5% B₂/C sample, and 2% B₂/C, which had the same composition as the 4.5% N₂/C sample. The obtained Hall measurements for these samples demonstrated high mobility values coupled with low carrier concentration and low resistivity, which when compared to their obvious p-type counterparts, indicated propensity for n-type characteristics. Since the carrier concentration measurements were so variable between positive and negative, and recognising the tendency for unreliable Hall measurements from the large error bars plotted in A.3 and A.4, no firm conclusions could be drawn. Nevertheless, in these samples negative values dominated the carrier concentration readings, and accounting for the strong effect from the p-type silicon substrate likely providing the positive values, it is probable that some n-type behaviour is present within the diamond lattice at room temperature. Until these dopant concentrations are tested on undoped substrates, however, a definite result cannot be reached, only speculation.

5.2 Future work

Further analysis on this project could utilise SIMS to receive a depth profile of the sample and confirm the presence of nitrogen in lower layers. This would also allow a more extensive analysis of the samples and where in the sample’s depth each dopant dominates.

Following on from this project, the diborane concentration range should be expanded to its full scope to confirm the trends of increasing boron dopant levels. This would allow a stronger picture of the effect that boron has in BNDD and could confirm the points at which its p-type characteristics dominate. It would be beneficial also to explore more concentrations surrounding the 4.5% N₂/C sample varied around in this project, as this demonstrated great potential towards the creation of an n-type material.

UPS and PEEM analysis on a dataset varying boron concentration would allow further insight into the effects that boron has on the band structure in BNDD. Unfortunately, this wasn’t

possible within the time frame of this project, but a follow-on project may want to investigate this.

Diamond growth should also be explored on a single crystal diamond substrate, to ensure that the p-type characteristics of the silicon substrate does not dominate the carrier concentration through Hall measurements. Conversely, an N-doped substrate such as the Si_3N_4 substrate used by Y. Yang et al, could provide increased n-type doping through thermal diffusion between the substrate and diamond layer.³⁸

A further project could explore the use of N_2O over N_2 as a dopant gas. Current published literature cites nitrous oxide as being more effectively incorporated into the diamond lattice, with low donor concentration and it therefore could improve the electrical performance of BNDD due to increased hole mobility.⁶⁰ It has been found that utilising N_2O over N_2 can limit macroscopic defects formed, improving the stability of nitrogen vacancy centres.⁷⁴

This work demonstrated high nitrogen doping to cause adverse effects due to excessive oxygen incorporation. As high N doping showed n-type characteristics at 773K, exploration into a terminated sample at RTP may exhibit more n-type behaviour.

Further work could be also conducted to explore the UV surface effects of highly doped CVD diamond. This wouldn't contribute to the exploration of n-type diamond, but it is an interesting feature that is unusual and doesn't seem to be explored in other literature. Samples could be made that are highly doped with many different dopants to explore how their diamond structure reacts to heavy UV exposure, and how purposeful termination with hydrogen gas for example, might mitigate this.

6 References

1. M. Hu, N. Bi, S. Li, T. Su, Q. Hu, H. Ma and X. Jia, *Cryst. Eng. Comm.*, 2017, **19**, 4571-4575.
2. V. Blank, M. Popov, G. Pivovarov, N. Lvova and S. Terentev, *Diamond and Related Materials*, 1999, **8**, 1531-1535.
3. D. Araujo, M. Suzuki, F. Lloret, A. Gonzalo and P. Villar, *Materials*, 2021, **14**, 7081.
4. J. E. Field, *The Properties of Natural and Synthetic Diamond*, Academic Press, London, 1992.
5. P. W. May, *Phil. Trans. R. Soc. Lond.*, 2000, **358**, 473-495.
6. A. Gicquel, K. Hassouni, F. Silva and J. Achard, *Current Applied Physics*, 2001, **1**, 479-496.
7. M. Seal and W. J. P. v. Enckevort, 1989.
8. K. Kobashi, K. Nishimura, Y. Kawate and T. Horiuchi, *Physical Review B*, 1988, **38**, 4067-4084.
9. S. Witt, A. Rogien, D. Werner, J. Siegenthaler, R. Lesiyon, N. Kurien, R. Rechenberg, N. Baule, A. Hardy and M. Becker, *Diamond and Related Materials*, 2021, **118**, 108542.
10. J. H. Kaneko, T. Tanaka, T. Imai, Y. Tanimura, M. Katagiri, T. Nishitani, H. Takeuchi, T. Sawamura and T. Iida, *Nuclear Instruments and Methods in Physics Research Section A: Accelerators, Spectrometers, Detectors and Associated Equipment*, 2003, **505**, 187-190.
11. Y. Miyake, T. Kondo, A. Otake, Y. Einaga, T. Tojo and M. Yuasa, *Acs Sustainable Chemistry & Engineering*, 2023, **11**, 8495-8502.
12. C. Y. Fong and B. M. Klein, *Diamond: Electronic Properties and Applications*, Springer Science + Business Media, LLC, New York, USA, 1995.
13. B. G. Yacobi, *Semiconductor Materials*, Springer, New York, NY, 1 edn., 2003.
14. G. G. Hall, *The London, Edinburgh, and Dublin Philosophical Magazine and Journal of Science*, 1952, **43**, 338-343.
15. I. V. Popov, A. L. Gorne, A. L. Tchougreeff and R. Dronskowski, *Phys. Chem. Chem. Phys.*, 2019, **21**, 10961.
16. R. Nemanich, J. Carlisle, A. Hirata and K. Haenen, *MRS Bulletin*, 2014, **39**, 490-494.
17. A. Mezzi and S. Kaciulis, *Surf. Interface Anal.*, 2010, **42**, 1082-1084.
18. M. N. Ashfold, P. W. May, C. A. Rego and N. M. Everitt, *Chem. Soc. Review*, 1994, **23**, 21-30.
19. C. M. Breeding and J. E. Shigley, *Gems & Gemology*, 2009, **45**, 96-111.
20. I. M. Buckley-Golder and A. T. Collins, *Diamond and Related Materials*, 1992, **1**, 1083-1101.
21. Y. A. Sorb, F. P. Bundy and R. C. DeVries, *Reference Module in Materials Science and Materials Engineering*, 2016.
22. S. Scandolo, M. Bernasconi, G. L. Chiarotti, P. Focher and E. Tosatti, *Physical Review Letters*, 1995, **74**, 4015-4018.
23. S. Veljković, V. Mitic, V. Paunovic, G. Lazovic, M. Mohr and H. J. Fecht, *Serbian Journal of Electrical Engineering*, 2020, **17**, 111-129.
24. A. C. Jones and M. L. Hitchman, *Chemical Vapour Deposition: Precursors, Processes and Applications*, RSC Publishing, UK, 2009.
25. A. Croot, Doctor of Philosophy, University of Bristol, 2018.

26. G. Pastor-Moreno, Doctor of Philosophy, University of Bristol, 2002.
27. *US Pat.*, 1962.
28. M. Hiramatsu, K. Murata, M. Naito, S. Takashima, H. Kondo and M. Hori, *Radical density measurements in microwave plasma with carbon-containing gases used for carbon nanotube and nanocrystalline diamond film growth*, Meijo University, Nagoya University, Japan, 2014.
29. B. V. Spitsyn, L. L. Bouilov and B. V. Derjaguin, *Journal of Crystal Growth*, 1981, **52**, 219-226.
30. M. Chandran, in *Carbon-Based Nanofillers and Their Rubber Nanocomposites*, eds. S. Yaragalla, R. Mishra, S. Thomas, N. Kalarikkal and H. J. Maria, Elsevier, 2019, pp. 183-224.
31. Y. Bar-Yam and T. D. Moustakas, *Nature*, 1989, **342**, 786-787.
32. H. Kato, M. Ogura, T. Makino, D. Takeuchi and S. Yamasaki, *Appl. Phys. Lett.*, 2016, **109**, 142102.
33. A. Dychalska, P. Popielarski, W. Franków, K. Fabisiak, K. Paprocki and M. Szybowicz, *MATERIALS SCIENCE-POLAND*, 2015, **33**.
34. P. A. Cox, *The Electronic Structure and Chemistry of Solids*, Oxford University Press, Oxford, UK, 1987.
35. A. Kahn, *Materials Horizons*, 2016, **3**, 7-10.
36. D. Sarkar, X. Xie, J. Kang, H. Zhang, W. Liu, J. Navarrete, M. Moskovits and K. Banerjee, *Nano Letters*, 2015, **15**, 2852-2862.
37. H. Yoo, K. Heo, M. H. Ansari and S. Cho, *Journal*, 2021, **11**.
38. Y. Yang, Y. Wang, H. Yan, C. Cao and N. Chen, *Journal*, 2023, **16**.
39. T. Guo, N. Yang, B. Yang, A. Schulte, Q. Jin, U. Koch, S. Mandal, C. Engelhard, O. A. Williams, H. Schonherr and X. Jiang, *Carbon*, 2021, **178**, 19-25.
40. R. J. Eyre, J. P. Goss, P. R. Briddon and M. G. Wardle, *physical. stat. sol. (a)*, 2007, **204**, 2971-2977.
41. B. S. Truscott, M. W. Kelly, K. J. Potter, M. N. Ashfold and Y. A. Mankelevich, *J. Phys. Chem. A*, 2016, **120**, 8537-8549.
42. Z. W. Wang, B. W. Li, Y. Liu, H. Y. Zhao, Q. Y. Guo, L. C. Chen, H. A. Ma and X. P. Jia, *Journal of Crystal Growth*, 2023, **624**.
43. S. Kunuku, M. Ficek, A. Wieloszynska, M. Tamulewicz-Szwajkowska, K. Gajewski, M. Sawczak, A. Lewkowicz, J. Ryl, T. Gotszalk and R. Bogdanowicz, *Nanotechnology*, 2022, **33**, 125603.
44. J. Achard, F. Silva, R. Issaoui, O. Brinza, A. Tallaire, H. Schneider, K. Isoird, H. Ding, S. Koné, M. A. Pinault, F. Jomard and A. Gicquel, *Diamond and Related Materials*, 2011, **20**, 145-152.
45. A. F. Sartori and M. Schreck, *physica status solidi (a)*, 2014, **211**, 2290-2295.
46. E. Gheeraert, P. Gonon, A. Deneuve, L. Abello and G. Lucazeau, *Diamond and Related Materials*, 1993, **2**.
47. H. Katayama-Yoshida, T. Nishimatsu, T. Yamamoto and N. Orita, *physical. stat. sol. (b)*, 1998, **210**, 429.
48. H. Katayama-Yoshida, T. Nishimatsu, T. Yamamoto and N. Orita, *J. Phys.: Condens Matter*, 2001, **13**, 8901-8914.
49. Q. Liang, C.-s. Yan, Y. Meng, J. Lai, S. Krasnicki, H.-k. Mao and R. J. Hemley, *Journal of Physics: Condensed Matter*, 2009, **21**, 364215.

50. K. G. Crawford, I. Maini, D. A. Macdonald and D. A. J. Moran, *Progress in Surface Science*, 2021, **96**, 100613.
51. J.-H. Seo, H. Wu, S. Mikael, H. Mi, J. Blanchard, G. Venkataramanan, W. Zhou, S. Gong, D. Morgan and Z. Ma, *Journal of Applied Physics*, 2016, **119**.
52. J. Li, Q. Wang, Y. Liu, Z. Jiang, J. Liu, H. Li and X. Yuan, *Functional Diamond*, 2021, **1**, 135-142.
53. W. Nie, Y. Sun, M. Li, C. Li and H. Li, *Diamond & related materials*, 2022, **125**, 109030.
54. P. Hartmann, R. Haubner and B. Lux, *Diamond and Related Materials*, 1997, **6**, 456-462.
55. A. Croot, M. Z. Othman, S. Conejeros, N. A. Fox and N. L. Allan, *J. Phys. Condens. Matter*, 2018, **30**, 425501.
56. D. Zhou, L. Tang, J. Zhang, R. Yue and Y. Wang, *Cham*, 2022.
57. D. Y. Liu, L. C. Hao, Y. Teng, F. Qin, Y. Shen, K. Tang, J. D. Ye, S. M. Zhu, R. Zhang, Y. D. Zheng and S. L. Gu, *APL Mater*, 2021, **9**, 081106.
58. Y. Liu, Y. Zhang, K. Cheng, X. Quan, X. Fan, Y. Su, S. Chen, H. Zhao, Y. Zhang, H. Yu and M. R. Hoffman, *Angew. Chem. Int. Ed*, 2017, **56**, 15607-15611.
59. L. Tang, X. Zhou, R. Yue and Y. Wang, *N-type Lithium-Nitrogen Codoping in Diamond from First Principles*, Institute of Microelectronics, Tsinghua University, Beijing, China.
60. M. W. N. Ngambou, C. Pellet-Mary, O. Brinza, A. Antonino, G. Hetet, A. Tallaire, F. B én édic and J. Achard, *J. Diamond*, 2022, **123**, 108884.
61. K. Kobashi, in *Diamond Films*, ed. K. Kobashi, Elsevier Science Ltd, Oxford, 2005, pp. 31-50.
62. G. E. Lloyd, *Mineralogical Magazine*, 1987, **51**, 3-19.
63. D. K. Pandey, H. L. Kagdada, P. Sanchora and D. K. Singh, in *Modern Techniques of Spectroscopy: Basics, Instrumentation, and Applications*, eds. D. K. Singh, M. Pradhan and A. Materny, Springer Singapore, Singapore, 2021, pp. 145-184.
64. Z. Wang, B. Li, Y. Liu, H. Zhao, Q. Guo, L. Chen, H. Ma and X. Jia, *Journal of Crystal Growth*, 2023, **624**, 127431.
65. J. I. B. Wilson, J. S. Walton and G. Beamson, *Journal of Electron Spectroscopy and Related Phenomena*, 2001, **121**, 183-201.
66. R.-D. Holmes, MScR, University of Bristol, 2023.
67. J. F. Watts and J. Wolstenholme, *An Introduction to Surface Analysis by XPS and AES*, John Wiley & Sons Ltd, 2nd edn., 2020.
68. J. E. Whitten, *Applied Surface Science Advances*, 2023, **13**, 100384.
69. D. S. Schmool and H. Kachkachi, in *Solid State Physics*, eds. R. E. Camley and R. L. Stamps, Academic Press, 2015, vol. 66, pp. 301-423.
70. X. M. Cheng and D. J. Keavney, *Reports on Progress in Physics*, 2012, **75**, 026501.
71. O. Lindberg, *Proceedings of the IRE*, 1952, **40**, 1414-1419.
72. F. Werner, *Journal of Applied Physics*, 2017, **122**.
73. W. L. B. Huey and J. E. Goldberger, in *Xenes*, eds. A. Molle and C. Grazianetti, Woodhead Publishing, 2022, pp. 255-294.
74. D. Y. Liu, K. Tang, S. M. Zhu, R. Zhang, Y. D. Zheng and S. L. Gu, *Chinese Physics B*, 2023, **32**, 7.
75. E. Requena, MSci, University of Bristol, 2023.
76. A. Shchukarev and D. Korolkov, *Central European Journal of Chemistry - CENT EUR J CHEM*, 2004, **2**, 347-362.

77. J. Laverock, personal communication.
78. T. L. Martin, Doctor of Philosophy, 2011.
79. F. G. Celii, H. H. Nelson and P. E. Pehrsson, *Journal of Materials Research*, 1990, **5**, 2337-2344.

7 Appendix

7.1 2-point probe

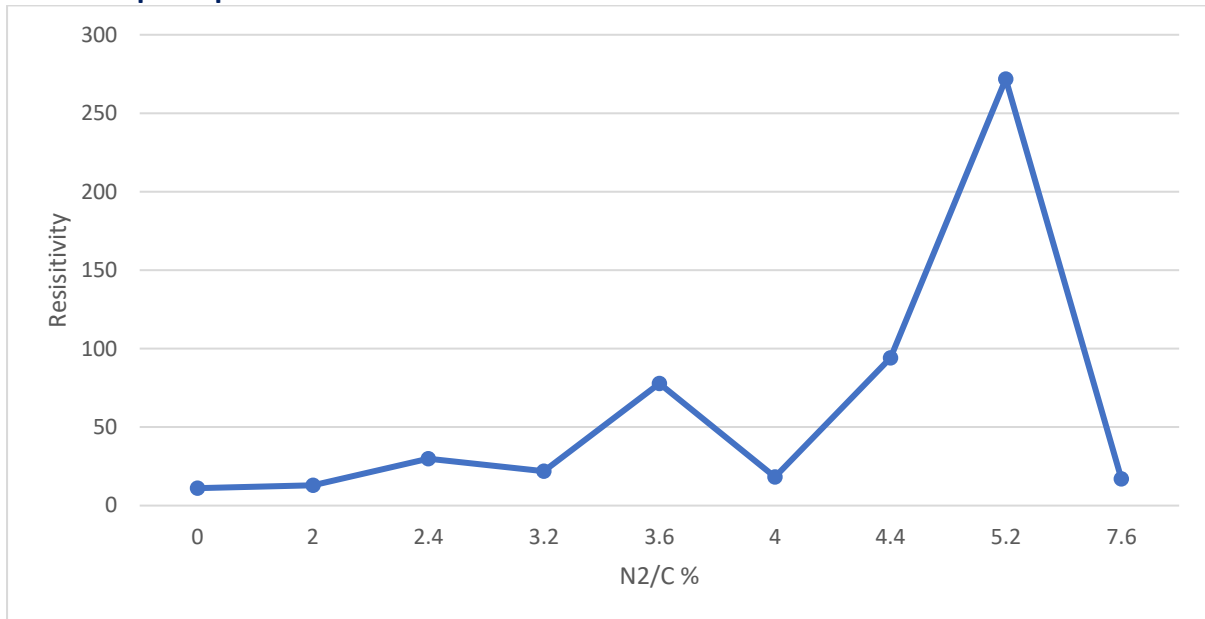


Figure A.1 – Resistivity measurements recorded with two-point probe apparatus, these results are quite variable and disagree with those recorded with the more reliable four-point probe.

7.2 4-point probe

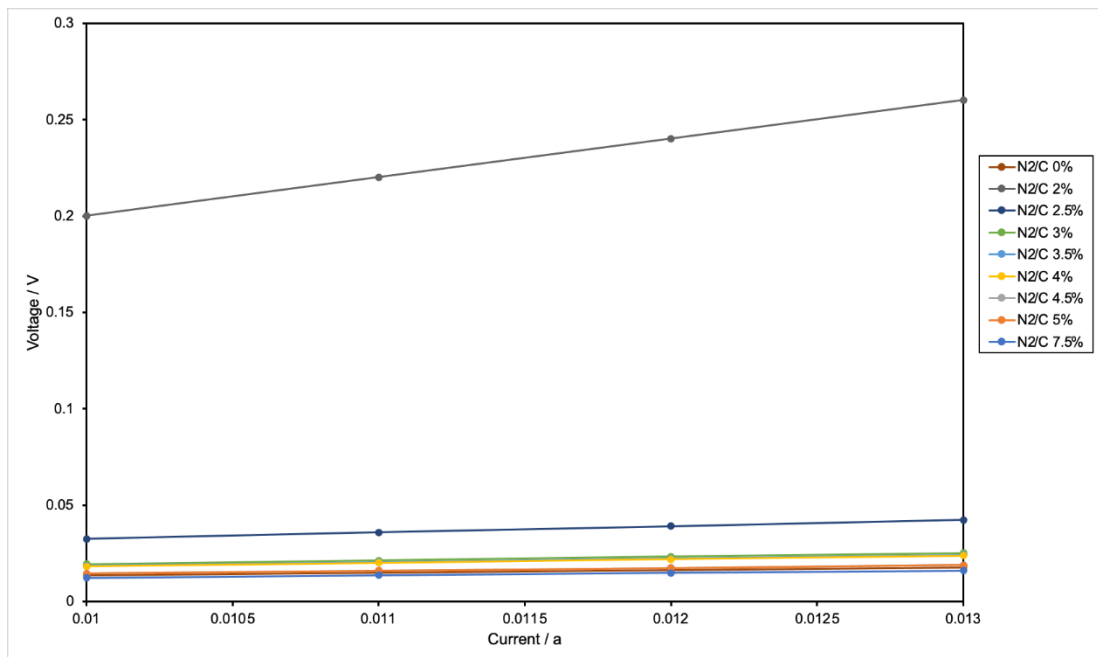


Figure A.2 – Plot of linear 4-point probe measurements inclusive of 2% sample

7.3 Hall measurements

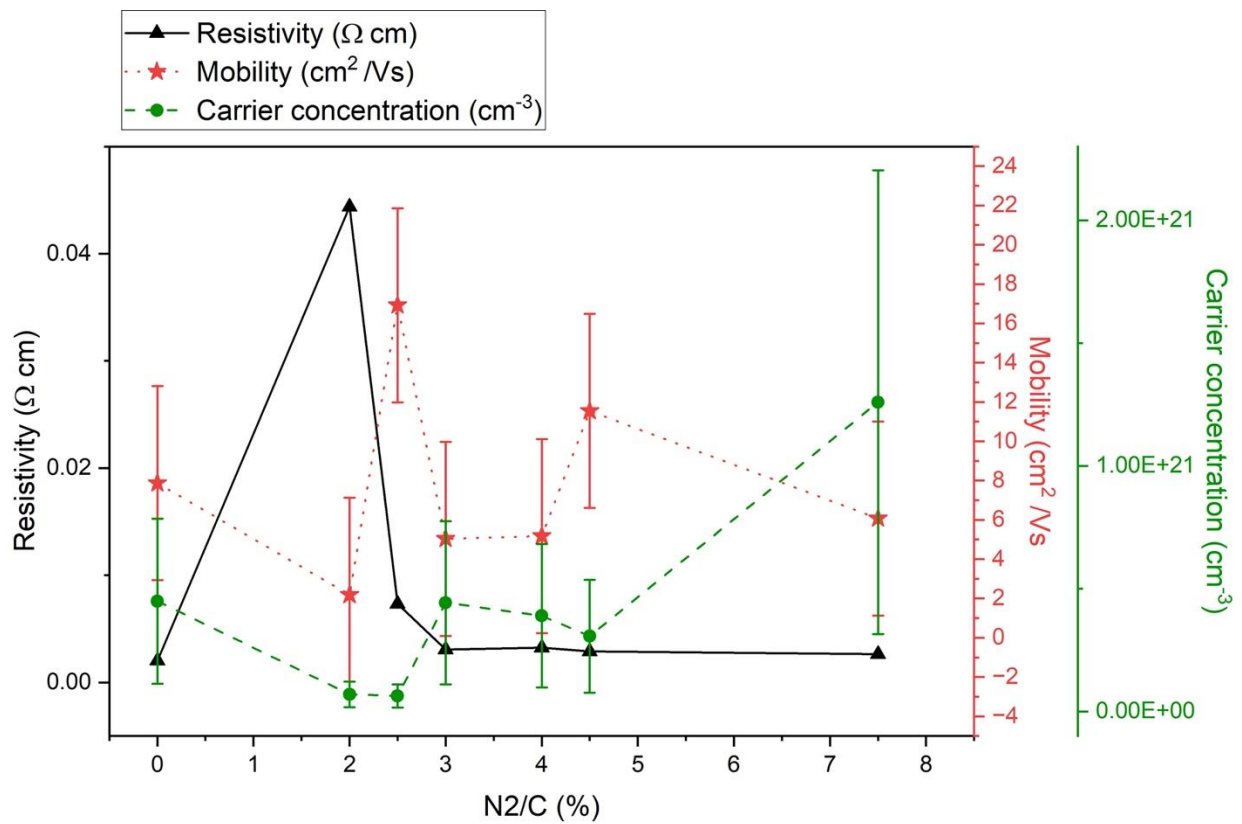


Figure A.3 – Estimated error bars for carrier concentration and mobility values of nitrogen variation BNDD growths. The scales of the corresponding axes have been expanded to allow for the size of the error bars.

Noticeably the 2% sample has much lower error, due to its definitive p-type characterisation.

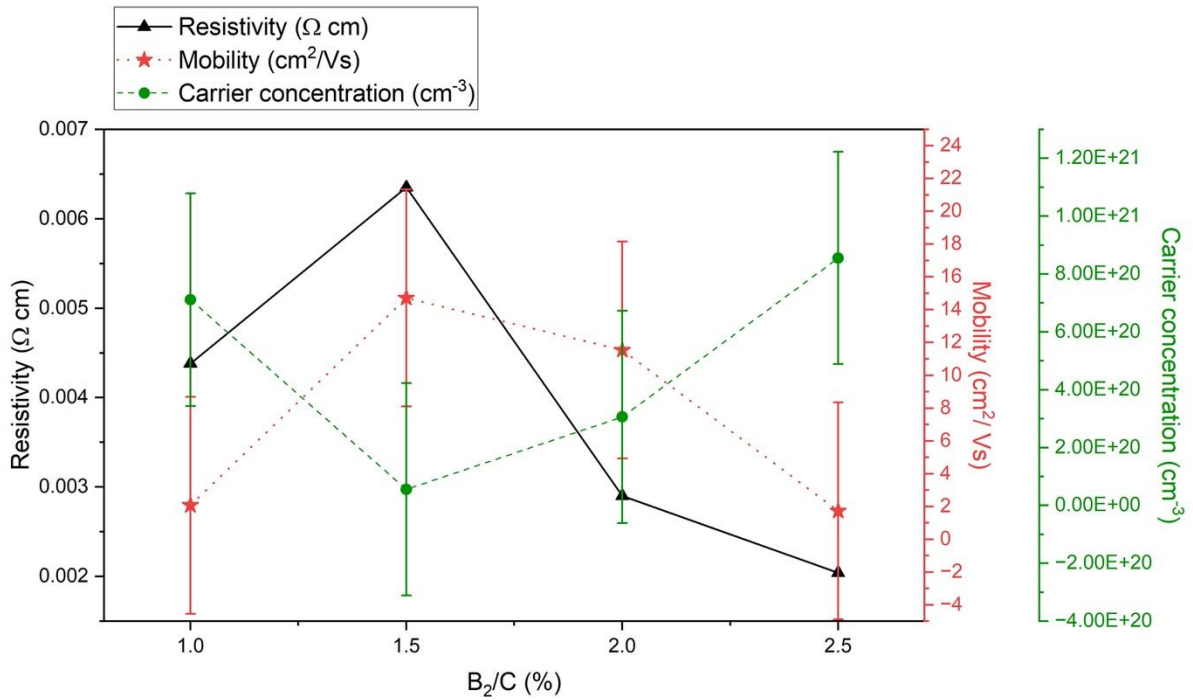


Figure A.4 – Estimated error bars for carrier concentration and mobility values of boron variation BNDD growths. The scales of the corresponding axes have been expanded to allow for the size of the error bars.

Table A.1 – Bulk carrier concentrations of boron variation growths measured within the ranges of 500 μ A and 100 μ A. These results demonstrate the variability in the readings, and the predominantly negative readings in both the 1.5% and 2% B₂/C samples.

Current	1% B ₂ /C	1.5% B ₂ /C	2% B ₂ /C & 4.5% N ₂ /C	2.5% B ₂ /C
500 μA	8.72E+20	-6.32E+20	1.87E+20	1.98E+23
	7.09E+20	-2.04E+21	-8.83E+20	1.40E+21
	5.53E+20	-7.01E+21	-4.15E+20	2.81E+20
	1.15E+21			2.41E+21
	-6.14E+20			-6.11E+20
	-1.08E+20			
	-2.77E+20			
	-1.69E+21			
100 μA		5.39E+19	-1.62E+21	1.34E+20
		-6.07E+19	4.26E+20	-3.77E+20
		2.09E+20	-1.92E+20	1.88E+20
		-2.87E+20		1.40E+20
		-5.26E+19		1.60E+20

Table A.2 – Bulk carrier concentrations of nitrogen variation growths measured within the ranges of 500 μ A and 100 μ A

Current	0%N ₂ /C	2% N ₂ /C	2.5% N ₂ /C	3% N ₂ /C	4% N ₂ /C	7.5% N ₂ /C
500 μA	-3.16E+20	6.67E+19	9.12E+19	-1.80E+21	-6.81E+20	3.94E+21
	-7.08E+20	8.80E+19	6.71E+19	6.00E+20	2.88E+20	3.31E+20
	3.67E+20	6.54E+19	2.96E+19	4.38E+20	-3.20E+21	4.76E+20
	2.90E+20	6.46E+19	-4.05E+21	-2.54E+20	4.84E+20	-1.69E+20
	6.90E+20	6.16E+19	4.35E+20	2.90E+20	3.97E+20	-3.01E+21
100 μA		3.72E+19	9.12E+19	4.23E+19		2.87E+20
		4.13E+19	6.71E+19	-9.01E+19		-1.06E+20
		8.11E+19	2.96E+19	-3.08E+19		-1.50E+20
		2.90E+19	-3.48E+20	-1.57E+20		-2.36E+20
		2.35E+19		7.74E+19		7.65E+19